

# **Rapid Inspection of Pavement Markings Using Mobile Laser Scanning Point Clouds**

by

**Haocheng Zhang**

**A thesis  
presented to the University of Waterloo  
in fulfillment of the  
thesis requirement for the degree of  
Master of Science  
in  
Geography**

**Waterloo, Ontario, Canada, 2016**

**© Haocheng Zhang 2016**

## **Author's Declaration**

I hereby declare that I am the sole author of this thesis. This is a true copy of the thesis, including any required final revisions, as accepted by my examiners.

I understand that my thesis may be made electronically available to the public.

## Abstract

Intelligent Transportation System (ITS) is the combination of information technology, sensors and communications for more efficient, safer, more secure and more eco-friendly surface transport. One of the most viable forms of ITS is the driverless car, which exist mainly as prototypes. Serval automobile manufacturers (e.g. Ford, GM, BMW, Toyota, Tesla, Honda) and non-automobile companies (e.g. Apple, Google, Nokia, Baidu, Huawei) have invested in this field, and wider commercialization of the driverless car is estimated in 2025 to 2030. Currently, the key elements of the driverless car are the sensors and a prior 3D map. The sensors mounted on the vehicle are the “eyes” of the driverless car to capture the 3D data of its environment. Comparing its environment and a pre-prepared prior known 3D map, the driverless car can distinguish moving targets (e.g. vehicles, pedestrians) and permanent surface features (e.g. buildings, trees, roads, traffic signs) and take relevant actions. With a centimetre-accuracy prior map, the intractable perception problem is transformed into a solvable localization task. The most important technology for generating the prior map is Mobile Laser Scanning (MLS). MLS technology can safely and rapidly acquire highly dense and accurate georeferenced 3D point clouds with the measurement of surface reflectivity. Therefore, the 3D point clouds with intensity data not only offer the detailed 3D surface of the road but also contains pavement marking information that are embedded in the prior map for automatic navigation. Relevant researches have been focused on the pavement marking extraction from MLS data to collect, update and maintain the 3D prior maps. However, the accuracy and efficiency of automatic extraction of pavement markings can be further improved by intensity correction and window-based enhancement. Thus, this study aims at building a

robust method for semi-automated information extraction of pavement markings detected from MLS point clouds.

The proposed workflow consists of three components: preprocessing, extraction, and classification. In preprocessing, the 3D MLS point clouds are converted into the radiometrically corrected and enhanced 2D intensity imagery of the road surface. Then the pavement markings are automatically extracted with the intensity using a set of algorithms, including Otsu's thresholding, neighbour-counting filtering, and region growing. Finally, the extracted pavement markings are classified with the geometric parameters using a manually defined decision tree. Case studies are conducted using the MLS datasets acquired in Kingston (Ontario, Canada) and Xiamen (Fujian, China), respectively, with significantly different road environments by two RIEGL VMX-450 systems. The results demonstrated that the proposed workflow and method can achieve 93% in completeness, 95% in correctness, and 94% in F-score respectively when using Xiamen dataset, while 84%, 93%, 89% respectively when using Kingston dataset.

## **Acknowledgements**

During my study at the University of Waterloo, and living in Canada, I have been helped by a lot of people.

I would like to express my great gratitude to my supervisor, Professor Dr. Jonathan Li, for accepting me to join the Mobile Mapping group, providing me with the encouragement, insight, and support during my Master's study. Thanks go to my Thesis Examining Committee, Dr. Peter Deadman, Prof. Dr. Richard Kelly, both from the Department of Geography and Environmental Management, and Dr. Alexander Wong from the Department of Systems Design Engineering to review my thesis and provide me their critical comments and valuable suggestions to make my thesis with a better quality.

I would like to thank the Mobile Mapping Lab group members, Haiyan Guan, Qing Xiang, Yongtao Yu, Lanying Wang, Weikai Tan, Xinqu Chen, Menglan Zhou, Yifei Chen, Zilong Zhong, for their contribution to my research. Thank Zeng Ji and Xiaoliang Zou, visiting scholars here, for their suggestions. Both the Fujian Key Laboratory of Sensing and Computing for Smart Cities, Xiamen University and Tulloch Engineering are acknowledged for providing their RIEGL VMX-450 point cloud data to support this study.

Thanks to all my friends: Lei Wang, for sharing knowledge on image processing; Anqi Fu, for giving suggestions on thesis writing; Weigang Tang, for modeling; Zhenghao Li, Siyuan Chen and Chenpei Shi, for helping me a lot in life; and all other friends in China and here.

Thanks to my dear parents and my uncle's family, with whom I gain the coverage to keep going on these years. Special thanks to my girlfriend, Jie Li, who has been in the United Kingdom but accompanied me and helped me these years.

*Haocheng Zhang*

March 13, 2016

# Table of Contents

<b>Author's Declaration</b> .....	ii
<b>Abstract</b> .....	iii
<b>Acknowledgements</b> .....	v
<b>Table of Contents</b> .....	vii
<b>List of Figures</b> .....	x
<b>List of Tables</b> .....	xiii
<b>List of Abbreviation</b> .....	xiv
<b>Chapter 1 Introduction</b> .....	1
<b>1.1 Motivation</b> .....	1
<b>1.2 Objective</b> .....	3
<b>1.3 Thesis Structure</b> .....	4
<b>Chapter 2 Background and Related Work</b> .....	6
<b>2.1 Principle of Mobile Laser Scanning</b> .....	6
<b>2.1.1 Components of a Mobile Laser Scanning System</b> .....	6
<b>2.1.2 A Mobile Laser Scanning System</b> .....	8
<b>2.1.3 Geo-referencing of MLS Data</b> .....	9
<b>2.2 Road Surface Detection Using Mobile Laser Scanning Data</b> .....	11
<b>2.3 Road Marking Extraction Methods</b> .....	16
<b>2.3.1 Images and Video-based Road Marking Extraction</b> .....	16
<b>2.3.2 MLS Based Road Marking Extraction</b> .....	18
<b>2.3.3 Scanning Range and Incidence Angle Effects on MLS intensity</b> .....	21
<b>2.4 Road Marking Classification</b> .....	25
<b>2.4.1 Road Marking Isolation</b> .....	25
<b>2.4.2 Feature Extraction</b> .....	26
<b>2.4.3 Classification Methods</b> .....	31
<b>2.5 Chapter Summary</b> .....	33
<b>Chapter 3 Proposed Method</b> .....	34
<b>3.1 Study Area and Dataset</b> .....	34

3.2	Description of the Proposed Workflow .....	37
3.3	Preprocessing of MLS Data.....	39
3.3.1	Road Surface Extraction .....	39
3.3.1.1	Non-ground Points Removal .....	39
3.3.1.2	IDW Interpolation of DTM .....	40
3.3.1.3	High-pass Filtering.....	41
3.3.1.4	Region Growing Segmentation .....	42
3.3.2	Intensity Image Generation.....	42
3.3.3	Scan Angle Based Intensity Correction .....	43
3.3.4	Large-size High-pass Enhancement .....	45
3.4	Extraction of Road Marking.....	47
3.4.1	Otsu’s Thresholding .....	47
3.4.2	Image Denoising .....	48
3.4.3	Accuracy Assessment .....	50
3.5	Classification of Road Marking .....	52
3.5.1	Road Marking Segmentation .....	52
3.5.2	Feature Extraction of Road Marking.....	54
3.5.3	Decision-tree Based Hierarchical Classification.....	57
3.6	Chapter Summary.....	59
Chapter 4	Results and Discussion .....	61
4.1	Preprocessing of MLS Data.....	61
4.1.1	Road Surface Extraction .....	61
4.1.1.1	Non-ground Removal.....	61
4.1.1.2	Road Surface Region Extraction .....	62
4.1.2	Intensity Image Generation.....	63
4.1.3	Intensity Image Correction .....	65
4.2	High-pass Filter Enhancement and Accuracy Assessment.....	67
4.2.1	High-pass Filter Enhancement.....	67
4.2.2	Accuracy Assessment of Road Marking Extraction and Comparative Study.....	74



4.2.3	Comparative Study .....	75
4.3	Road Marking Segmentation .....	78
4.4	Road Marking Classification .....	79
4.5	A Case Study on Road Marking Classification in Kingston .....	82
4.5.1	Challenges and Adjustments .....	83
4.5.2	Results and Discussion .....	86
4.6	Chapter Summary.....	90
Chapter 5 Conclusions and Recommendations.....		93
5.1	Conclusions.....	93
5.2	Contributions.....	94
5.3	Recommendations for Future Studies .....	96
5.3.1	Point Cloud Intensity Correction.....	96
5.3.2	Large-size High-pass Enhancement .....	97
References .....		98

## List of Figures

Figure 2.1: A Mobile Laser Scanning system. ....	9
Figure 2.2: Principle of Geo-referencing. ....	10
Figure 2.3: Geometry and parameters involved in the radar equation (Source: Wagner et al., 2006). ....	22
Figure 2.4: An overview of shape description techniques. (Source: Yang et al., 2008) ...	27
Figure 3.1: Study areas: (a) Island Ring Road in Xiamen, Fujian, China, and (b) King Street in Kingston, Ontario, Canada. ....	35
Figure 3.2: Workflow of road marking extraction and classification: (a) Workflow of Preprocessing, (b) Workflow of Road Marking Extraction, (c) Workflow of Road Marking Classification. ....	38
Figure 3.3: Octree structure and upward 9-neighbours voxel: (a) Octree partition structure, and (b) upward growing scheme (Source: Yu et al., 2015). ....	40
Figure 3.4: Illustrations of the high-pass filters. ....	41
Figure 3.5: Intensity of the Sample05 and its associated plot: (a) the plot of the cosine of the scan angle rank vs. intensity and (b) Scatterplot of pure road marking pixels. Green points are the inlier and the cyan points are the outlier. The red line is the trend of the linear regression. ....	44
Figure 3.6: Neighbour-counting filtering: (a) corrected intensity image of road surface, (b) extracted result from enhanced intensity image, (c) 15×15 kernel of neighbours counting, and (d) neighbour-based filtering result. ....	49
Figure 3.7: Region growing segmentation: (a) extracted road marking, (b) region growing segmentation result. ....	52
Figure 3.8: Segmentation of large road marking segments: (a) neighbour-counting image of large segments, (b) neighbour-counting image of wide road marking, (c) junction detection based on neighbour-counting, and (e) segmentation result of large road marking. ....	54
Figure 3.9: Road marking shape feature: area and width: (a) area of labeled road markings, and (b) estimated width of labeled road markings. ....	55

Figure 3.10: Road marking boundaries and minimum bounding rectangles: (a) and (b) show the boundaries of the road marking segments, (c) and (d) show the bounding rectangles of the road marking segments. ....	56
Figure 3.11: A hierarchical tree of the road marking categories. ....	58
Figure 3.12: Decision tree classification: (a) the first level result, (b) the second level result, (c) the third level result, (d) the fourth level result. ....	59
Figure 4.1: MLS data of Sample07: (a) MLS data, (b) ground surface points. ....	62
Figure 4.2: Sub-sample of the ground surface: (a) DTM (5 cm grid size), (b) 3×3 High-pass Filtering, (c) Absolute Value of High-pass Filtering, (d) Thresholding Result, and (e) Region Growing Result. ....	63
Figure 4.3: Intensity image generated at different resolutions. ....	64
Figure 4.4: IDW interpolation results of point intensity: with the grid size of 5cm from Sample01 to Sample06. ....	65
Figure 4.5: Corrected Intensity Image from Sample01 to Sample06. ....	66
Figure 4.6: Histograms of the road markings and pavements: (a) the histogram of pavements and road markings in intensity image and (b) the histogram of pavements and road markings in corrected intensity image. ....	67
Figure 4.7: F-Score for each high-pass filter size based on Sample02. ....	68
Figure 4.8: High-pass results with 3×3, 5×5, 11×11, 31×31, 51×51 kernel. ....	69
Figure 4.9: High-pass enhanced images with 31×31 kernel. ....	70
Figure 4.10: Otsu's thresholding results based on high-pass enhanced images from sample01 to Sample06. ....	71
Figure 4.11: Intensity image, ground truth image (white: road marking pixels, black: pavement pixels), error image (white: False Negative, red: False Positives, blue: True Positives). ....	72
Figure 4.12: Performance of different high-pass filter with Sample06. ....	73
Figure 4.13: Results of road marking extraction. ....	74
Figure 4.14: Extracted road markings from Sample 01 dataset: (a) road surface points, (b) Chen's method result, (c) Guan's method result, (d) Yu's method result, (e)	

proposed method result, and manually labeled reference data (Adapted from: Yu, 2015).....	77
Figure 4.15: Extracted road markings from Sample 05 dataset: (a) road surface points, (b) Chen’s method result, (c) Guan’s method result, (d) Yu’s method result, (e) proposed method result, and manually labeled reference data (Adapted from: Yu, 2015).....	77
Figure 4.16: Results of road marking clustering and segmentation.....	78
Figure 4.17: Results of road marking classification. ....	79
Figure 4.18: Errors of road marking classification. ....	80
Figure 4.19: Detection of Chinese characters: (a) road marking region, (b) dilated road marking region, (c) Chinese characters classified in dilated region. ....	81
Figure 4.20: Road marking extraction of sample07 in Xiamen (a) road surface intensity image, (b) road marking extraction result.....	82
Figure 4.21: Road surface detection in Kingston’s sample: (a) candidate road markings (green) (b) road surface coverage thresholding result, including road surface (blue), road markings (green), and non-marking segments (red). ....	84
Figure 4.21: Density filtering of road marking: (a) road marking with noise, and (b) density filtering result of (a). ....	85
Figure 4.23: A remedial measure of road marking: (a) the unclassified marking segments, and (b) result of the rectification method. ....	86
Figure 4.24: IDW interpolation vs Maximum value enhancement: (a) IDW mean intensity image, (b) the maximum corrected-intensity image, (c) road marking extraction result from IDW mean corrected-intensity image, and (d) road marking extraction result from maximum corrected-intensity image. ....	87
Figure 4.25: Road marking classification in Kingston: (a) overview of road marking classes, black area represent detected road surface, blue lines represent curbs, (b) road intersection 1, (c) road intersection 2.....	89

## List of Tables

Table 2.1: Parameters of the geo-referencing equation. ....	10
Table 2.2: Summary of different road surface detection techniques.....	15
Table 2.3: Summary of impacts of road marking extraction.....	17
Table 2.4: Summary of road marking detection techniques from MLS data. ....	20
Table 2.5: Summary of different geometric features of road marking shape. ....	30
Table 3.1: Point Data Record (Source: ASPRS Standards Committee, 2011).....	37
Table 3.2: Summary of road marking extraction. ....	50
Table 3.3: A confusion matrix for binary classification. ....	50
Table 3.4: Road marking geometric measures .....	55
Table 4.1: Resolution of intensity image and image size (Sample02). ....	63
Table 4.2: Quantitative assessment using completeness, correctness and F-Score. ....	74
Table 4.3: Quantitative evaluation results of different road marking extraction methods.	77
Table 4.4: Comparison of the road marking results from different rasterization methods. .....	87
Table 4.5: Quantitative assessment results using the Kingston dataset .....	90

## List of Abbreviation

2D	Two-dimensional
3D	Three-dimensional
ADAS	Advanced Driver Assistance Systems
ALS	Airborne laser scanning
CRF	Conditional Random Field
DMI	Distance Measurement Indicator
DOPP	Density of Projected Points
DTM	Digital Terrain Model
GNSS	Global navigation satellite system
GPS	Global positioning system
IDW	Inverse Distance Weighting
IMU	Inertial measurement unit
IT	Information Technology
ITS	Intelligent Transportation Systems
KNN	K-Nearest Neighbour
LiDAR	Light detection and ranging
MBR	Minimum Bounding Rectangle
MLS	Mobile Laser Scanning
MMS	Mobile mapping system
RANSAC	Random sample consensus
RJMCMC	Reversible Jump Markov Chain Monte Carlo
TLS	Terrestrial laser scanning

TOF

Time of Flight

# Chapter 1 Introduction

## 1.1 Motivation

Intelligent transportation systems (ITS) have been introduced for many years. It is the result of developing transportation systems by information technology (IT), sensors and communications technologies (GSMA, 2014). A country's transportation system has significantly improved by building new roads, maintaining aging infrastructures as well as integrating infrastructures (roads, traffic lights, messages signs, etc.) into vehicle systems via wireless technologies. ITS can improve the performance of the transportation system significantly, enhancing road safety, improving traffic efficiency and environmental sustainability, and reducing incidents and congestion.

The current development of ITS focuses on driverless car, which is the most viable form of ITS. The driverless cars are still in the research stage, but it is estimated to be launched in the next decade. Several companies predicted the commercial sale of the fully autonomous vehicles would be between 2018 and 2020 (Litman, 2014). Companies in automotive and other industries are racing to develop the technologies, including Tesla, Ford, General Motors, Honda, Google, Apple, Baidu; etc. As a robotic vehicle that is capable of traveling between destinations without a human operator, the driverless car is driven not by human but the data. There are two principal data sources for the navigation of the driverless cars. The first one is the sensory input in terms of the surroundings of the driverless car. It can be acquired and collected by the radar, LiDAR sensor and video cameras. The roof-mounted Light Detection and Ranging (LiDAR) sensor monitors a range from 60 to 100m from the car and creates a 3D map of the environment (Google driverless car report, 2015; Whitwam, 2014). The second one is a prior highly detailed



3D map. Different from the traditional road map, this detailed 3D map is developed for the machine. The highly precise map is indispensable not only to allow a car to locate itself on the traffic lane but also enable a vehicle to take corresponding actions correctly (Guizzo, 2011). In a scenario where a driverless car tries to overtake a slower truck in front of it on a motorway. The car itself must have the knowledge that there is another lane to move into. It has to follow the legal restrictions to overtake or drive in the other lane. The width of the lane and the stretch length of road for completing the maneuver also need to be taken in to consideration. Thus, the automated car has to be supported by detailed lane model. Such a lane model needs to have precise lane geometry with lane boundaries and rich attributions such as lane types, lane traversal information, lane marking types and lane speed limit information (Kent, 2015). Except the detailed information of lanes, every stationary object should be recorded in the precise 3D map. Therefore, the car is able to recognize the moving objects that are not in the 3D map, such as vehicles and pedestrians. With the prior 3D map, the autonomous driving is transformed from a difficult perception task into a localization problem.

To capture the world in 3D for autonomous vehicles, Mobile Laser Scanning (MLS) technology is applied before the driverless cars hit the road. It is an effective and efficient method for acquiring highly accurate, precise, and dense geo-referencing 3D topographic data (Puente et al., 2013). MLS systems are the mobile mapping systems based on the LiDAR, which capture 3D point clouds from the surrounding environment using profiling scanners. The laser scanners are mounted on the roof or the rear of the vehicle to acquire the range data during the movement of the vehicle. The vehicle has motion-tracking navigation devices, and the vehicle's trajectory and attitude are tracked by a global

navigation satellite system (GNSS) and inertial measurement unit (IMU). The information acquired can be used to geo-reference a 3D point cloud from the range data. MLS offers many advantages, including high accuracy, high point density and rapid data acquisition. For example, the integration of two RIEGL VQ-450 laser scanners in a RIEGL VMX-450 system can provide 8 mm measurement accuracy and 5 mm precision (RIEGL, 2015). Their maximum effective measurement rate can reach 1.1 million points per second. As a result, the system can collect data up to 250 Mb in 100 m path with 20 m width at the speed of 30-50 km/h. Therefore, MLS is a feasible 3D mapping technology for surveying and mapping of the urban environment (Williams et al., 2013). The detailed 3D point cloud data normally involves the important information of traffic lane such as lanes' geometry and boundary, lanes' types, speed limit and lane traversal information. The indispensable data helps the driverless car make solid decisions (Kent, 2015). However, processing the point cloud data to generate the highly detailed 3D map is a labour-intensive process. There are three challenges in processing the 3D point clouds collected by MLS. Firstly, the volume of MLS data is incredibly large. Secondly, the MLS data is unstructured. Thirdly, the MLS data has unevenly distributed intensity. In this context, using the state-of-the-art and efficient MLS data to extract detailed information of lanes become an urgent need for the development of driverless cars. It is noted that majority of the information of lanes is represented by the road markings, thus, this study focuses on the extraction and recognition of road markings from MLS data for building the prior map of driverless car.

## **1.2 Objective**

The main purpose of this study is to develop a semi-automatic workflow for road

marking detection and classification using 3D point clouds that are acquired by a vehicle-mounted MLS system. The positioned and recognized road markings can be transformed to the detailed lane information (such as lanes' geometry, boundary and types) to support the operation of the driverless car. In this study, the MLS data of Island Ring Road (City of Xiamen, Fujian) and King Street (City of Kingston, Ontario) were acquired and collected from the two RIEGL VMX-450 systems, provided by the Fujian Key Laboratory of Sensing and Computing for Smart Cities, Xiamen University, China and the Tulloch Engineering, Ottawa, Ontario, respectively. The detailed research objectives are listed below:

(1) Completely extract the road markings from MLS data automatically with high accuracy in different environments;

(2) Classify the road markings into thorough and detailed categories based on the extracted information from MLS data with a high accuracy.

### **1.3 Thesis Structure**

The thesis consists of the five chapters.

Chapter 1 introduces the research background and motivations followed by addressing the research objectives.

Chapter 2 reviews fundamental knowledge of the MLS technology, and the related studies about the road surface information extraction and recognition by using MLS data and digital images/videos.

Chapter 3 describes the study areas and test datasets, the designed workflow and the algorithms details for road information extraction and classification is also explained.

Chapter 4 first presents the extracted and classified road marking information from the MLS data of Island Ring Road in Xiamen using the proposed workflow and algorithms. The results were compared with the performance of the three recently published methods. Second, the MLS data of the King Street, Kingston is used to apply the proposed workflow and algorithm with modification to handle the cracking, rutting and potholes issues.

Chapter 5 concludes contributions of the thesis and points out the future research directions.

## Chapter 2 Background and Related Work

### 2.1 Principle of Mobile Laser Scanning

#### 2.1.1 Components of a Mobile Laser Scanning System

Mobile laser scanning (MLS) may be defined as the science and technology for deploying portable laser scanner(s) on road, rail or marine vehicles to rapidly collect 3D georeferenced point clouds for digital representation of the built and physical environments. Compared with the early mobile mapping systems mainly using digital and video cameras (Schwarz and El-Sheimy, 2007; Lemmens, 2011), a MLS system nowadays is normally integrated with optimal digital camera(s), laser scanner(s), a Global Navigation Satellite System (GNSS) receiver, an Inertial Measurement Unit (IMU), and a Distance Measurement Indicator (DMI) (Olsen, 2013; Florida Department of Transportation, 2013).

**The laser scanner** emits laser pulses or continuous waves to the surface of a target and receives the backscattered pulses or waves. There are two range measurements for laser scanning technologies: time-of-flight (TOF) and phase shift (Vosselman and Maas, 2010).

The TOF scanners (also called pulse-based) scanners emit a laser pulse to the target, and receives the backscattered pulse. The pulse traveling time recorded in the system is used to measure the distance between the scanner and the target. In the phase-based system, the phase shift and the number of transmitted are used to calculate the distance. Both of these approaches utilise the amount of the reflected energy to measure the intensity of a point on the surface. Even though the phase-based scanner has a less measurement range than the pulse-based scanner's, it has a higher scanning frequency

and accuracy. In addition, the pulse-based scanners are more suitable for 3D reconstruction of large areas, such as in urban environment; while the phase-based scanners are more appropriate in the case of more detailed and precise measurement, such as digital archaeology (Ogund, 2015). Thus, the majority of MLS systems are mounted with pulse-based scanners. For example, the maximum range of TOF scanner RIEGL VQ-450 is 800 m.

**The optical digital cameras** capture the color of the target surface to supplement the original 3D point clouds that are acquired by laser scanners. The raw MLS point clouds lack of the texture information, while the true colour images cannot provide with accurate geometry information. Fusion of the true colour images and raw point clouds produce 3D true coloured point clouds, which can facilitate the elaborated visualization and 3D construction.

**The GPS receiver** observes time, position and the estimated velocity. It provides highly accurate position under optimal satellite configuration (Olsen, 2013; Florida Department of Transportation, 2013). However, the positioning accuracy would decline when the GPS receiver is under poor satellite configuration. For example, the GPS is located in a place surrounded by a cluster of tall buildings.

**The IMU** consists of three accelerometers and three gyroscopes. The acceleration is measured in three axes (X, Y, Z), and the angular rate is measured along each of the acceleration axes. In the signal processing step, the total acceleration and rotation are calculated for an IMU sample period. Different from GPS, the performance of IMU is not influenced by satellite signal strength. However, the errors of IMU add up over time, and lead to the decrease of the accuracy in positioning and orienting (Puente et al., 2013). It

should be noted that the errors can be compensated by the high accurate positioning information from a GPS; while the positioning accuracy of GPS can be also improved. Thus, the integration of the GNSS/IMU is able to provide a high accurate position and orientation for the MLS system.

**The DMI** is installed on the one of the vehicle's rear wheels to estimate the traveled distance (Talaya et al., 2004). The DMI offers the observation to help constrain the error drift when the vehicle locates in an area where tall buildings block the view of the sky.

### **2.1.2 A Mobile Laser Scanning System**

A vehicle-mounted MLS system is used in the mapping of roads and urban public space. It can offer sufficient speed to keep pace with the traffic and acquire a large amount of dense and precise point cloud dataset for various surveying tasks (Kukko et al., 2012). The MLS point clouds contain intensity data that can be applied to detect urban infrastructures automatically, such as buildings, pavement, roads, curbs, markings, manholes, traffic sign, poles and pylons. As shown in Figure 2.1, the environment is rendered with the intensity data of point cloud in greyscale where the road markings are distinguished. The MLS system RIEGL VMX-450 is mounted on the rear of the vehicle. It contains two tilted laser scanners, each scanner has a 360° field of views and their scan direction is counter-clockwise. The tilted angle of the scanners is 35 °, and the yaw offset is ±30 °. With the scanners' tilted angle of 35 ° and the yaw offset of ±30 °, this configuration is call “Butterfly” or “X” pattern. As the vehicle moves along the road, the navigation system based on GPS, IMU and DMI tracks the vehicle's trajectory and attitude for direct geo-referencing of laser scanning data. Due to the different position, movement speed, scan frequency and number of the scanners, the characteristics of the

obtained point cloud are different from airborne laser scanning (ALS) data, such as point pattern, distribution and point density. The flatness of the terrain and absence of tall targets result in the significant drop of the point density beyond 30 m (Guan et al., 2014). There are other factors that impact the point density, such as the vehicle speed, scan frequency and point measurement rate.

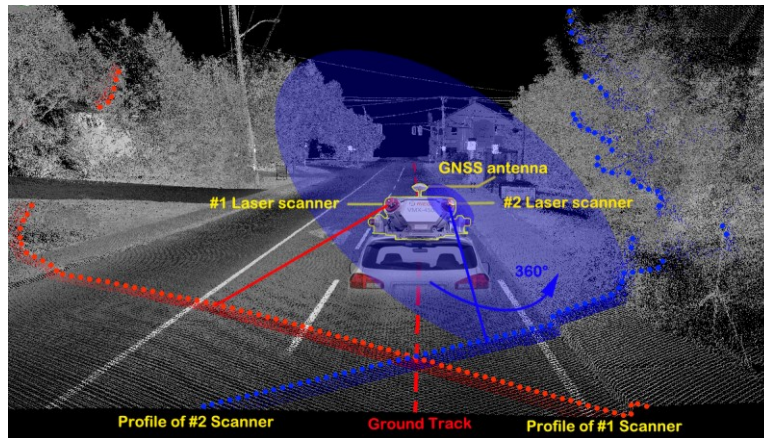


Figure 2.1: A Mobile Laser Scanning system.

### 2.1.3 Geo-referencing of MLS Data

The principle of geo-referencing is illustrated in Figure 2.2. The laser scanner is able to locate  $P$  point in its coordinate system by measuring scan angle  $\alpha$  and scan range  $d$ . Then the position of  $P$  in scanner system is transformed into the coordinate system of the mapping frame.



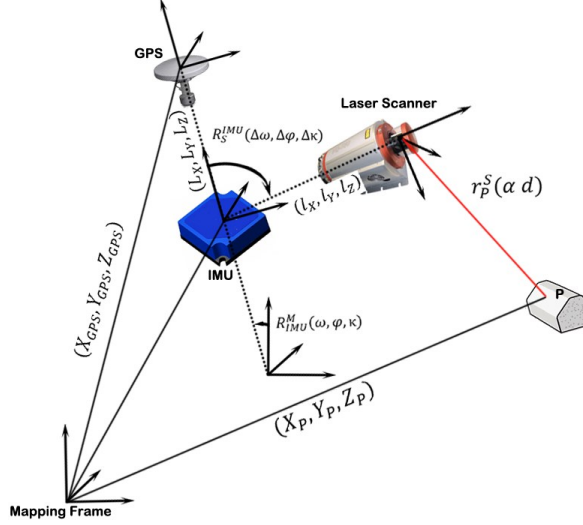


Figure 2.2: Principle of Geo-referencing.

The parameters that are used in the geo-referencing method is summarised in Table 2.1:  $[X_P, Y_P, Z_P]^T$  indicates the location of target P in the mapping frame coordinate system;  $[X_{GPS}, Y_{GPS}, Z_{GPS}]^T$  represents the position of the GPS antenna in the mapping frame;  $\omega, \varphi, \kappa$  indicates the rotation matrix from the IMU coordinate system;  $\alpha$  and  $d$  refers to the scan angle and range of the laser beam; and the others are the parameters that is determined by system calibration and measurement (Barber et al., 2008).

Table 2.1: Parameters of the geo-referencing equation.

Parameters	Description	Source
$X_P, Y_P, Z_P$	Coordinate of target P in mapping frame.	
$X_{GPS}, Y_{GPS}, Z_{GPS}$	Coordinate of GPS antenna in mapping frame.	GPS antenna
$R_M^{IMU}(\omega, \varphi, \kappa)$	Rotation matrix from IMU coordinate system to mapping frame	IMU
$r_P^S(\alpha d)$	The vector from laser scanner to point P. $\alpha$ is the scan angle and $d$ is the scan range.	Laser scanner
$L_X, L_Y, L_Z$	The offsets from the GPS origin to the IMU origin.	System calibration and measurement
$l_X, l_Y, l_Z$	The offsets from the IMU origin to the laser scanner origin.	System calibration and measurement
$R_{IMU}^S(\Delta\omega, \Delta\varphi, \Delta\kappa)$	Rotation matrix from laser scanner coordinate system and IMU coordinate system.	System calibration and measurement

The coordinate of a target  $P$  can be calculated by equation 2.1:

$$\begin{bmatrix} X_P \\ Y_P \\ Z_P \end{bmatrix} = R_M^{IMU}(\omega, \varphi, \kappa) \cdot (R_{IMU}^S(\Delta\omega, \Delta\varphi, \Delta\kappa) \cdot r_P^S(\alpha d) + \begin{bmatrix} l_X \\ l_Y \\ l_Z \end{bmatrix} + \begin{bmatrix} L_X \\ L_Y \\ L_Z \end{bmatrix}) + \begin{bmatrix} X_{GPS} \\ Y_{GPS} \\ Z_{GPS} \end{bmatrix} \quad (2.1)$$

## 2.2 Road Surface Detection Using Mobile Laser Scanning Data

In order to extract the road markings efficiently, the first step is to extract the road surface from the large-volume raw MLS point cloud data. A variety of methods were developed to detect roads from LiDAR data. The generic road surface detection with MLS data schemes from (a) 2D features filtering, (b) scan line segmentation, (c) 3D geometric features filtering, (d) surface growing, (e) random sampling consensus (RANSAC), to (f) voxel-based algorithm.

In the 2D features filtering approach, the road surface is detected given its elevation value, point density and intensity value. Li et al. (2004a) designed a method named Density of Projected Point (DOPP) to segment the range image. They used the density of projected point as an important criterion for road extraction. Guan et al. (2015) implemented elevation filtering to remove the high objects from the geo-referenced intensity image, and a point-density filter to extract the road surface. Clode et al. (2007) developed a hierarchal classification method to extract road from off-road points, based on intensity and elevation information.

In the second category (scan line segmentation), the MLS data is split into scan lines (or row of a range image) before the extraction. The detection of the road edges is used to determine the region of the road surface. First of all, the raw MLS data was segmented into profiles by a profiling process, and then processed by different algorithms. McElhinney et al. (2010) removed high elevations from the profiles and calculated the

rapid changes in the slope of the spline. The nearest points with the greatest changes were identified as the left and right edge of the road. Yang et al. (2013) implemented a moving window process on successive road cross section to detect border points of ground. Guan et al. (2014) detected curb points by the calculation of the slope and the elevation differences between a point and its neighbours in each scan line. Furthermore, the road surface can also be detected in each scan line separately. Manandhar and Shibasaki (2002) analyzed the histogram of height deviation of the points along the width of the road to extract the road surface. Zhao and Shibasaki (2002) also conducted a scan-line based classification by employing height deviation to separate the range points into building surface, road surface, other surfaces, windows, trees and others. In the study conducted by Smadja et al. (2010), RANSAC was implemented to detect the road boundary in each scan line.

In the third category (3D geometric features filtering), the road surface is extracted by a 3D features filtering. Hervieu and Soheilian (2013) calculated normal vector of each point and determined curbs and curb ramps based on its angular distance to normal vector of the ground. Liu et al. (2013) developed a digital elevation model using 2D sequential laser data. A probabilistic moving object deletion approach was utilised to remove the objects on the road. Then the slope and height variance between the curb candidate grid and adjacent grids were calculated for the identification of the curb grids.

In the fourth category (surface growing), Vosselman et al. (2004) introduced a surface growing algorithm to segment the point clouds into planes. The connectivity and smoothness of the plane, and the orthogonal distance between a candidate point and a plane were taken into account. Based on the surface growing segmentation, Pu et al.

(2011) defined and categorized all the feature types regarding geometric attributes and topological relations. In a rough classification, the road surface segments were extracted based on the distance to the vehicle trajectory.

In terms of the ground removal methods, Zhou et al. (2012) implemented RANSAC to fit the planes of the road surface, and the points within a distance to the planes are extracted as the ground. Cabo et al. (2013) simplified the point cloud approach based on the space regular voxelization. All voxels were segmented into horizontal slices, and the fragments of target poles were grouped and extracted in 2D sections. In the end, the tridimensional neighborhood analysis was applied to the grouped voxels of each pole, and the slices of the targets join to its neighbours to reconstruct the target poles. Yu et al. (2015) partitioned point data into an octree structure with a voxel size. For each voxel, it grew upward to its 9-neighbour voxels, and then the growing scheme continued until reached the top boundary. If the elevation of the top voxel smaller than the predefined threshold, the cluster of these voxels is regard as ground and the point clouds were labeled as ground points.

Four categories of road surface detection techniques were summarised in Table 2.2. The application of the elevation, point-density and intensity filtering is simple and fast, but the extraction results are in relatively low accuracy. The scan-line based segmentation focuses on the detection of the road edges or curbs based on the elevation changes in each scan line. A rapid change of slope is employed to distinguish curb or road border from the ground (McElhinney et al., 2010; Yang et al., 2013; Guan et al., 2014). Different from road edge detection, some studies aimed at extracting the road surface directly according to its smoothness. One of the main parameters in this method is the height deviation that

measures the smoothness (roughness) of the surface (Manandhar and Shibasaki, 2002; Zhao and Shibasaki, 2002). Compared with scan-line based segmentation, 3D geometric features filtering is able to extract road surface in a global scale. Hervieu and Soheilian (2013) calculated the normal vectors of the points to detect the curb and curb ramps. Liu et al. (2013) transformed a 3D problem into a 2D problem, making their method faster than Hervieu and Soheilian's method (2013). In addition, the surface growing algorithm takes the coplanarity and connectivity into the consideration and detects the road surface in a global scale but in a time-consuming manner.

Table 2.2: Summary of different road surface detection techniques.

Method	Information	Advantages	Limitations	Examples
2D features filtering	<ul style="list-style-type: none"> <li>●Point density</li> <li>●Elevation</li> </ul>	<ul style="list-style-type: none"> <li>●Straightforward</li> <li>●High computational efficiency</li> </ul>	<ul style="list-style-type: none"> <li>● Difficult to handle steep terrain</li> <li>● Cannot remove the wheels from the road</li> </ul>	<p>Distinguishing ground and building by calculating density of projected point (Li et al., 2004a)</p> <p>Removing the high object by elevation filtering and extract road surface by point-density filtering (Guan et al., 2015).</p>
	<ul style="list-style-type: none"> <li>●Point intensity</li> <li>●Elevation</li> </ul>	<ul style="list-style-type: none"> <li>●Straightforward</li> <li>●High efficiency</li> </ul>	<ul style="list-style-type: none"> <li>● Cannot detect boundary lines</li> </ul>	<p>Detection and vectorization of roads from LiDAR data by hierarchal classification with intensity and height values (Clode et al., 2007)</p>
Scan line segmentation	<ul style="list-style-type: none"> <li>●Edge of Road</li> </ul>	<ul style="list-style-type: none"> <li>●Detecting the accurate edge of the road surface in urban area</li> <li>●Without additional information, such as point density, point intensity</li> </ul>	<ul style="list-style-type: none"> <li>●The curb-based road detections fail in rural area</li> <li>●Need vehicle trajectory information for profiling</li> </ul>	<p>Initial results from European road safety inspection (EuRSI) mobile mapping project (McElhinney et al., 2010)</p> <p>Partitioning MLS into road cross sections to detect border points of ground (Yang et al., 2013)</p> <p>Curb-based road extraction based on rapid elevation changes through successive road cross section (Guan et al., 2014).</p>
	<ul style="list-style-type: none"> <li>●Height deviation</li> <li>●Scan range</li> </ul>	<ul style="list-style-type: none"> <li>●Detecting the road surface according to the smoothness of the road</li> </ul>	<ul style="list-style-type: none"> <li>●Need vehicle trajectory information for profiling</li> </ul>	<p>The histogram analysis was implemented along scan line to detect the height deviation and extract road surface (Manandhar and Shibasaki, 2002)</p> <p>Vehicle-borne laser range data was segmented by scan line, and the successive linear patches are extracted. Then the extracted patches were classified into the horizontal and vertical surface according to their orientations. (Zhao and Shibasaki, 2002)</p>
3D geometric features	<ul style="list-style-type: none"> <li>●Slope</li> <li>●Height difference</li> <li>●Normal vector</li> </ul>	<ul style="list-style-type: none"> <li>●Processing in Global scale</li> </ul>	<ul style="list-style-type: none"> <li>● The complex of the methods depends on calculation of the 3D features</li> </ul>	<p>Curb detection based on DEM built from UGV(Liu et al., 2013)</p> <p>Road side detection with angular distance to ground normal (Hervieu and Soheilian, 2013)</p>
Surface growing algorithm	<ul style="list-style-type: none"> <li>●Coplanarity (Normal vector) and</li> <li>●Connectivity</li> </ul>	<ul style="list-style-type: none"> <li>●Processing in Global scale</li> </ul>	<ul style="list-style-type: none"> <li>●Time consuming</li> </ul>	<p>Segment the laser point cloud with a surface growing algorithm.(Vosselman et al., 2004)</p> <p>The point clouds were partitioned by surface growing algorithm, and road surface segments were detected by the spatial relationship to vehicle trajectory. (Pu et al., 2011)</p>
RANSAC	<ul style="list-style-type: none"> <li>●Smoothness</li> </ul>	<ul style="list-style-type: none"> <li>●No need of trajectory information</li> <li>●High computational efficiency</li> </ul>	<ul style="list-style-type: none"> <li>●Accuracy depends on how the model fit the data</li> <li>●Cannot handle the terrain with large elevation variance</li> </ul>	<p>Implementing RANSAC to fit a plane for ground, and searching the ground points within a distance to the plane (Zhou et al., 2012)</p>
Voxel-based algorithm	<ul style="list-style-type: none"> <li>●Connectivity along vertical direction</li> </ul>	<ul style="list-style-type: none"> <li>●No need of trajectory information</li> <li>●High efficiency</li> </ul>	<ul style="list-style-type: none"> <li>● Cannot handle the terrain with large elevation variance</li> </ul>	<p>Implementing voxelization and partitioning the voxels into horizontal slice to analyze and extract the pole voxels. (Cabo et al., 2013)</p> <p>Applying voxel-based upward growing to remove ground point from entire point clouds (Yu et al., 2015)</p>

## **2.3 Road Marking Extraction Methods**

In general, the road markings have much higher reflectance than the unpainted road surface. Therefore, their relatively high intensity can be used for detecting the road markings with the assistance of different data sources. Based on data sources, the studies can be categorized into two groups: (a) digital images or videos based and (b) mobile laser scanning data based.

### **2.3.1 Images and Video-based Road Marking Extraction**

The use of digital images and videos for road marking extraction has been investigated for years. This extraction consists of two steps: candidate extraction and road marking classification. Taking the study of Kheyrollahi and Breckon (2010) as an example, they implemented a multi-level-threshold segmentation to detect the candidate road markings. A set of connected contours were extracted from the binary images. Based on the shape of the road markings, artificial neural network were utilised to classify these road markings.

In order to overcome the difficulty of inconstant luminance, road markings were identified with local thresholding. Beside the multi-level-threshold segmentation, Kheyrollahi and Breckon (2012) processed the image line by line and identified the left and right boards based on the changes of the luminance along the lines. Wang et al. (2009) and Mathibela et al. (2015) applied Inverse Perspective Mapping (IPM) to transform the perspective image into a top-view image and implemented steerable filter (Freeman and Adelson, 1991) to detect the lane markings. The image was then segmented by lane markings and arrow markings were extracted using the Otsu thresholding (Otsu, 1979). These methods avoided the application of global thresholding for the extraction

process and explored different partitioning strategies to segment the MLS data into data stripes/profiles to avoid spatial variance.

One of the main challenges of the images and videos based extractions is the inconstant luminance of road markings and pavements. The process of measuring the reflected sunlight inherits the disadvantage of passive remote sensing. Various factors would affect the detection of road markings, such as weather, time of day, moving vehicles and shadows (see Table 2.3). Equipped with active sensors, MLS systems have a good performance in detecting road markings. First of all, the detection is weather and sunlight independent. The MLS systems can work in cloudy weather, without shadows occurring on the road surface and operate at night avoiding the dense traffic. However, some factors would impact the intensity data measured by MLS systems, such as scan range, incidence angle and surface properties (see Table 2.3). Similar to the images/videos-based methods, the MLS-based methods have their own “inconstant luminance” issue. The details will be further discussed in Section 2.3.5.

Table 2.3: Summary of impacts of road marking extraction.

Data source	Impacts	Description
Images and videos	Weather	Cloudy weather reduces the contrast between markings and pavements.
	Time of day	Cameras can be used only during day time.
	Occultation	Vehicles on the road cover the road marking. Pedestrians walk through zebra crossing.
	Shadows	Shadows of buildings, trees and vehicles reduce the luminance of the road marking.
MLS data	Scan range	Atmospheric attenuation
	Incidence angle	Lambert's cosine law
	Surface properties	The surface roughness, grain properties and albedo determine the intensity of the road markings.



### 2.3.2 MLS Based Road Marking Extraction

In the MLS systems to extract the road markings, the first step is to distinguish road surfaces points from raw MLS data. The road markings are then detected based on their high reflectance in the form of laser intensity. Based on the MLS data, the road marking extraction process can be classified into three categories (a) global intensity filtering, (b) global intensity filtering with preprocessing, (c) multi-thresholding segmentation.

With regard to global intensity filtering, Smadja et al. (2010) implemented a simple threshold on intensity for detecting the road markings. Toth et al. (2008) selected an intensity value based on the intensity distribution in a search window as a global threshold for the extraction. Yang et al. (2012) extracted continuous edge lines and broken lane line markings successfully. First of all, a two-step filtering was undertaken to MLS point clouds based on intensity and elevation information. The markings were then detected according to their patterns and arrangements. However, there were some noises in those three road marking results due to unevenly distributed intensity of point clouds.

To eliminate the intensity variance caused by the unevenly distributed point clouds, Jaakkola et al. (2008) conducted a study to correct the intensity data before extraction. They projected the MLS point clouds into the raster images, and used image-processing algorithms to extract markings. First of all, the intensity image was profiled by column in the study. Along the profile, a second order curve fitted the median intensity measurements to reduce the variance of the measured intensity value. After radiometric correction, a 3-by-5 average filter was applied for denoising the corrected image. Then a constant threshold was used to extract road markings.

Studies were also undertaken aiming at solving the problem caused by inconstant

intensity. Chen et al. (2009) selected the intensity peaks along the scan line as lane marking points by using adaptive thresholding. Vosselman (2009) proposed a distance-dependent thresholding method to detect the road markings, and a connected components analysis to extract road markings. In Vosselman (2009), the threshold was expressed as a function of the distance to overcome the disturbance of inconstant intensity. Kumar et al. (2014) applied a range dependent thresholding function to extract road markings from intensity and range images. The strategies used by Vosselman (2009), Kumar et al. (2014) and Chen et al. (2009) can be concluded as an equivalence of the transverse multi-thresholding segmentation. The algorithm proposed by Chen et al. is a transversal segment, while the methods proposed by Vosselman (2009) and Kumar et al (year) are a longitudinal segmentation. In other studies, the distance-dependence of intensity was used in different ways (Guan et al, 2014; Yu et al, 2015).

Guan et al. (2014) implemented point-density-dependent multi-thresholding segmentation to extract road markings. The distribution of point density along the cross section was fitted to a Gaussian normal distribution function. The road surface points were segmented into some bins according to the range  $r$  that was calculated by the estimated mean  $\mu$  and standard deviation  $\sigma$ . Yu et al. (2015) applied a distance-dependent multi-thresholding segmentation in which the road surface points were segmented into the blocks along the road. A distance-based segmentation was then used to partition the blocks into segments, in which each segment was threshold by Otsu method individually. Table 2.4 summarizes the advantages and limitations of the three categories of road marking extraction from MLS data.

Table 2.4: Summary of road marking detection techniques from MLS data.

Method	Information	Advantages	Limitations	Examples
Global intensity filtering	<ul style="list-style-type: none"> <li>●Intensity</li> </ul>	<ul style="list-style-type: none"> <li>●Simple</li> </ul>	<ul style="list-style-type: none"> <li>●Inaccurate extraction result</li> </ul>	Using road pavement markings as ground control for LiDAR data (Toth et al., 2008). A simple global intensity filtering was implemented to extract road markings (Smadja et al., 2010).
Global intensity filtering with preprocessing of intensity	<ul style="list-style-type: none"> <li>●Intensity</li> <li>●Distance to vehicle trajectory</li> </ul>	<ul style="list-style-type: none"> <li>●Removing some variance of road markings by intensity correction</li> </ul>	<ul style="list-style-type: none"> <li>●Distance-dependent correction is rough</li> </ul>	The intensity values were corrected radiometrically with distance prior to a global intensity filtering (Jaakkola et al., 2008).
Multi-thresholding segmentation	<ul style="list-style-type: none"> <li>●Distance to vehicle trajectory</li> </ul>	<ul style="list-style-type: none"> <li>●Eliminating the influence of inconstant intensity by multi-thresholding</li> </ul>	<ul style="list-style-type: none"> <li>●The intensity variance of road marking remains in segments and disturbed the extraction process</li> <li>●Partitioning relies on the information of the navigation trajectory</li> </ul>	Selecting the intensity peaks along the scan line as road marking points (Chen et al., 2009). Expressing the threshold as a function of distance to extract road marking (Vosselman, 2009; Kumar et al., 2014). Point-density-dependent multi-thresholding segmentation for road marking extraction (Guan et al., 2014). Distance-dependent multi-thresholding segmentation for road marking extraction (Yu et al., 2015).

It is noted that the inconstancy of the intensity value may result in errors in the extraction results. Therefore, multi-thresholding segmentation was employed to minimise the impact of the inconsistent intensity (Vosselman, 2009; Kumar et al., 2014; Guan et al., 2014; Yu et al., 2015). Based on the findings from literature review, there are three research gaps in the field of road marking extraction from MLS. Firstly, limited studies were conducted on the challenging dataset from the conditions of cracking, rutting, potholes and decay. Therefore, this study concentrated on two different study areas to explore the extraction of deficient road markings in poor road conditions.

Secondly, majority of the research did not undertake radiometric correction for reducing intensity variance before road marking extraction except the study conducted by Jaakkola et al. (2008). Thus, this study aims at introducing an improved radiometric correction of laser intensity for road marking extraction to improve the road marking extraction result.

Thirdly, most of studies were conducted on reducing intensity variance by multi-thresholding segmentation (Vosselman, 2009; Kumar et al., 2014; Guan et al., 2014; Yu et al., 2015), without the implement of the window based method to overcome the unevenly distributed intensity. Although multi-thresholding segmentation can reduce the in-class variance in each segment, some intensity variances would remain in the traversal and longitudinal segments. Because of the size of the window is small, window based method could result in less intensity variance than the traversal and longitudinal segments. Thus, the window based method should be used to improve the road marking extraction, especially in overcoming the unevenly distributed intensity issue, and improving the road marking extraction result in this thesis.

### **2.3.3 Scanning Range and Incidence Angle Effects on MLS intensity**

A laser light, as the near infrared light, follows the reflection and transmission of electromagnetic radiation. The strength of its intensity measured by a scanner depends on the range from the laser point to the scanner, the incidence angle of a laser beam and the material property.

Kaasalainen et al. (2011) analyzed the impacts of the range and incidence angle on the intensity measurements from terrestrial laser scanners (TLS). In their study, the radar equation was used as below (Wagner et al., 2006)

$$P_r = \frac{P_t D_r^2}{4\pi R^4 \beta_t^2} \sigma \quad (2.2)$$

where  $P_r$  is the received power,  $P_t$  is the transmitted power,  $D_r$  is the receiver aperture,  $R$  is the range, and  $\beta_t$  is the transmitter beam width.  $\sigma$  is the backscatter cross section. Assuming all variables are constant, the previous equation can be simplified to

$$P_r = \frac{K}{R^2} \quad (2.3)$$

where  $K$  is a constant, representing a combination of the variables  $P_t$ ,  $D_r$ , and  $\beta_t$ . The geometry and parameters involved in the radar equation are presented in Figure 2.3. The laser scanner emits the waves, the receiver captures diffusion reflected waves and measures the intensities. The transmitter and receiver are side by side at the same location, while the transmitter and receiver are drawn at different locations for clarity.

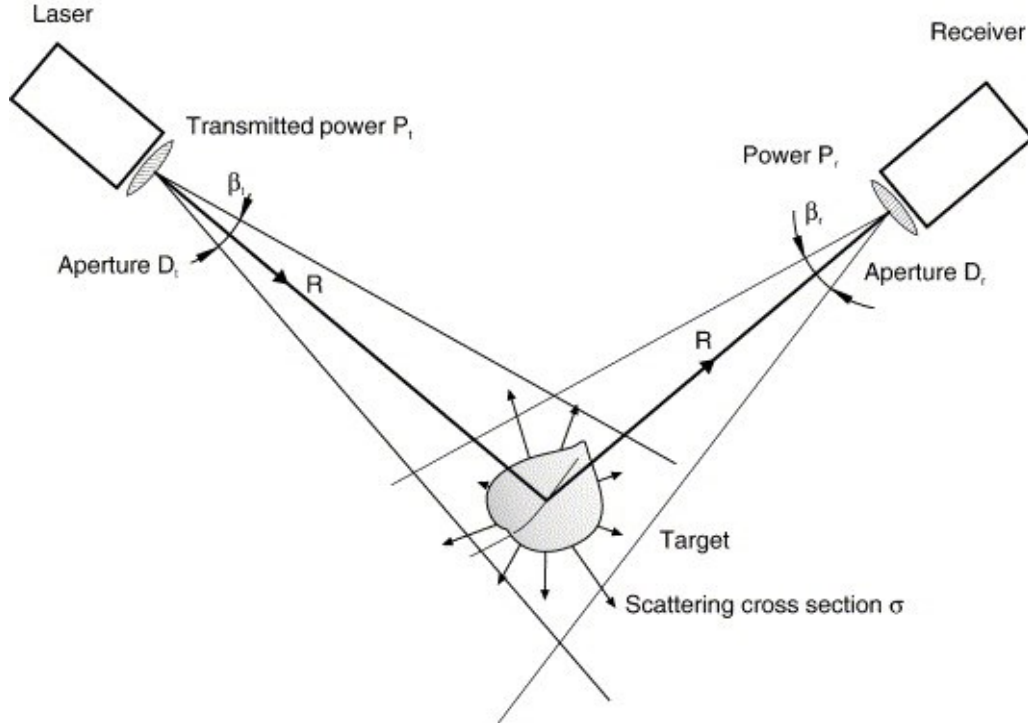


Figure 2.3: Geometry and parameters involved in the radar equation (Source: Wagner et al., 2006).

The experimental results from the study conducted by Kaasalainen et al. (2011) indicated that the intensity values roughly follow the  $K/R^2$  prediction (Equation (2.3)) at ranges of 10-15 m and further. At a small distance, the intensities recorded in different TLS datasets deviate significantly from Equation (2.3). Measured intensity obtained from other kinds of TLS decreases due to other factors, such as a brightness reducer for near distances. Thus, the efficiency of intensity correction depends on the type of the scanner. Another limitation of the correction is the estimation of the scan range. Without the support of raw range data, the calculation of the scan range requires the utility of the trajectory information that increases the complexity of the correction. Although the scan range can be estimated by dividing the height of scanner by the cosine of the scan angle rank, the error will be amplified by the  $K/R^2$  prediction, which leads to a non-linear relationship between  $1/R^2$  and the measured intensity.

In the study on incidence angle effects on the intensity measurements, an empirical correction function was introduced to use incidence angle to express received intensity (Kaasalainen et al., 2011):

$$I(\theta) = a(\omega, g)(1 - b(\omega, g)(1 - \cos \theta)) \quad (2.4)$$

where,  $\theta$  represents the incidence angle,  $a$  is the value of intensity,  $\omega$  is the reflectance or albedo, and  $g$  is the grain size of the material.  $\theta = 0$ ,  $b = 0$  indicates that there is no Lambertian component, while  $b = 1$  represents a fully Lambertian behavior ( $I(\theta) = a(\omega, g) \cos \theta$ );

For extraction of road marking, the material property of markings is same. In the case that the material property of marking is same, the albedo  $\omega$  and grain size  $g$  are constant. Note that,  $a(\omega, g)$  and  $b(\omega, g)$  are proportional to  $\omega$  and  $g$ . Thus, they are constant too.

As a result, Equation (2.4) can be simplified as below:

$$I(\theta) = A + B \cos \theta \quad (2.5)$$

where,  $A$  and  $B$  are the constants that depend on the albedo and grain size of the material. Therefore, the intensity value received by the scanner can be corrected with incidence angle  $\theta$ . However, an accurate incidence angle can only be calculated using the direction of the laser beam and normal vector of the surface, which is time-consuming with massive calculations. A simple and rough way to get the incidence angle is to employ the scan angle rank recorded in MLS data as an estimator. The scan angle rank ranges from  $-90^\circ$  to  $+90^\circ$  within  $1^\circ$  accuracy (ASPRS Standards Committee, 2011). It is an angle based on  $0^\circ$  being the nadir.  $-90^\circ$  to the left side of the direction of trajectory. The absolute value of the scan angle rank is close to incidence angle when the ground surface is planar. The cosine of the scan angle rank will be used to correct the intensity value according to Equation (2.5) in Section 3.3.3. Because the range based correction is more sensitive to the cross slope of the road than the scan angle based correction, this study only explores the latter method.

Besides the incidence angle, the surface roughness also plays a critical role in the optical scattering. The rougher the surface, the higher intensity the pavements have. Because pavement surface is polished by road traffic, the point clouds of pavements would have various intensity values. Therefore, the intensity correction based on Equation (2.5) is not able to eliminate the variance of intensity caused by different roughness of pavements.

## **2.4 Road Marking Classification**

The classified road markings offer a precise lane geometry with lane boundaries and rich attributions such as lane types, traversal information, marking types and speed limit information. Thus, the information of road markings can help to build the detailed lane model and support driverless cars and advanced driver assistance systems. With the increasing demands for detailed 3D road network update, the techniques in detecting and recognising road markings from MLS were developed in recent years. Based on the image, video and point cloud based algorithms, the classification of road markings commonly consists of three steps: splitting road markings into objects, extracting features of objects and recognizing road marking objects.

### **2.4.1 Road Marking Isolation**

Each isolated road marking has its shape that can be used to distinguish it from others. The first stage is to segment the whole road markings into the portions for recognition. The road marking isolation can be classified into three categories: (1) the Hough transform, (2) the contour-based analysis and (3) the region-based analysis.

#### (1) Hough transform

As one of the most common post-processing techniques used in line road marking detection, it was used to transform to detect rectilinear markings, such as lines, dashed lines and zebras (Rebut et al., 1997). Li et al. (2004b) also applied a multiresolution Hough-transform-based algorithm for detecting and tracking of road contours. Chen et al. (2009) implemented Hough transform clustering to extract candidate markings. In theory, the Hough transform is efficient, but can only be used to detect line shape road markings.

#### (2) Contour-based analysis



Another strategy for isolating the road markings is by detecting the contour of the road markings. Li et al. (1997) applied a fuzzy-reasoning-based general technique for edge detection. It classified a pixel in an image to a region according to luminance gradient between the pixel and its neighbours. Kheyrollahi and Breckon (2010) also employed a contour-based approach to isolate the pixels of road markings, and then simplified the isolated shapes into a closed polygon shape representation using the Douglas–Peucker derivative (Wu and Márques, 2003).

### (3) Region-based analysis

Franke et al. (1998) implemented a colour-connected component (CCC) extraction to segment images to produce a database containing candidates of road markings. Maximally Stable Extremal Regions (MSERs) was used to prune the image to partition as the candidates of road markings (Wu and Ranganathan, 2012). Foucher et al. (2011) detected road marking objects as connected components based on their geometric parameters, such as minimum bounding rectangle and the rectangularity. Euclidean distance clustering was also employed on unorganized and insular road marking points to obtain candidate road marking clusters (Yu et al., 2014).

#### **2.4.2 Feature Extraction**

Feature extraction retrieves the shape information (e.g. geometric parameters and descriptors) to facilitate the shape recognition. Yang et al. (2008) compared and discussed the characteristics and performances of various shape-based feature extraction approaches (see Figure 2.4). It should be noted that majority of the road markings are line-shaped or rectangular, therefore, only a portion of shaped based extraction techniques were used in road marking recognition studies.

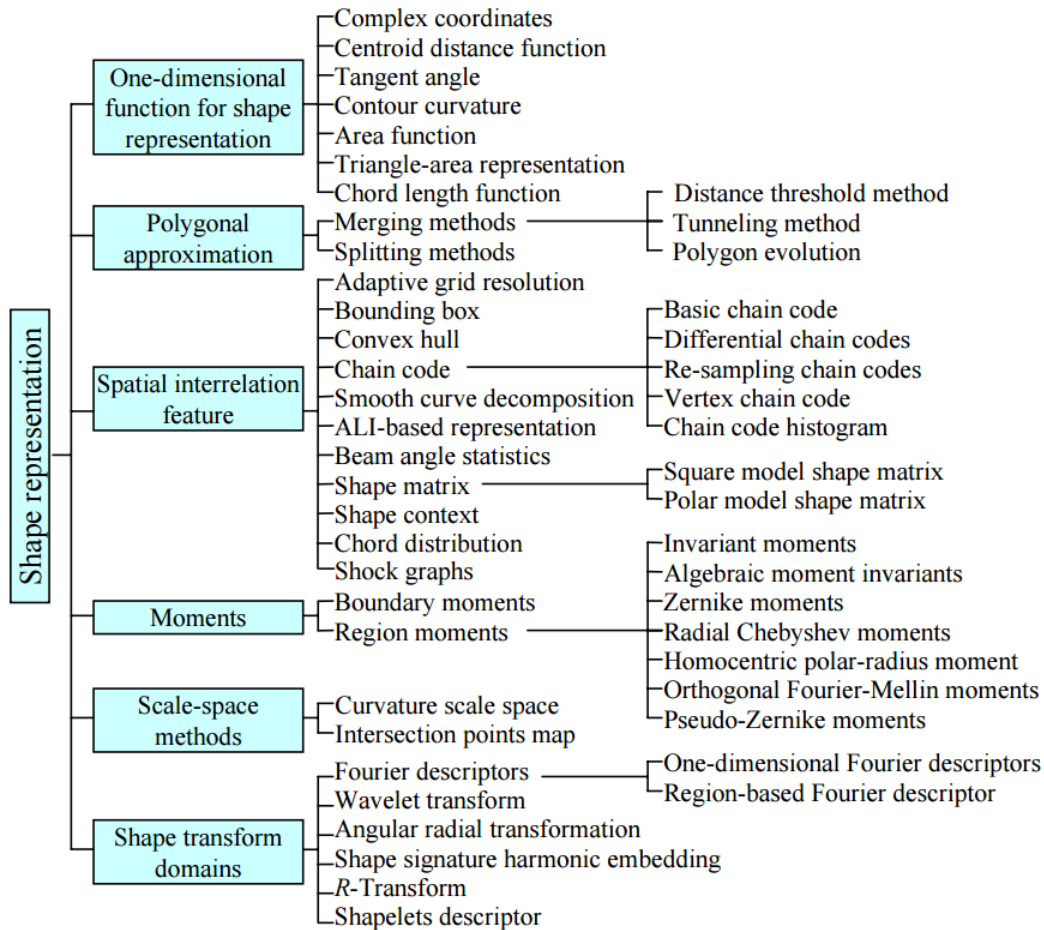


Figure 2.4: An overview of shape description techniques. (Source: Yang et al., 2008)

Franke et al. (1998) computed the attributes of all segmented regions for road marking recognition and employed the template matching method on the distance transform images. The attributes are the area, bounding box, aspect ratio, length, and smoothness of contour. Rebut et al. (2004) used one-dimensional Fourier descriptor as the shape signatures for the recognition of the road arrows. Li et al. (2007) identified arrow markings based on the shape information, such as chain code, moment features, length and aspect ratio of a minimum bounding box. Tournaire et al. (2007) used various variables (i.e. centroid and orientation, the width and the length) to describe rectangular marking. In addition, a projection based method was used to determine the ROI of arrow

markings, describe arrow markings with wavelet feature, and then recognize the markings with SVM classifier (Wang et al., 2009). Kheyrollahi and Breckon (2010) calculated many feature placement of simplified contour shape for classification, including the aspect ratio of the glyph (i.e. height divided by width), normalized central moment, horizontal/ vertical projection of the glyph and fuzzy zoning of angles. Danescu and Nedevschi (2010) applied RANSAC to extract the edge lines of the road markings, and then classified the markings based on three characteristics. The first character is the ratio between the outliers and the total number of points on a border line. The second one is the deviation from the line for the outliers. The third one is the position of points with the maximum number of error on each side. Foucher et al. (2011) calculated the minimum bounding box of connected components in an image and then classified the components into crosswalks and arrows by their areas, rectangularity and profiles. Wu and Ranganathan (2012) detected corners in road marking regions, labeled the corners as the points of interest (POI), then calculated the histogram of oriented gradients (HOG) of each POI as the features of the shape. A routine template matching was implemented to recognize the road markings. Yu et al. (2014) classified the road markings based on the size of marking, the direction of marking (variance between the orientation of marking and the direction of trajectory/curb-lines) at the first level of hierarchical classification. At the second level of hierarchical classification, the small road markings were rasterized into 2-D binary images with a size of  $n \times n$ . Each 2-D binary images correspond to an  $n \times n$  dimension vector. Since the  $n \times n$  dimension vector is the feature vector representing a specific template, it changes when the 2-D image is rotated. In addition, each small road markings consists of four directional templates, including south to north, west to east,

southeast to northwest and southwest to northeast. Based on these 2-D images, the Deep Boltzmann Machine (DBM) (Salakhutdinov and Hinton, 2009) was designed and developed for the classification of these small road markings. Hervieu et al. (2015) projected the point cloud vertically to generate an ortho-image, and the intensity value of the lowest projected point was set to the pixel. The intensity image was classified by Model&data-driven Reversible Jump Markov Chain Monte Carlo (RJCMCMC) algorithm. The RJCMCMC sampler was applied to check whether the target is similar to the road marking pattern. With the assistance of a simulated annealing, the sampler process detected the road markings through the minimization of the output of the energy function.

A number of geometric parameters are used as representatives of the markings shapes in the road marking classification. Table 2.5 summarized the geometric parameters that can be used to describe the features of the road markings, and the shape descriptors that are used in road marking classification.

Table 2.5: Summary of different geometric features of road marking shape.

Shape parameters	Description	Examples
Area	The number of pixels in the shape	Franke et al. (1998) Foucher et al. (2011) Yu et al. (2014) Danescu and Nedevschi (2010)
Perimeter	The number of pixels in the boundary of the shape	Franke et al. (1998) Tournaire et al. (2007) Mathibela et al (2015)
Compactness/ Circularity	How closely-packed the shape is	
Eccentricity	The ratio of the length of the major axis to the length of the minor axis. Measurement of aspect ratio	Franke et al. (1998) Li et al. (2007) Kheyrollahi and Breckon (2010)
Rectangularity	How much it fills its minimal bounding box: ratio of object/area	Foucher et al. (2011)
Circularity	Smoothness of contours, ratio of $(4 \times \text{PI} \times \text{Area}) / (\text{Perimeter}^2)$	Franke et al. (1998) Danescu and Nedevschi (2010)
Orientation	The overall direction of the shape	Tournaire et al. (2007) Yu et al. (2014), Mathibela (2015)
Centre of gravity	Centroid of the shape	Tournaire et al. (2007)
Advanced shape descriptors	Description	Examples
Moment	A statistical properties to describe shape	Li et al. (2007) Kheyrollahi and Breckon (2010)
Chain Code	The contours are described as a connected sequence of straight-line segments with given lengths and directions (Zhang and Lu, 2004; Liu et al., 2007).	Li et al. (2007) Kheyrollahi and Breckon (2010)
Shape matrix	Shape matrix is an $m \times n$ matrix to present a region shape	Yu et al. (2014)
Minimum bounding rectangle	The smallest rectangle that contains every point in the shape	Franke et al. (1998), Li et al. (2007) Foucher et al. (2011) Hervieu et al. (2015)
Profiles	The profiles count the number of pixels in the region in each row/column on Cartesian coordinate system (Yang et al., 2008).	Wang et al. (2009) Kheyrollahi and Breckon (2010) Foucher et al. (2011)
One-dimensional Fourier descriptors	A one-dimensional function derived from contour coordinates by applying Fourier transform	Rebut et al. (2004)
Wavelet transform	The wavelet descriptor decomposes a contour into components of different scales containing global and local information respectively. (Yang et al., 2008).	Wang et al. (2009)
Shape transform	Distance transformation converts a binary digital image, consisting of the target and non-target pixels, into an image where all non-target pixels have a value corresponding to the distance to the nearest feature pixel (Borgefors, 1986).	Franke et al. (1998)
	Histogram of oriented gradients (HOG) counts occurrences of gradient orientation in localized portions of an image (Dalal and Triggs, 2005).	Wu and Ranganathan (2012)

Compared to images or videos acquired from the camera sensors, MLS data has fewer limitations and disturbances for the road marking extraction. Additionally, the result retrieved from the MLS-based extraction is more comprehensive and accurate than the one obtained from the image or video-based extraction method. It was also identified that since the location and rotation of the road markings cannot affect the shape of the road markings, the geometric features used by road marking classification need be both translation and rotation invariant.

### **2.4.3 Classification Methods**

A number of supervised classification methods were developed for recognizing road markings.

Danescu and Nedeveschi (2010) classified the road markings by defining a decision tree based on the shape of the road markings. Li et al. (2007) generated a Bayes classifier with minimum error rate training In which over 5000 samples of five different road markings were used to train the classifier. Kheyrollahi and Breckon (2010) manually extracted 1022 sample glyphs from real road footage sequences and trained the artificial neural network (ANN) classifier for recognising road markings. Additionally, zebra crossing and arrows were defined as a repetitive pattern and a single pattern respectively in the study conducted by Foucher et al. (2011). With the criterion of size, Firstly, based on the difference of size, the zebra crossing and arrows were identified from other road markings. These two markings will be further separated based on their difference on orientation, rectangularity, vertical and horizontal profiles. Wu and Ranganathan (2012) generated the feature vectors from HOG for each POI in all template images, and all of these feature vectors were stored in the template pool. Then road markings were

identified by the template matching method based on the template pool. Taking the numerous noise sources (i.e. shadows, sun/headlight/streetlight reflection, road surface debris and decay) into consideration, Rebut et al. (2004) trained K-Nearest Neighbour (KNN) classifier with the noise-added training base. The Fourier descriptors were utilised to describe the shapes of the road markings. Wang et al. (2009) also designed a multi-class support vector machine (SVM) to classify arrow markings based on the hierarchical classification method. The SVM classifiers at the nodes of the hierarchical tree were trained to form the hierarchical classification. Based on the Euclidean distance clustering result of road marking points, Yu et al. (2015) trained the DBM model with 2-D images of small-sized road markings, and the small-sized road markings were then classified into the various categories (i.e. arrow markings, rectangular-shaped marking, pedestrian warning marking and other markings). Mathibela et al. (2015) classified the road markings into seven distinct classes within a Conditional Random Field (CRF) and probabilistic RUSBoost classification framework by employing a set of geometric feature functions.

It was identified from the review that machine learning algorithms were widely used for road marking recognition, except the study conducted by Danescu and Nedevschi (2010) in which rules were encoded in a simple decision tree to classify the road markings. It is noted that the machine learning algorithms require training of the samples to determine whether a candidate matches a model sufficiently. In addition, the success of the road markings classifications relies on the quality and quantity of training dataset. There was a positive correlation between the number of the training samples and the performance of the machine learning algorithms. On the other hand, manually building

the decision tree relies on the strong prior knowledge. It is clear that the pavement marking guide, as strong prior knowledge, can be easily encoded in the decision tree as rules while the machine learning algorithms need training process.

Based on the prior knowledge of road marking shapes, three geometric parameters are selected to be considered in feature extraction, including area, width and orientation. The detailed feature extraction methods will be discussed in Section 3.5.2.

Based on the findings from literature review, limited research classified the road markings into thorough and detailed categories. The roughly classified results would be sufficient to support the maneuver of driverless cars. Thus, there is a need to improve the detailed classification of the road markings in this research field.

## **2.5 Chapter Summary**

In this chapter, the fundamental knowledge of the MLS technology and the literature on road surface extraction from MLS data were reviewed. A variety of studies on the road-marking extraction and recognition from the digital images/videos and MLS data are discussed. It is identified that the MLS data is more suitable than digital images/videos to detect and recognize the road markings. A hybrid road surface extraction will be applied in the experiments of this study. A scan-angle-rank-based intensity correction will be undertaken to improve marking extraction. Based on the strong prior knowledge of the marking shapes, a decision tree will be constructed manually to classify the road markings into detailed types.



## Chapter 3 Proposed Method

This chapter provides an overview of workflow for road marking extraction and classification, and the method adopted in this research. Section 3.1 introduces the study area and test datasets, followed by an overview of the proposed workflow presented in Section 3.2. The workflow is divided into three stages, including preprocessing, extraction and classification, which will be discussed in Section 3.3, 3.4 and 3.5 respectively. Section 3.6 summarizes this chapter.

### 3.1 Study Area and Dataset

Two study areas were selected within this research, one is located in the City of Xiamen (see Figure 3.1(a)) and the other is in the City of Kingston, Ontario (see Figure 3.1(b)). Xiamen is a port city on the southeast coast of mainland China. A complete survey of mobile laser scanning was carried out back and forth on Xiamen Island Ring Road on 23 April 2012 by a RIEGL VMX-450 system. The Ring Road is a two-side, four-lane road with a centre median. The total length for one direction survey was around 10 km. This primary road in Xiamen is characterized by numerous vehicles, trees, shafts (e.g., light poles and traffic poles). The majority of the road surface and road markings are in good condition. Seven samples of the survey data (i.e. the straight, curve roads and different types of road markings) were selected as the test dataset for evaluating the proposed method.

The King Street in the City of Kingston, Ontario was selected as another study area to test the robustness of the proposed method in Canada's road network, see Figure 3.1(b). A survey was carried out five times along the King Street, and the point cloud data was collected on August 29, 2013 by a RIEGL VMX-450 system from the Tulloch

Engineering. Different from Xiamen’s Island Ring Road, King Street is a two-side and two-lane local road. The residential houses and sidewalks are located along the road sides. Due to the winter maintenance operations and road traffic, pavement markings are deficient in the sample of Kingston. Thus, the Kingston datasets are more challenging than the Xiamen datasets. In this study, the Xiamen datasets were used in the early stage of the experiment to assist the algorithm configurations, and the Kingston datasets were employed to test the robustness of the proposed method.

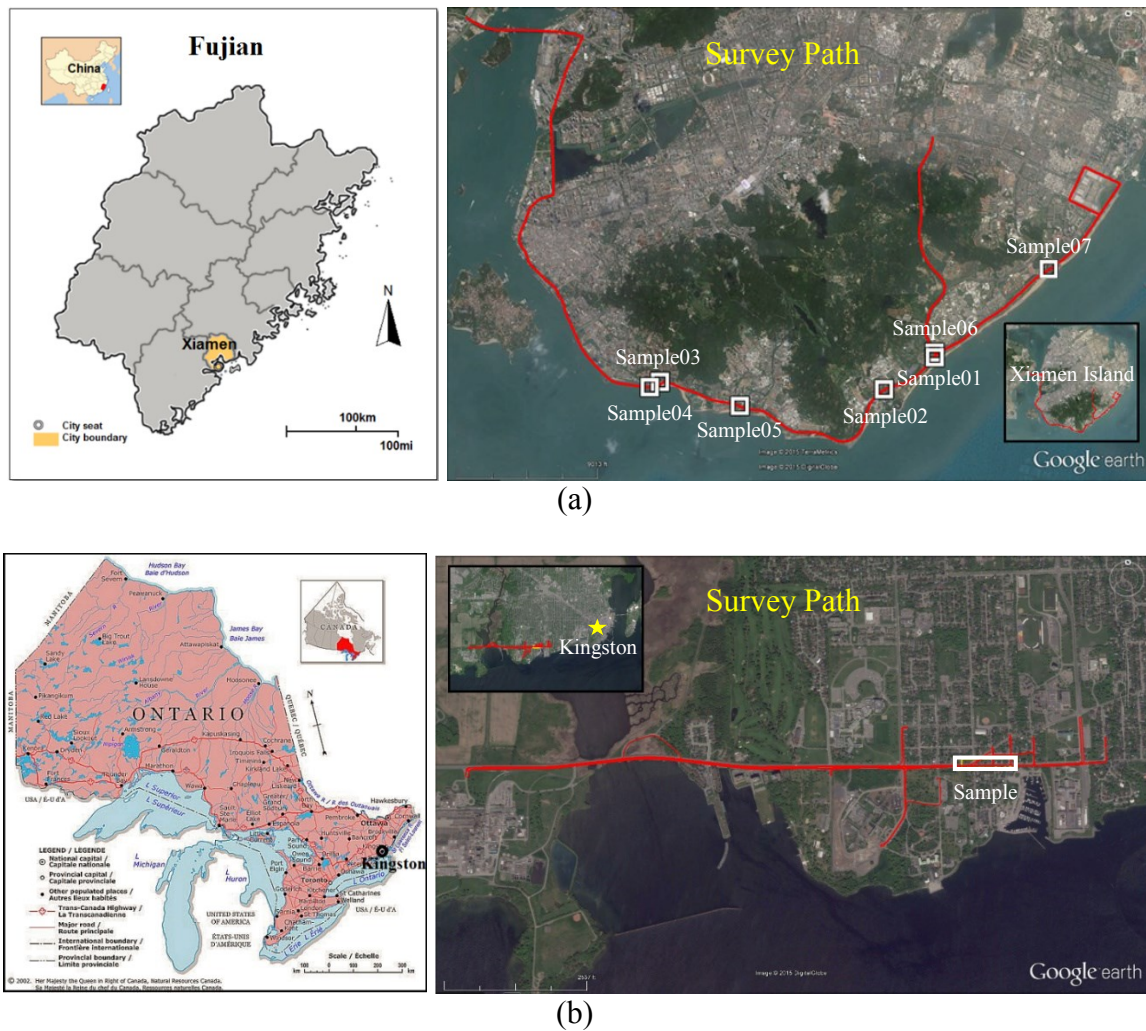


Figure 3.1: Study areas: (a) Island Ring Road in Xiamen, Fujian, China, and (b) King Street in Kingston, Ontario, Canada.

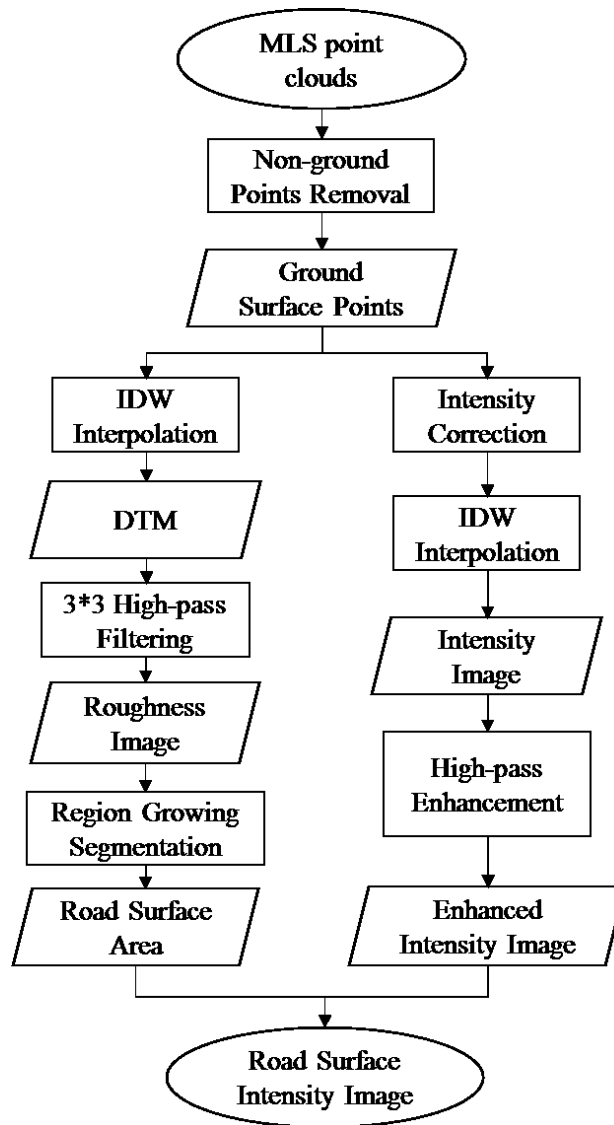
The average point density of Xiamen datasets and Kingston datasets are 7,000 points/m<sup>2</sup> and 4,800 points/m<sup>2</sup>, respectively. The two datasets were then converted into the format of LAS that is a standard in the laser scanning industry. The LAS format contains binary data consisting of a Header Block, Variable Length Records, and Point Data. The Header Block consists of a public block including point numbers and coordinate bounds. The Variable Length Records contain projection information, metadata and user application data. The Point Data records the X, Y, and Z 3D coordinates, intensity, returns, scan direction flag, scan angle rank and other attribute information (ASPRS Standards Committee, 2011). The data record in a LAS file is illustrated in Table 3.1, and the coordinate, intensity value and scan angle rank were adopted within this research.

Table 3.1: Point Data Record (Source: ASPRS Standards Committee, 2011)

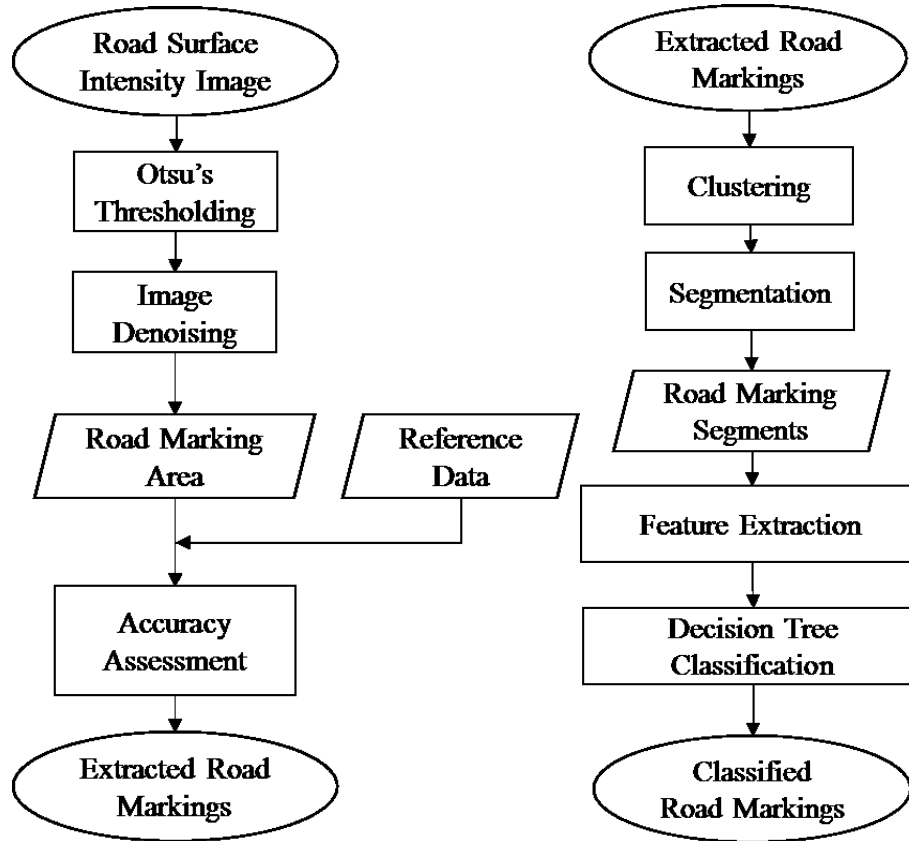
Item	Description
X	Coordinate
Y	Coordinate
Z	Coordinate
Intensity	The intensity value is the integer representation of the pulse return magnitude.
Return Number	The Return Number is the pulse return number for a given output pulse.
Number of Returns (given pulse)	The Number of Returns is the total number of returns for a given pulse.
Scan Direction Flag	The Scan Direction Flag denotes the direction at which the scanner mirror was traveling at the time of the output pulse.
Edge of Flight Line	The Edge of Flight Line data bit has a value of 1 only when the point is at the end of a scan.
Scan Angle Rank (-90 ° to +90 °) – Left side	The Scan Angle Rank is a signed one-byte number with 1° of accuracy from +90 ° to -90 °. The scan angle is an angle based on 0 ° being nadir, and -90 ° to the left side of the aircraft in the direction of flight.
GPS Time	The GPS Time is the double floating point time tag value at which the point was acquired.

### 3.2 Description of the Proposed Workflow

The proposed method within this study consists of three phases, including preprocessing (see Figure 3.2 (a)), road marking extraction (see Figure 3.2(b)) and road marking classification (see Figure 3.2(c)).



(a) Preprocessing



(b) Road Marking Extraction

(c) Road Marking Classification

Figure 3.2: Workflow of road marking extraction and classification: (a) Workflow of Preprocessing, (b) Workflow of Road Marking Extraction, (c) Workflow of Road Marking Classification.

(1) Preprocessing: the raw point clouds are preprocessed in two steps to reduce the volume of the data and overcome the problem resulting from the uneven distribution of intensity data.

The first step is the road surface detection. The non-ground removal is implemented to extract ground points from the MLS data. The ground surface points are rasterized into a digital terrain model (DTM) by inverse distance weighted (IDW) interpolation. In the DTM method, the road surface is distinguished from other features by its smoothness and connectedness. The smoothness of DTM is the absolute value calculated by a  $3 \times 3$  high-pass filter.

The second step is the intensity correction and enhancement. The intensity value of the ground surface points are corrected by the scan angle rank, following by the IDW interpolation. After scan-angle-rank-based intensity correction and rasterization, the corrected intensity image is further enhanced by the large size high-pass filtering process.

(3) Road marking extraction: with the application of Otsu's thresholding method, the corrected and enhanced intensity image is used to extract road markings followed by denoising process.

(4) Road marking classification: the extracted road markings are clustered by a region growing segmentation. The road marking clusters are then segmented into road marking segments by the neighbour counting filtering process. Eventually, the road marking segments are classified based on the geometry features using a manually built decision tree.

### **3.3 Preprocessing of MLS Data**

#### **3.3.1 Road Surface Extraction**

The raw MLS data includes various non-ground points, such as the pedestrians, vehicles, trees, poles, and buildings. In order to eliminate the disturbance from non-road points and improve the computational efficiency of road marking extraction, these non-road points are removed prior to the extraction. A hybrid road surface extraction is introduced in this step, including a voxel-based upward growing, DTM interpolation, high-pass filtering and region growing segmentation.

##### **3.3.1.1 Non-ground Points Removal**

A voxel-based upward growing method is employed to segment the raw MLS data into ground points and non-ground points. This method partitions point cloud data into an

octree structure with a voxel size (see Figure 3.3(a)). For each voxel, it expands to its 9-neighbour upward voxels (see Figure 3.3(b)), and then the growing scheme expands until it reaches the top boundary. If the elevation of the top voxel is smaller than the predefined threshold, the cluster of these voxels is referred to the ground. The point clouds in these voxels are labeled as ground points. Otherwise, the point clouds will be categorized as non-ground points.

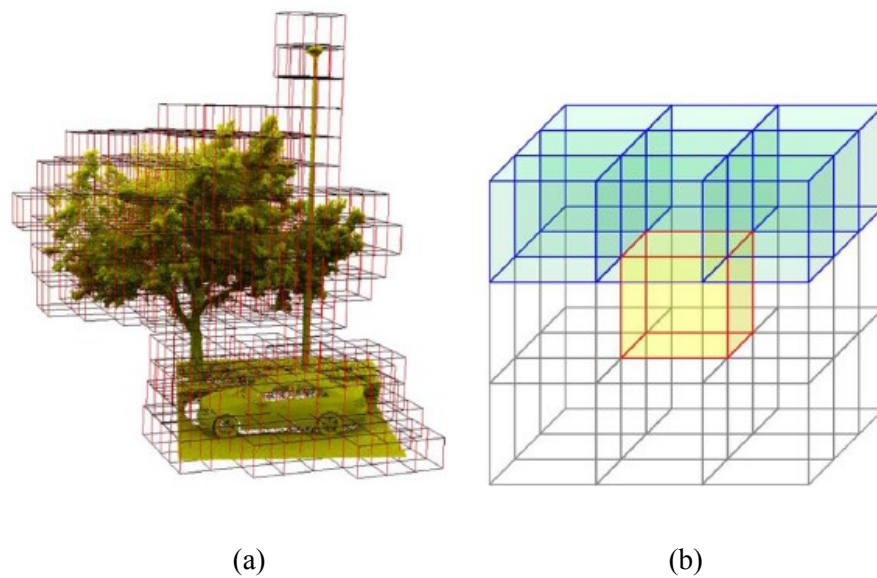


Figure 3.3: Octree structure and upward 9-neighbours voxel: (a) Octree partition structure, and (b) upward growing scheme (Source: Yu et al., 2015)

### 3.3.1.2 IDW Interpolation of DTM

In the removal process, all the non-ground points (e.g. pedestrians, vehicles, trees, shafts and buildings) are removed from raw point clouds. The volume of the ground points concentrates 60% of the raw MLS data. To further reduce the data volume and improve the computational efficiency, the ground points will be rasterized into the DTM by IDW interpolation. With the IDW interpolation, the grey value of a grid is interpolated with its neighbours. The grey value of a grid is calculated given the formula below:

$$z(x) = \frac{\sum_{k=1}^n w_k z_k}{\sum_{k=1}^n w_k} \quad (3.1)$$

$$w_k = 1/d_k^2$$

where  $w_k$  is the weight of the  $k$ -th point within the grid, as the function of distance  $d_k$ ;  $z_k$  is the  $k$ -th point grey value that can either be an  $z$  value or intensity value;  $n$  is the number of points in a grid. When  $z_k$  represents the elevation of the point, the result of the IDW interpolation is the DTM; when  $z_k$  represents the intensity of the point, the result is intensity image of the ground.

### 3.3.1.3 High-pass Filtering

The main features of the road surface are characterised by its smoothness and connectedness. In general, the surface of the grass is rougher than the road surface. Additionally, it is clear that the existence of a curb would result in a sudden change in the height on the road boundary. Therefore, a high-pass filter is applied to the DTM. The absolute value of filtering result indicates the roughness of the surface. A  $3 \times 3$  and  $5 \times 5$  high-pass kernels are shown in Figure 3.4.

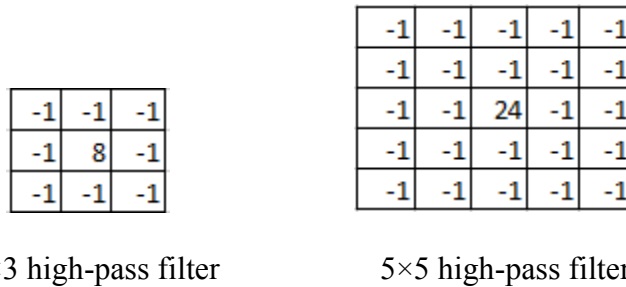


Figure 3.4: Illustrations of the high-pass filters.

The high-pass filter compares the centre grid with the average value of its neighbourhood and assigns the difference as the grid value. The grids with high absolute values indicate that there is a sharp elevation change at the location, i.e. the roughness of



the surface. To distinguish the road surface from other grounds (e.g. lawn and curbs), a threshold should be defined based on the absolute value of the filter results.

#### **3.3.1.4 Region Growing Segmentation**

In order to improve the computational efficiency, the points of the road surface were rasterized into a 2D intensity image using the IDW interpolation method. Although the elevation information was lost after the dimensionality reduction, the intensity information was retained in the 2D image, which was essential for the road marking extraction.

One of the critical parameters in intensity image generation is the spatial resolution (pixel size) of grid to store the result of IDW interpolation. It determine the accuracy of the intensity image and the computational efficiency of road marking extraction. The larger grid size leads to lower spatial resolution, smaller data volume and non-distinct details. The fine grid interpolation captures the details of pavement markings and increases the computational work. To improve the computational efficiency of extraction and provide accurate and detailed road markings for further classification, the analysis of grid size of IDW interpolation will be undertaken in Section 4.1.2.

#### **3.3.2 Intensity Image Generation**

In order to improve the computational efficiency, the points of the road surface were rasterized into a 2D intensity image using the IDW interpolation method. Although the elevation information was lost after the dimensionality reduction, the intensity information was retained in the 2D image, which was essential for the road marking extraction.

One of the critical parameters in intensity image generation is the spatial resolution (pixel size) of grid to store the result of IDW interpolation. It determine the accuracy of the intensity image and the computational efficiency of road marking extraction. The larger grid size leads to lower spatial resolution, smaller data volume and non-distinct details. The fine grid interpolation captures the details of pavement markings and increases the computational work. To improve the computational efficiency of extraction and provide accurate and detailed road markings for further classification, the analysis of grid size of IDW interpolation will be undertaken in Section 4.1.2.

### **3.3.3 Scan Angle Based Intensity Correction**

The unevenly distributed intensity leads to the large in-class variance of road marking points, which affects the extraction of the road markings. A variety of methods were developed to overcome the distribution issue of MLS data. For example, the MLS dataset can be partitioned into subsets, such as segments or profiles, to reduce the in-class variance and improve the extraction performance.

In this study, a scan angle based intensity correction was adopted to reduce the variance of intensity directly. The first step of the correction was to figure out the linear relationship between the cosine of the scan angle rank and the intensity of road markings. The scatterplot associated with the intensity image (see Figure 3.5) presents the relationship between pixel intensity and the rasterized cosine of scan angles. Figure 3.5(a) illustrates the scatter plots including all of the pixel intensities from Sample05. The clouds on the bottom and top of the image refer to the pavement pixels and the pavement marking pixels with high intensities, respectively.

Based on Equation (2.4) in Section 2.3, the measured intensity values have a positive correlation with cosines of incidence angles. According to mathematical deduction, the Equation 2.4 holds for pixel data interpolated by IDW. Thus, the linear regression model generated from the intensity image can be used to correct the intensity value of MLS data. Figure 3.5(b) demonstrates the scatter plots corresponding to the “purified” road marking pixels that were selected manually. After the removal of the outlier, the linear regression model was built using these pure road marking samples. The formula of the linear regression model is presented as below:

$$y = 15115 \cdot x + 24794 \quad (3.2)$$

In this regression model, the R-squared is 0.77, and the P-value is less than 0.0001. It indicates that the model can explain 77% variance of the road marking pixel intensity. The correlation between the cosine of scan angle and the intensity value is significant. With this linear regression model, the road marking intensity can be corrected by the cosine of the scan angle rank; and majority of the in-class variance of the road marking intensity will be eliminated.

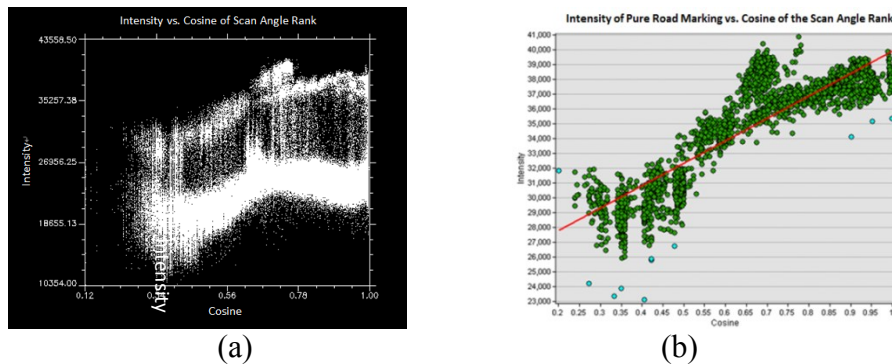


Figure 3.5: Intensity of the Sample05 and its associated plot: (a) the plot of the cosine of the scan angle rank vs. intensity and (b) Scatterplot of pure road marking pixels. Green points are the inlier and the cyan points are the outlier. The red line is the trend of the linear regression.

### 3.3.4 Large-size High-pass Enhancement

Aiming to eliminate the uneven distribution of the intensity the scan-angle-rank-based correction is implemented to the road surface points prior to rasterization. After rasterization of the corrected intensity image, the large-size high-pass enhancement will be utilized on the corrected intensity image to eliminate the spatial varieties of intensity caused by various surface roughness.

The principle of the filter is to distinguish the road marking pixels from pavement pixels in a window-based process, such as the  $3 \times 3$  kernel. In this window, the centre pixel is the target, and it is compared to its neighbouring pixels one by one. Based on the differences from its neighbours, the pixel will be classified into the road marking or the pavement.

The designed kernels of the filters are same as ideal high-pass filters (see Figure 3.4). Compared with other high-pass filters, each neighbour pixel has the same weight in an ideal high-pass convolution. Additionally, the comparisons between target pixel and its neighbour pixels are equitable. The convolution of the ideal high-pass filter can be interpreted by the mathematical expressions below:

$$h = n \times a + \sum_{i=1}^n (-1) \times b_i \quad (3.3)$$

$$h = \sum_{i=1}^n (a - b_i) \quad (3.4)$$

where  $h$  is the convolution result;  $a$  denotes the value of target pixel;  $b_i$  denotes neighbour pixel of the target pixel;  $(a - b_i)$  indicates the difference between the target

pixel and one of its neighbour pixel. It is assumed that there are only two classes (e.g. road marking and pavement) in the image, and the pixels in the same class have the same value while the road markings have a higher intensity value than road pavements. If the target pixel and the neighbour pixel are both in the same class,  $(a - b_i)$  is close to 0. If the target pixel is the road marking and the neighbour pixel is the pavement,  $(a - b_i)$  will be larger than 0. If the target pixel is the road pavement and the neighbour pixel is the road marking,  $(a - b_i)$  will be less than 0. Therefore,  $h$  summarizes the differences between the target and its neighbours. Assuming no in-class variance exists in road markings and pavement, the convolution result  $h > 0$  indicates the target pixel is the road markings and  $h < 0$  indicates the target pixel is the road pavement. However, there is an in-class variance in each class. The threshold cannot be simply set to 0 for extracting road markings from convolution result. Therefore, Otsu's thresholding method needs to be applied to determine the optimal threshold for the extracting from the convolution result. Based on the interpretation of the convolution, the ideal high-pass filter is used to distinguish the road markings from the pavements.

The application of the ideal high-pass filter is able to solve the unevenly distributed intensity problem. (1) It helps the targets to be distinguished from the background. When the window size is smaller than the object, only the edges between the objects and the background will be highlighted. If the window size is significantly larger than the target, the target will be outstanding from the background; (2) the relatively small window size makes the ideal high-pass process free from the impact of unevenly distributed intensity. Although the intensities distribute unevenly in the whole image, the variance of road markings in a small window is relatively limited. Therefore, the ideal high-pass filter has

the great potential to distinguish the road markings from the pavements and solve the unevenly distributed intensity problem.

Based on the characteristics of the ideal high-pass filter, the kernel has to meet the requirements as follows. Firstly, the kernel size must be large enough to contain both road marking pixels and pavement pixels. Secondly, the kernel size should be small enough to avoid the impact of the spatial variance of the intensity.

Sample02 is selected to verify the minimum kernel size of the high-pass filter, because it has the longest and widest road marking. Sample06 is selected to reveal the maximum value, as it has a segment of three-road that contains more spatial varieties.

The no-data areas are defined as no-data pixels, which may interrupt the high-pass filtering. Therefore, before the filtering, the no-data areas are assigned a value, which is between the pavement pixel value and the road marking pixel value. The alternative value of the no-data pixel can be defined by an average filter. A value that is three times of the average of neighbouring values is assigned to the no-data pixel. This method of a self-adaptive compensation can be utilized to all the samples.

The performance of the high-pass enhancement will be evaluated in Chapter 4, and the best size of the filter will be provided after the assessment.

### **3.4 Extraction of Road Marking**

#### **3.4.1 Otsu's Thresholding**

The Otsu's thresholding method is applied to extract road markings based on the discriminant analysis. It segments the image automatically with the optimum threshold that helps minimize the within-class variance. It is assumed that the image is bimodal and

the illumination is uniform, therefore the bimodal brightness can be determined based on the differences of the materials' properties.

The road surface area is preserved in the intensity images in the format of either the asphalt pavements or the road markings. With the assistance of the intensity correction and enhancement, the illumination in the image is uniform. Thus, the enhanced and corrected intensity image is able to meet the requirements of the Otsu's thresholding method, and then the global thresholding process can be employed to preprocess the intensity images.

### **3.4.2 Image Denoising**

There are three principal sources of the noise: the irregularity of the road surface, the boundary of different adjacent pavement and the absence of point data. The scan-angle-rank-based intensity correction is only capable to eliminate the intensity variance for a flat road surface. In the surveying of a poor-conditioned road, the laser beam may scan at the crack or the rutting slope. The relatively smaller incidence angle of the cracks and rutting would result in a brighter intensity compared to their neighbouring road surface and cause a false positive in the thresholding result. Another false positive could be resulted from the boundary of two different pavements, which is enhanced by the high-pass enhancement. Besides, the gaps generated from a low point density between the points may also cause a false negative.

Three de-noising methods, introduced by Adam and Bischof (1994), are employed in this research, including median filtering, neighbour-counting filtering and region growing segmentation. Small pixels of false-positive and false-negative can be eliminated utilizing the median filtering approach. The segments of false-positive with medium sizes (i.e.

small fragments of cracks, and manholes) can be removed using the region growing segmentation if they are smaller than the smallest road marking segment. However, the region growing method is not applicable for the large segments of false-positive, which occur at a depression or boundary between two different pavements. Figure 3.6(a) demonstrates the intensity image of a pedestrian crossing, where the intensity of the concrete pavement is brighter than asphalt pavement's. The concrete region is detected as markings (see Figure 3.6(b)). Figure 3.6(c) illustrates a  $15 \times 15$  kernel whose convolution is equal to the number of marking pixels in a  $15 \times 15$  window. Because concrete region has more homogeneous neighbouring pixels than pedestrian crossing, the concrete region can be detected during neighbor-counting filtering. After the neighbour-counting filtering (see Figure 3.6(d)), these large false positive regions are hollowed out and broken into small pieces that could be removed using the region growing algorithm. It should be noted that the neighbour-counting filtering is applied in the case study of Kingston to compress the noise caused by depression and different pavements.

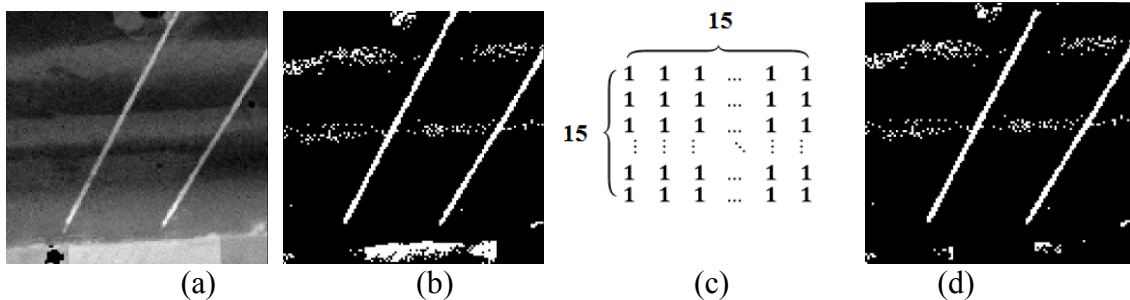


Figure 3.6: Neighbour-counting filtering: (a) corrected intensity image of road surface, (b) extracted result from enhanced intensity image, (c)  $15 \times 15$  kernel of neighbours counting, and (d) neighbour-based filtering result.

The last step in the road marking extraction is the de-noising process. Method and function of the road marking extraction approaches are summarized in Table 3.2.



Table 3.2: Summary of road marking extraction.

	Method	Function
Road surface detection	Voxel based upward growing algorithm	Removing non-ground points
	High-pass filtering	Removing non-road region
Intensity correction and enhancement	Scan-angle-rank-based intensity correction	Eliminating variance of intensity caused by different incidence angle
	Large size high-pass enhancement	Eliminating variance of intensity caused by different surface roughness
Thresholding	Otsu's thresholding	Extracting road markings
Denoising	Neighbours-based filtering	Breaking the false positive region caused by the boundary of pavements
	Region growing segmentation	Removing salt-noise and small fragments
	Median filtering	Filling the pepper-noise on the road markings

### 3.4.3 Accuracy Assessment

In order to evaluate the performance of the road marking extraction, an accuracy assessment will be implemented with manually labeled reference data.

Table 3.3 illustrates a confusion matrix for the binary classification, where  $tp$  and  $tn$  indicate a true positive and negative;  $fp$  and  $fn$  represent a false positive and negative, respectively. In this study, the road marking class is the target class (*positive*), and the rest class is the pavement class (*negative*).

Table 3.3: A confusion matrix for binary classification.

Classified Class \	as Positive	as Negative
Positive	$tp$	$fn$
Negative	$fp$	$tn$

The overall accuracy, as the most used empirical measure, is not enough to evaluate the performance of the extraction especially for this study where the proportion of target class is small in the study area.

$$\text{overall accuracy} = \frac{tp + tn}{tp + tn + fp + fn} \quad (3.5)$$

In the extraction, the accuracy of the road marking extraction is much more important than the accuracy of the pavement detection. Therefore, three commonly-accepted performance evaluation measures: *recall*, *precision*, and *F-Score*, are employed in the accuracy assessment (see formula 3.6 – 3.8) (Sokolova et al. 2006).

$$\text{precision} = \frac{tp}{tp + fp} \quad (3.6)$$

$$\text{recall} = \frac{tp}{tp + fn} \quad (3.7)$$

$$\text{F-Score} = \frac{(\beta^2 + 1) * \text{precision} * \text{recall}}{\beta^2 * \text{precision} + \text{recall}} \quad (3.8)$$

Precision is a function of the true positive and false positive, which indicates the correctness of road marking extraction. Recall represents the completeness of road marking extraction. The F-Score is evenly balanced or partial to precision, when  $\beta = 1$  or  $\beta > 1$ , respectively. In this study, the completeness is adopted, and the precision is replaced by the correctness. Both completeness and correctness make the same contribution to the F-Score ( $\beta = 1$ ) (see formula 3.9 – 3.11):

$$\text{correctness} = \frac{tp}{tp + fp} \quad (3.9)$$

$$\text{completeness} = \frac{tp}{tp + fn} \quad (3.10)$$

$$F - Score = \frac{2 * correctness * completeness}{correctness + completeness} \quad (3.11)$$

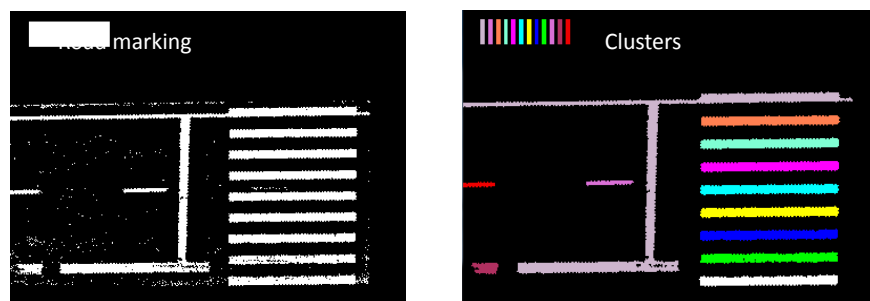
In order to validate the proposed extraction method, the evaluation results will be compared with the outputs from three recently published road marking extraction methods with MLS data. The comparison will be further discussed in Chapter 4.

### 3.5 Classification of Road Marking

In this research, the road marking recognition consists of three steps, including road marking isolation, feature extraction and road marking classification.

#### 3.5.1 Road Marking Segmentation

The first step of road marking classification is dividing the extracted road marking into segments, where a 4-neighbour region growing segmentation (Adams & Bischof, 1994) is employed. The region growing segmentation has the capacity of separating different clusters and ensures the connection of the pixels in each cluster. During region growing segmentation, regions that are smaller than the smallest road marking are removed from the road marking segments.



(a) Extracted road marking

(b) Region growing segmentation

Figure 3.7: Region growing segmentation: (a) extracted road marking, (b) region growing segmentation result.

Figure 3.7 shows an extracted road marking and the segmentation result, in which the

noise and little clusters are removed in the procedure of region growing. In addition, the road markings which are attached to each other could be merged into a large region (see Figure 3.7 (b)). This large road marking should be segmented into a few road markings to guarantee the subsequent recognition of transverse road marking and zebra crossing stripes. Taking the width and junction into consideration, the large road marking can be easily classified into two types: the thin road marking and the wide road marking.

The segmentation method consists of two steps: distinguishing thin and wide road markings, and splitting road markings at junctions. The neighbour-counting filtering is applied to detect the thin, wide road markings and their junctions.

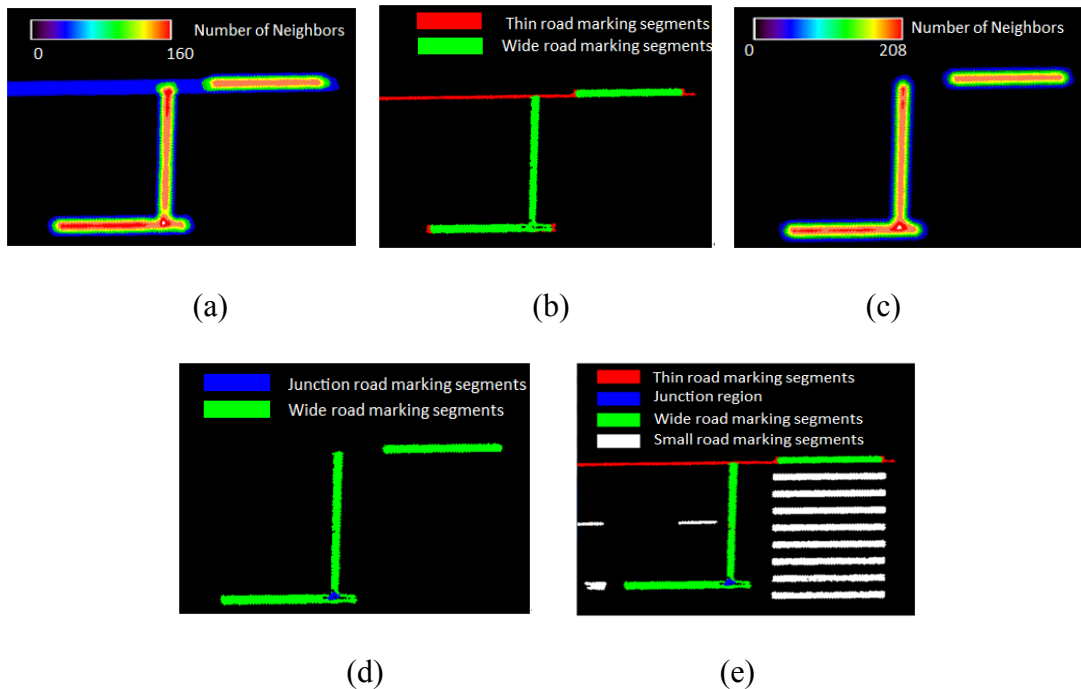


Figure 3.8: Segmentation of large road marking segments: (a) neighbour-counting image of large segments, (b) neighbour-counting image of wide road marking, (c) junction detection based on neighbour-counting, and (e) segmentation result of large road marking.

The width of road markings can be inferred by counting the neighbours of a pixel. As shown in Figure 3.8(a) in terms of the road marking pixels, the wide road marking pixels

have more neighbours while the thin markings have less. Therefore, wide markings and thin markings can be distinguished as illustrated in Figure 3.8(b). Figure 3.8(c) shows the neighbour-counting of wide markings. It can be observed that junction regions have more neighbours, thus junctions can be detected by the application of the neighbours based filtering. Figure 3.8(d) shows the detected junction region, and the wide road markings are separated at junctions. The final segmentation result is presented in Figure 3.8(e).





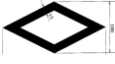
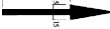

### 3.5.2 Feature Extraction of Road Marking

After the road marking is partitioned into segments, geometric parameters of marking segments will be calculated. To achieve the translation and rotation invariance of road marking shape and improve the computational efficiency of the feature, four parameters were employed in road marking classification, including area, perimeter, estimated width and orientation. Area and perimeter, as the basic geometric parameters of a road marking, can be directly calculated. The estimated width is the function of the width of a segment from area and perimeter:

$$width = \frac{2 * area}{perimeter} \quad (3.12)$$

Although this estimated value is not the true width of the segment, it can indicate the thinness of road markings. Table 3.4 shows the area, perimeter, real width, real length and the estimated width of each kind of road markings. The estimated width is fairly accurate when the length is much longer than the width. As shown in Figure 3.9, road marking of some classes can be distinguished from others according to area (see Figure 3.9(a)) and width (see Figure 3.9(b)).

Table 3.4: Road marking geometric measures

Road markings	Zebra Crossing	Continuous line	Broken line 1	Broken line 2	Diamond	Arrow (Straight)	Word
Shape							
Width (cm)	45	15	45	15	15	15	20
Length(cm)	600	8000	100	200	Null	300	Null
Area (cm <sup>2</sup> )	27000	120000	4500	3000	6772.74	5400	13080
Perimeter(cm)	1290	16030	290	430	903	649	1221
Estimated width (cm)	42	10	31	14	15	17	21
Error (cm)	3	0	14	1	1	2	1

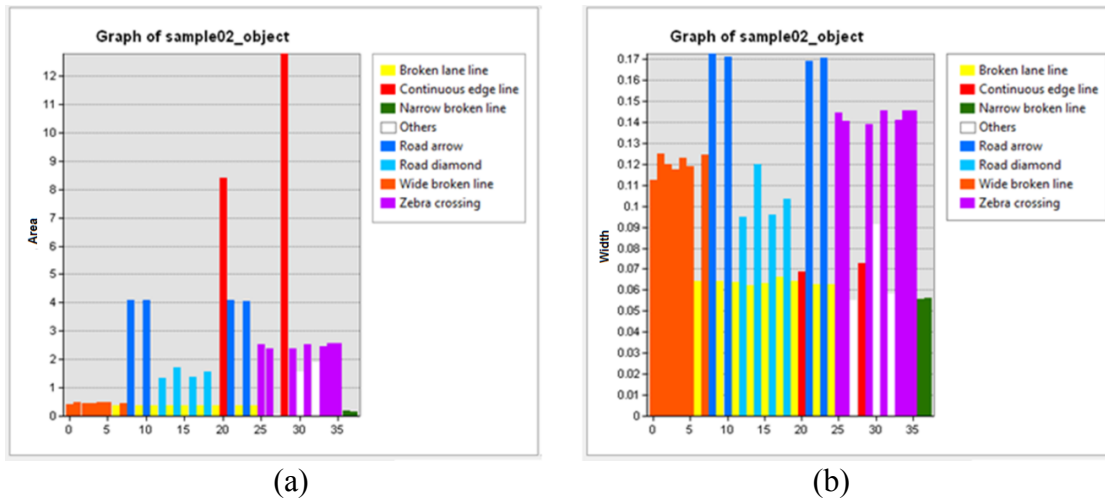


Figure 3.9: Road marking shape feature: area and width: (a) area of labeled road markings, and (b) estimated width of labeled road markings.

Based on area and width of the road marking, rectangular markings can be detected and recognized, but irregular markings having similar area and width, i.e. road diamonds, may be misclassified. In this case, a Minimum Bounding Rectangle (MBR) is derived to present the extent of each road marking (see Figure 3.10). According to the width of MBRs, road markings can be classified into the road marking in thin MBRs (e.g. zebra strip and broken line) and road marking in wide MBRs (arrow, diamond, character and number).

Based on the MBRs, the main angle of a road marking can be calculated. Compared

with longitudinal markings, transverse markings have a higher variance of the main angle in a section of the road. It makes transverse markings distinguishable from longitudinal markings.

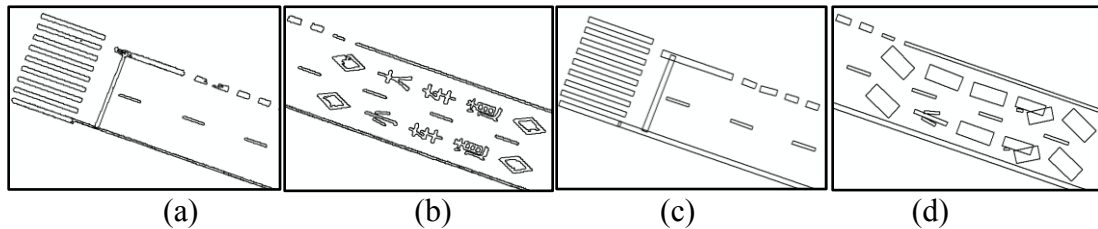


Figure 3.10: Road marking boundaries and minimum bounding rectangles: (a) and (b) show the boundaries of the road marking segments, (c) and (d) show the bounding rectangles of the road marking segments.

Compared to other shape descriptors, the use of the parameters (i.e. area, perimeter and estimated width) has two advantages for road marking classification. Compared to shape descriptor and template matching, these three basic shape features require relatively low computational work. They can be calculated rapidly than other advanced shape descriptors, such as moment, chain code, profiles, Fourier descriptor and wavelet transform. It is noted that the orientation of the road markings is non-uniform and varying therefore, the template matching needs to be adapted to allow multi-angle matching that is based on the cost of computational power. Assuming that each of the road marking has different instances in eight directions in the study areas, accordingly eight templates need to be developed for multi-angle matching. This increases the amount of computation. Another factor that would increase the computation complexity of template matching is the template size. In the classification process, the size of road markings ranges from 1 m to 6 m. The increased size of the road markings requires larger templates in the matching process, which complicates the computational work. In addition, these three parameters (i.e. area, perimeter and estimated width) can be easily used to represent the shape of the

road markings. Each road marking has its own characteristics such as area, perimeter and width. Thus, in this study, these three basic shape parameters are used to describe the shape of road markings for further recognition. The MBR and its orientation are then employed to make the different road markings more distinguishable and recognizable from others.

### **3.5.3 Decision-tree Based Hierarchical Classification**

Based on strong prior knowledge of the road marking criteria, road-marking segments can be grouped into classes based on their geometric parameters (i.e. areas, estimated width, MBR area and MBR width). A decision tree is designed and developed for the classification. The hierarchical tree of road marking categories that developed in this study is illustrated in Figure 3.11. According to the People's Republic of China National Standards: Road Traffic Marking (2009), the road markings in Xiamen dataset can be classified into two categories: longitudinal and transverse marking. The orientation of road marking segments can be measured by the main angle of MBRs. Transverse and longitudinal markings have a high and low variance of the main angle in a section of the road respectively. The difference of orientation variance is adopted as the rule for the first level of the decision tree. Transverse markings of the Xiamen dataset include stop lines and transverse reduction lines. At the second level, longitudinal marking segments are separated into two groups based on the MBR width. In the third level, if the width of the segment exceeds 45 cm, it is referred to a wide MBR (i.e. road arrow or non-road arrow); otherwise, it is referred to a thin MBR (i.e. strip of zebra crossing, broken line or continuous line). In the fourth level, zebra crossings, broken lines, continuous lines, road arrows and non-road arrows are further classified into specific subclasses based on their



area and estimated width.

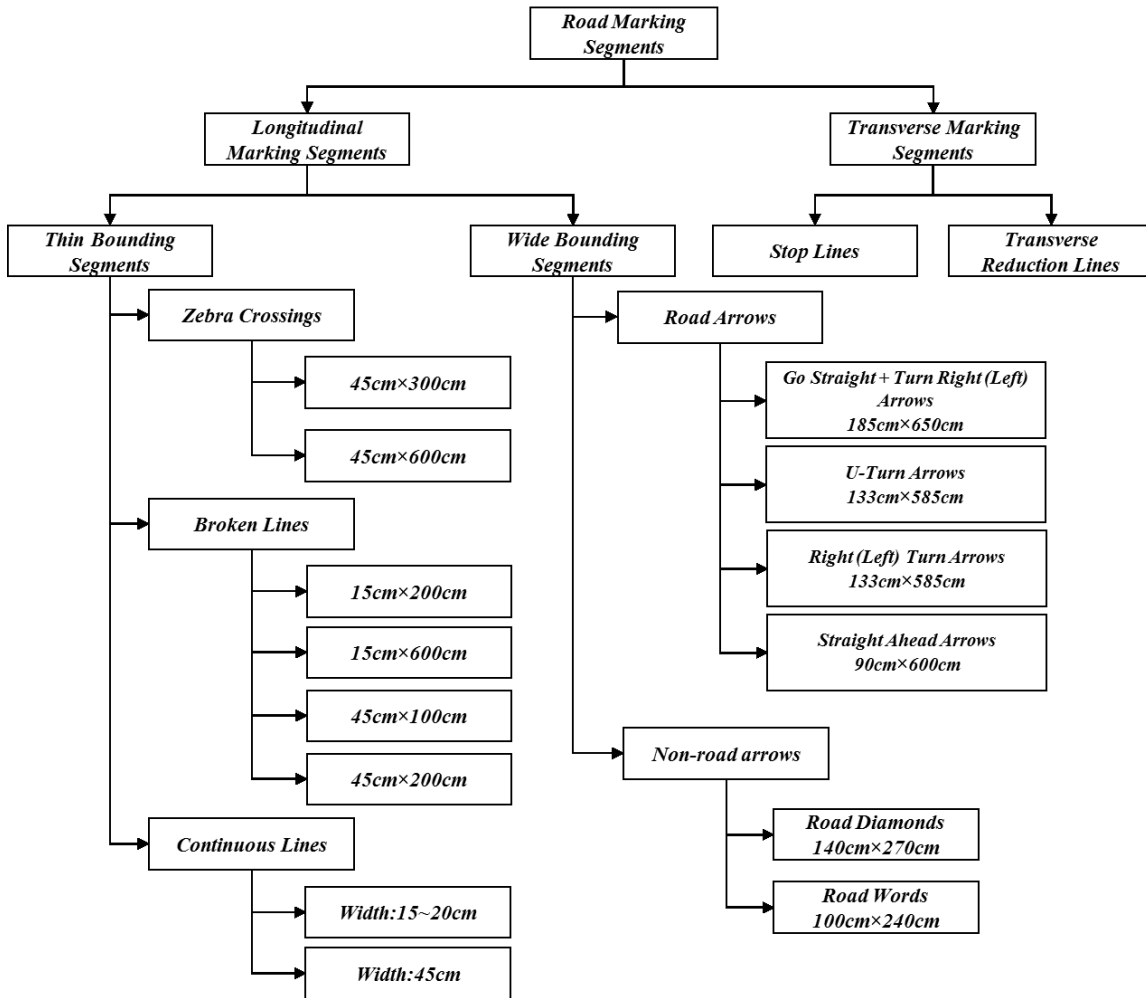


Figure 3.11: A hierarchical tree of the road marking categories.

The classification result is illustrated in Figure 3.12. At the first level, the marking segments are categorized into transverse markings (red) and longitudinal markings (white) (see Figure 3.12(a)). At the second level, the longitudinal markings are divided into thin MBRs (white) and wide MBRs (red) (see Figure 3.12(b)). Figure 3.12(c) shows the subclasses of thin MBRs, including zebra crossings (purple), broken lines (green) and continuous lines (yellow). At the fourth level, the categories of the road markings are sub-classified into the specific types (e.g. 15cm x 200cm broken line and 45cm x 100cm

broken line).

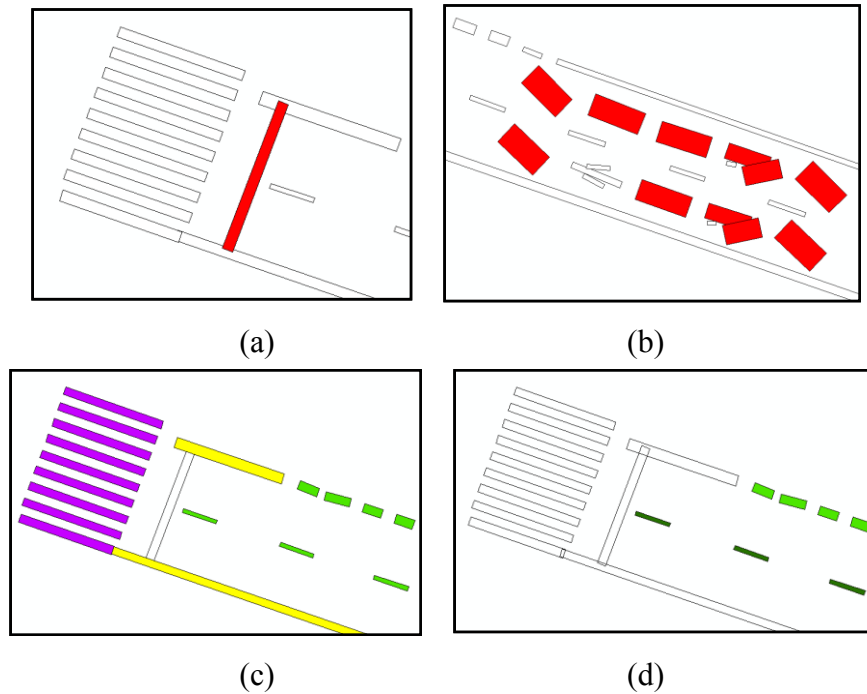


Figure 3.12: Decision tree classification: (a) the first level result, (b) the second level result, (c) the third level result, (d) the fourth level result.

### 3.6 Chapter Summary

This chapter introduces a road marking extraction and classification workflow. A preprocessing stage is proposed, focusing on the detection of the road surface and reduction of in-class variance of the road markings and the pavements. A high-pass filter with a window size of  $3 \times 3$  is applied on the digital terrain model (raster). The absolute values of the filtered result are then binarized to extract road surface from the ground surface. In addition, a scan-angle-rank-based intensity correction and a large window high-pass filter are implemented to decrease the in-class variance of the road markings and increase the difference between the road markings and the pavements. The Otsu's thresholding is then employed to partition the corrected and enhanced intensity images.

Based on a manually labeled reference dataset, the performance of road marking extraction method is evaluated with three measures (i.e. correctness, completeness and F-Score). The third section introduced road markings' geometric parameters and developed a tree-based hierarchical classification for road markings recognition.

## **Chapter 4 Results and Discussion**

The chapter begins with the results and discussions of road surface detection and scan-angle-rank-based intensity correction. To explore an appropriate size for the large-kernel-sized high-pass enhancement, the high-pass enhancement processes are demonstrated and evaluated by an accurate assessment. The following section presents the road-marking segmentation process. Finally, two datasets were selected to demonstrate the application of the research reported in the thesis. Results from both case studies are reported and analysed, in order to draw some conclusions regarding the validity of the extraction methods reported in this study.

### **4.1 Preprocessing of MLS Data**

Preprocessing aims to compress the large-sized data and balance the uneven distribution of intensity data prior to the extraction of the road markings. Section 4.1 demonstrates how to eliminate the intensity variance and evaluate the performance of proposed preprocessing methods. In addition, all pixel values are normalized between 0 to 255 to make the results comparable in each step.

#### **4.1.1 Road Surface Extraction**

##### **4.1.1.1 Non-ground Removal**

In this study, voxel-based upward growing aims to remove the non-ground points (e.g. pedestrians, vehicles, trees, poles and buildings) from the MLS dataset. Figure 4.1 presents the raw MLS data of Sample07 and its ground surface points with intensity value.

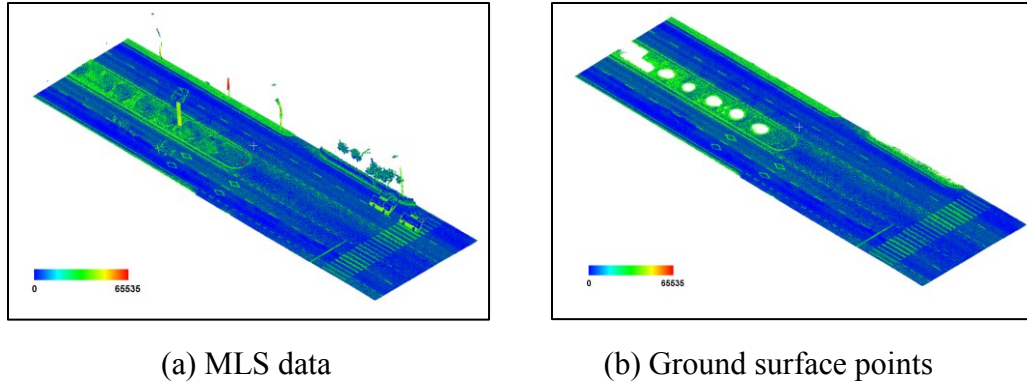


Figure 4.1: MLS data of Sample07: (a) MLS data, (b) ground surface points.

#### 4.1.1.2 Road Surface Region Extraction

The road surface region was extracted by the integration of IDW interpolation, high-pass filtering, thresholding and region growing segmentation. Figure 4.2(a) provides a view of DTM created from ground surface points, where the black area representing no-data area. The grid size of the DTM is set to 5 cm that corresponds with the size of the resolution intensity image. The large grey area refers to the road surface and the brighter regions represent the median strips.

The  $3 \times 3$  high-pass result of DTM and the absolute value of the high-pass value are shown in Figure 4.2(b) and Figure 4.2(c), respectively. It is noted that in the high-pass result, the absolute values of the road surface are much lower than the values of the other surfaces'. With a defined threshold (0.04 in this image), the objects (e.g. grass and curbs) can be distinguished from the ground. Other surface types with less roughness remain in Figure 4.2(d). Due to its character of continuous connectivity, the road surface is obtained as the largest smooth region that is shown in white (see Figure 4.2(e)).

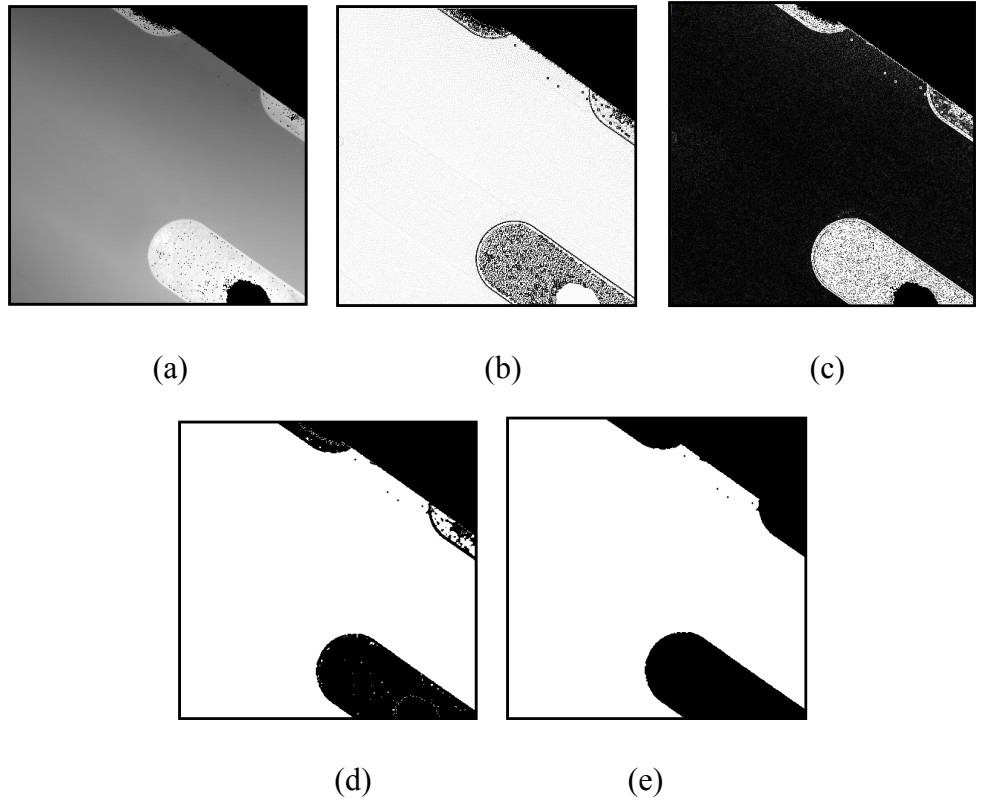


Figure 4.2: Sub-sample of the ground surface: (a) DTM (5 cm grid size), (b) 3×3 High-pass Filtering, (c) Absolute Value of High-pass Filtering, (d) Thresholding Result, and (e) Region Growing Result.

**4.1.2 Intensity Image Generation**

The IDW interpolation was applied to the ground surface points derived from MLS data at different levels (from 1 cm to 10 cm). However, the fine resolution can result in the increase volume of data and workload for computation (see Table 4.1).

Table 4.1: Resolution of intensity image and image size (Sample02).

Resolution (cm)	1	2	3	4	5	6	7	8	9	10
Image size (M)	98.6	24.6	10.9	6.18	3.96	2.75	2.01	1.54	1.22	0.99

From the grid size of 2.5 cm to 10 cm, the images of the road markings were blurred and the computational work was decreased (see Figure 4.3). With the grid size of 5 cm, the thinnest road marking (line width 15 cm) can be presented in the intensity image, and the gaps between the MLS points will be interpolated. Therefore, the road surface points were rasterized by IDW with the grid size of 5 cm.

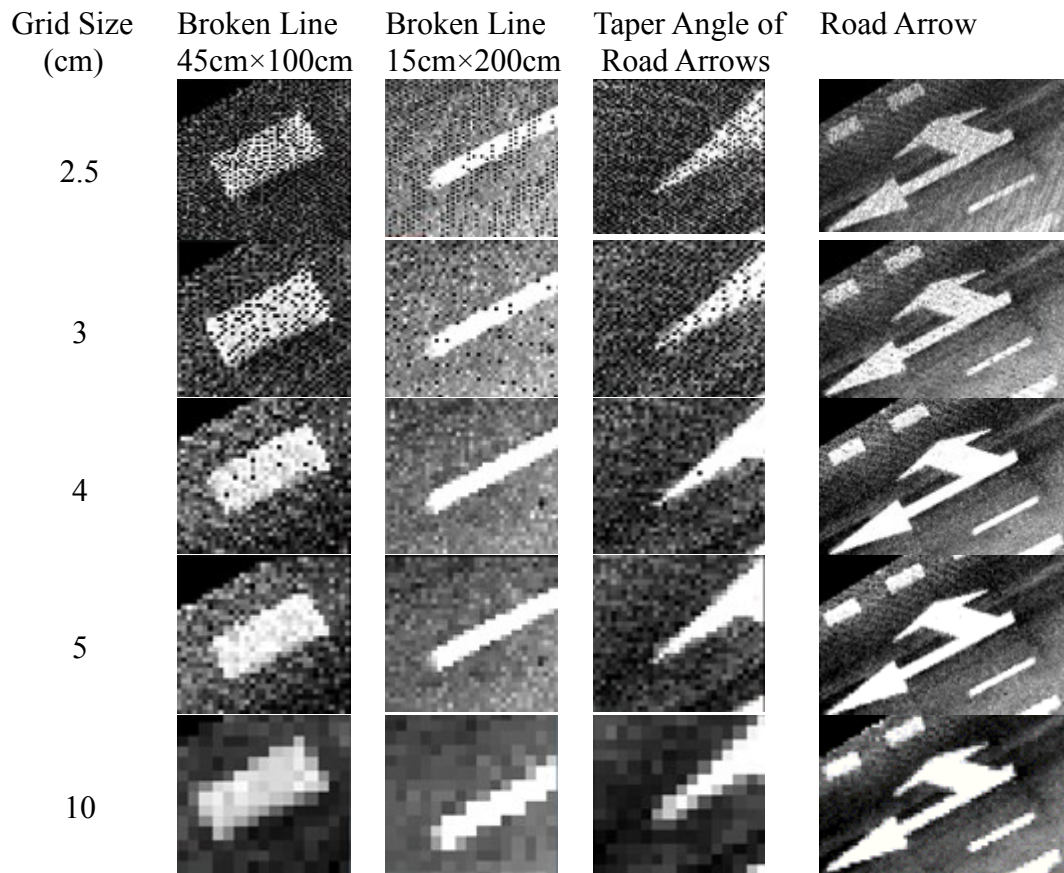


Figure 4.3: Intensity image generated at different resolutions.

Figure 4.4 shows the intensity image generated by the IDW interpolation with a grid size of 5 cm. In addition, the distinct details of the road markings are presented with an image resolution of 5 cm. In respect of intensity, the road markings look brighter than the pavements (asphalt). Nevertheless, the intensity of the pavement and the road markings are both unevenly distributed, which leads to large in-class variance and contaminated

extraction results.

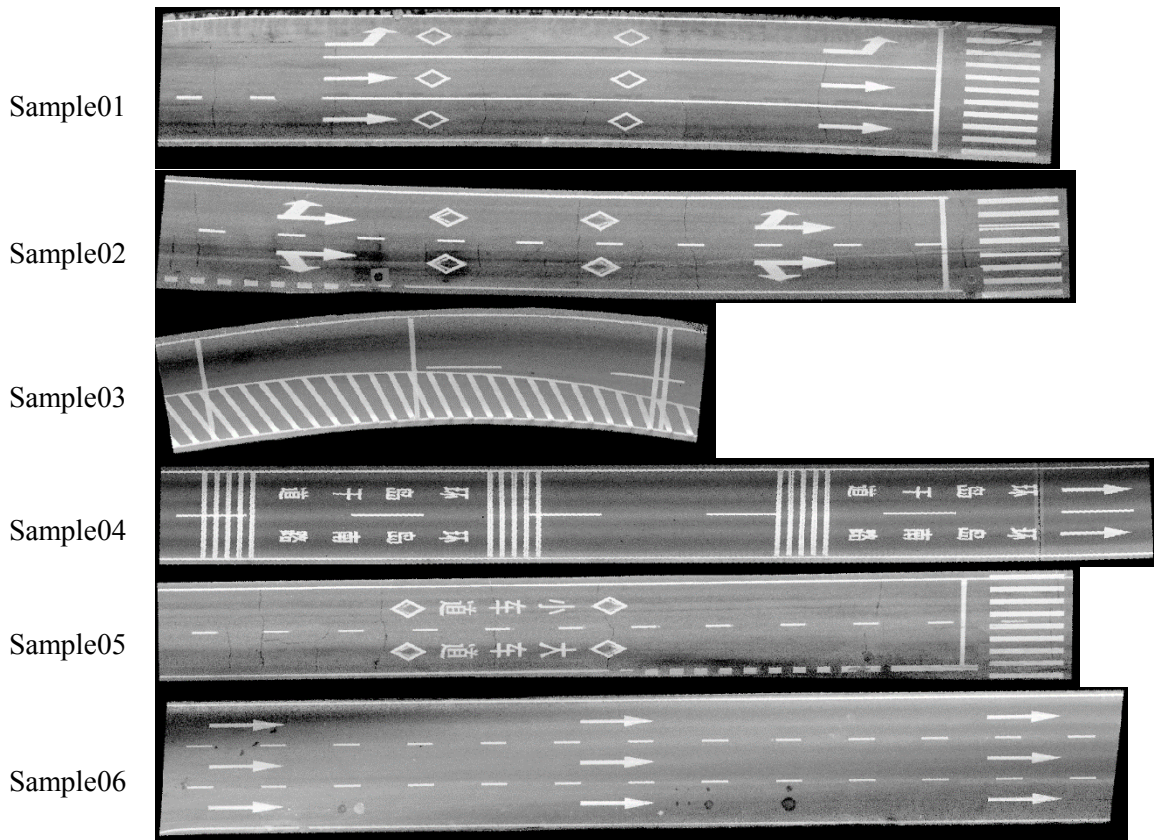


Figure 4.4: IDW interpolation results of point intensity: with the grid size of 5cm from Sample01 to Sample06.

### 4.1.3 Intensity Image Correction

In order to extract the road marking, a scan-angle-rank-based intensity correction was used to correct various intensity values caused by different incidence angles. The corrected intensity images are presented in Figure 4.5. It is evident that the contrast between road markings and the pavements was enhanced, therefore the road markings became more detectable. However, the variance of pavement intensity remained after the correction. The intensity value of the rough pavements on the road boundaries is too high to be distinguished from the road markings within the global thresholding method and



cannot be distinguished from road markings by global thresholding. Therefore, a local scale filtering approach was undertaken to eliminate the spatial variance caused by different pavement roughness prior to the road marking extraction process.

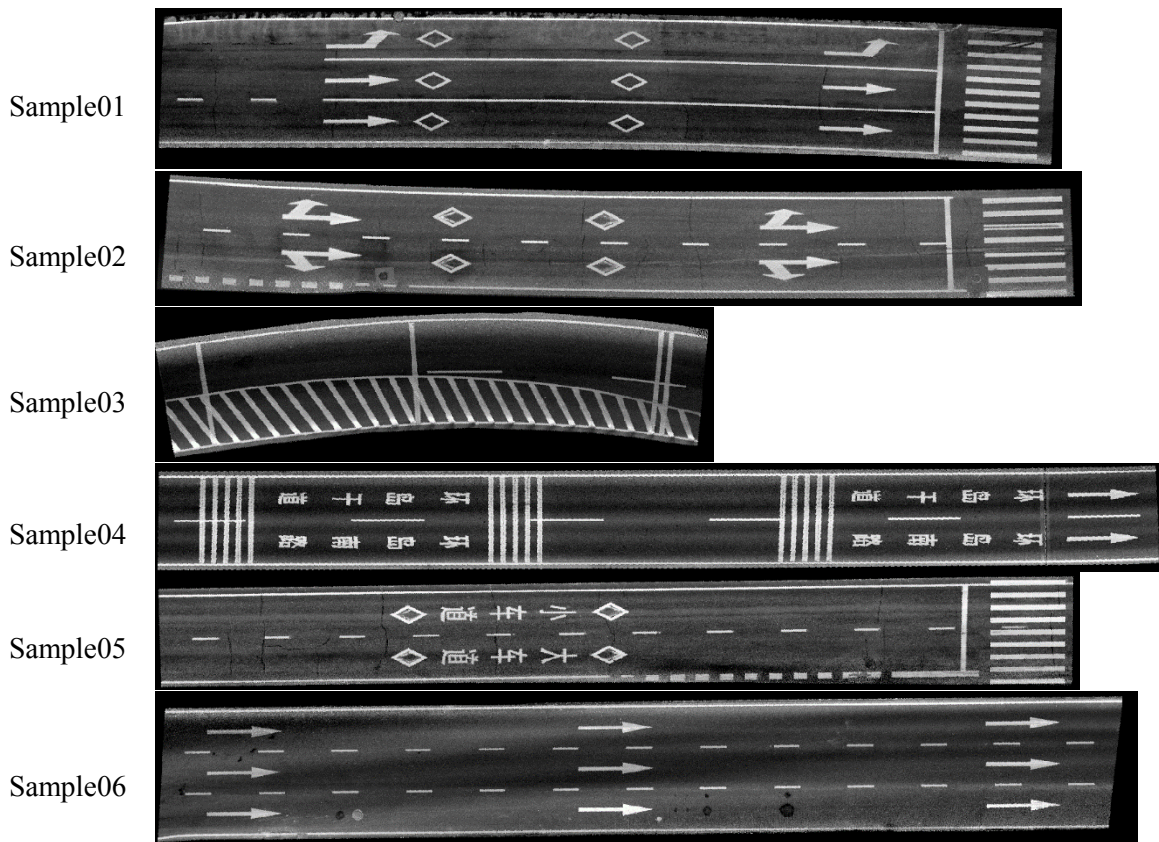


Figure 4.5: Corrected Intensity Image from Sample01 to Sample06.

In theory, the application of the intensity correction will decrease the in-class variance and increase the between-class variance. The improvement of the intensity image was demonstrated in the histograms of Sample02 (see Figure 4.6). It is clear that the distribution of the pavements and the road marking intensity value are more concentrated using the intensity correction process. The in-class variance of pavements and road markings decrease from 21.23 to 14.10 and 32.38 to 18.57, respectively. The difference between the road markings and the pavements also decreases from 91.10 to 78.42.

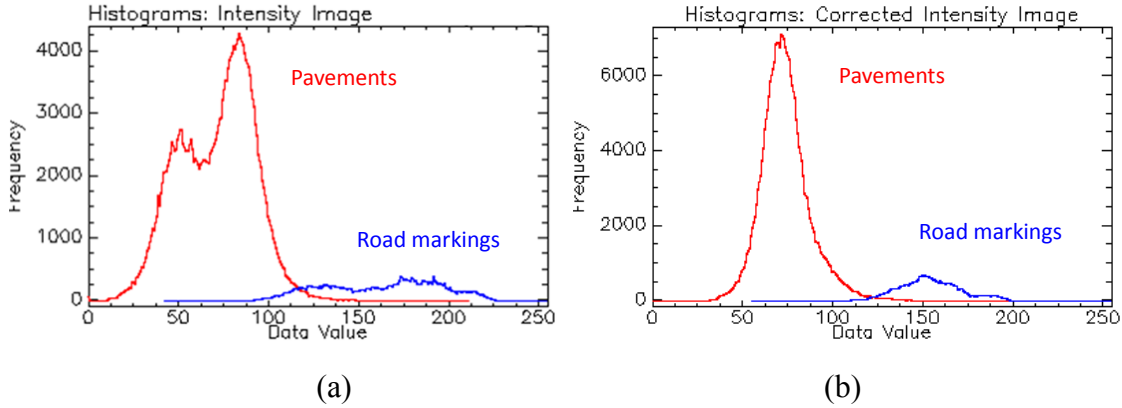


Figure 4.6: Histograms of the road markings and pavements: (a) the histogram of pavements and road markings in intensity image and (b) the histogram of pavements and road markings in corrected intensity image.

In summary, the intensity correction minimizes the in-class variance and keep the between-class variance still, thus, the road markings become more detectable. The results of the intensity correction indicate that the cosine of scan-angle-rank-based intensity correction works well on a global scale. Nonetheless, the intensity in some areas, which have different slopes and roughness, cannot be explained by the cosine of the scan angle rank.

## 4.2 High-pass Filter Enhancement and Accuracy Assessment

### 4.2.1 High-pass Filter Enhancement

In this section, the large-size high-pass kernel was validated using Sample02 and Sample06 to get the optimal size of the kernel. The corrected intensity image of Sample02 was processed by high-pass filters in different sizes. The intensity of no-data area in Sample02 is set to a constant value that is higher than the intensity of pavements and lower than the intensity of road markings. Therefore, the success of the high-pass enhancement can be guaranteed among the no-data pixels. The individual high-pass result is binarized by the Otsu's thresholding method, and the extraction results are assessed

using manually labeled references. The performance of individual high-pass enhancement is represented by the F-Score in an accuracy assessment. The F-Score of results with different sizes of the high-pass kernel is shown in Figure 4.7.

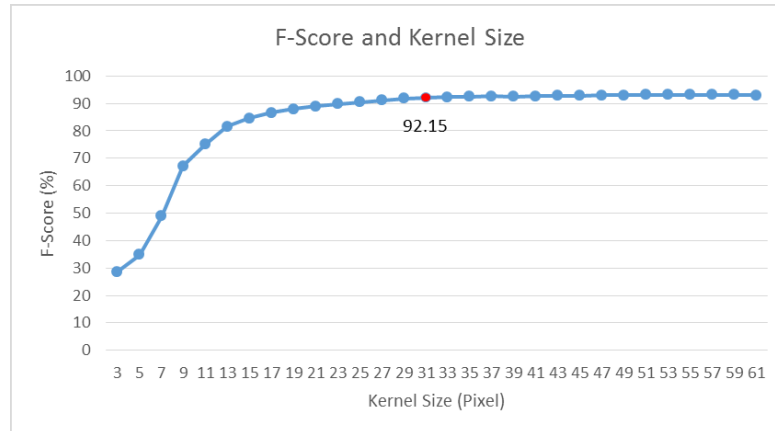


Figure 4.7: F-Score for each high-pass filter size based on Sample02.

The F-Score grows significantly with the increase of kernel sizes at the beginning, and it reaches 92.15% at size of 31×31. After the size of 31×31, F-Score grows smoothly with the increase of kernel size. As shown in Figure 4.8, the increase of the kernel size (from 3×3 to 31×31) makes the distinguishing of the road markings from the pavement much easier. When kernel size is bigger than 5×5 (25×25cm<sup>2</sup>), the thin road markings (15-20cm) (e.g. boundary line, centreline and traffic lane line) are detectable in the images. When kernel size is bigger than 11×11 (55-55cm<sup>2</sup>), the road markings with medium width (40-45cm) (e.g. stop line and a zebra crossing stripe) become detectable. When kernel size exceeds e 31×31 (155×155cm<sup>2</sup>), the widest road markings (e.g. road arrow) can be detected. With the result of Sample02, the minimum high-pass window size was determined to be 31×31 in order to achieve the detectability of the widest road markings.

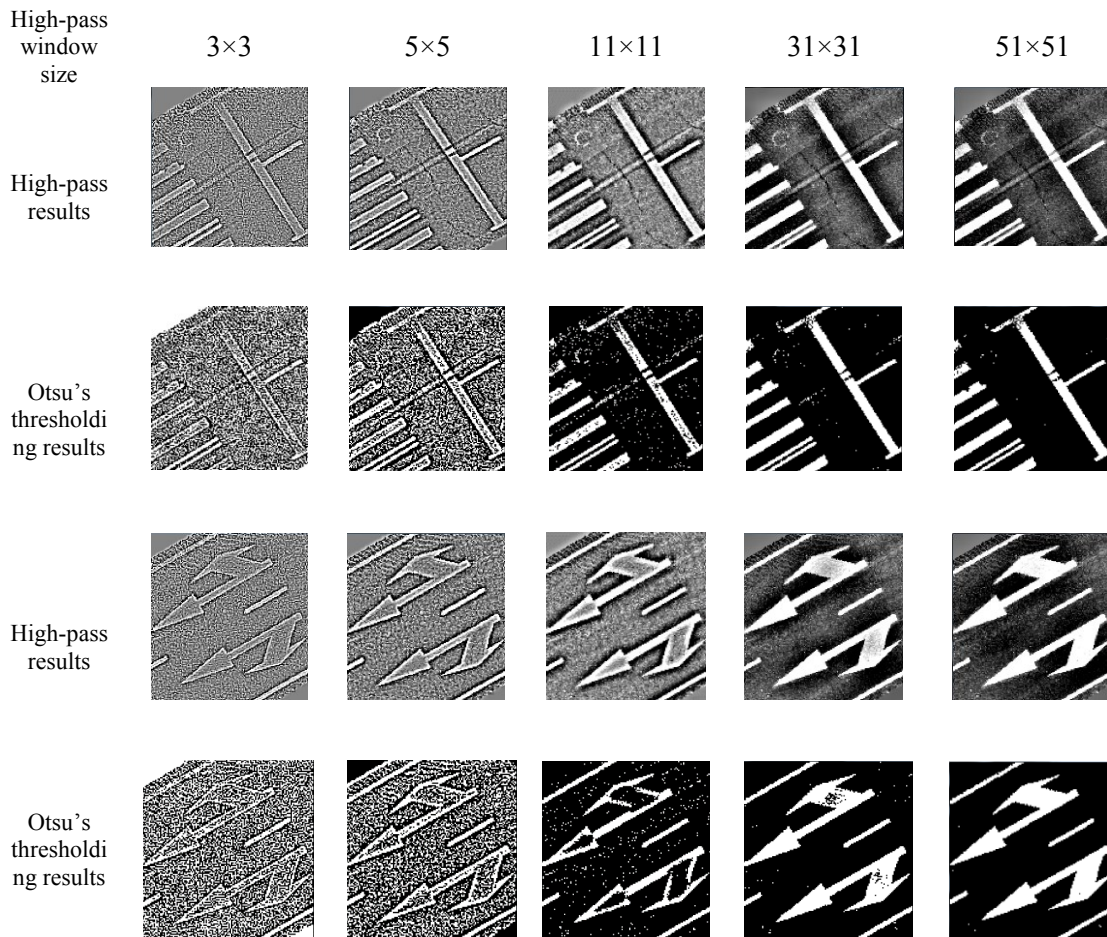


Figure 4.8: High-pass results with 3×3, 5×5, 11×11, 31×31, 51×51 kernel.

Based on the corrected intensity images, the 31×31 high-pass enhanced results are shown in Figure 4.9. The no-data areas are set as a specific value between the intensity of the pavement and the road markings. However, a constant value is not universally applicable. Thus, the following section will discuss the errors that are caused by the value setting in the case of no-data.

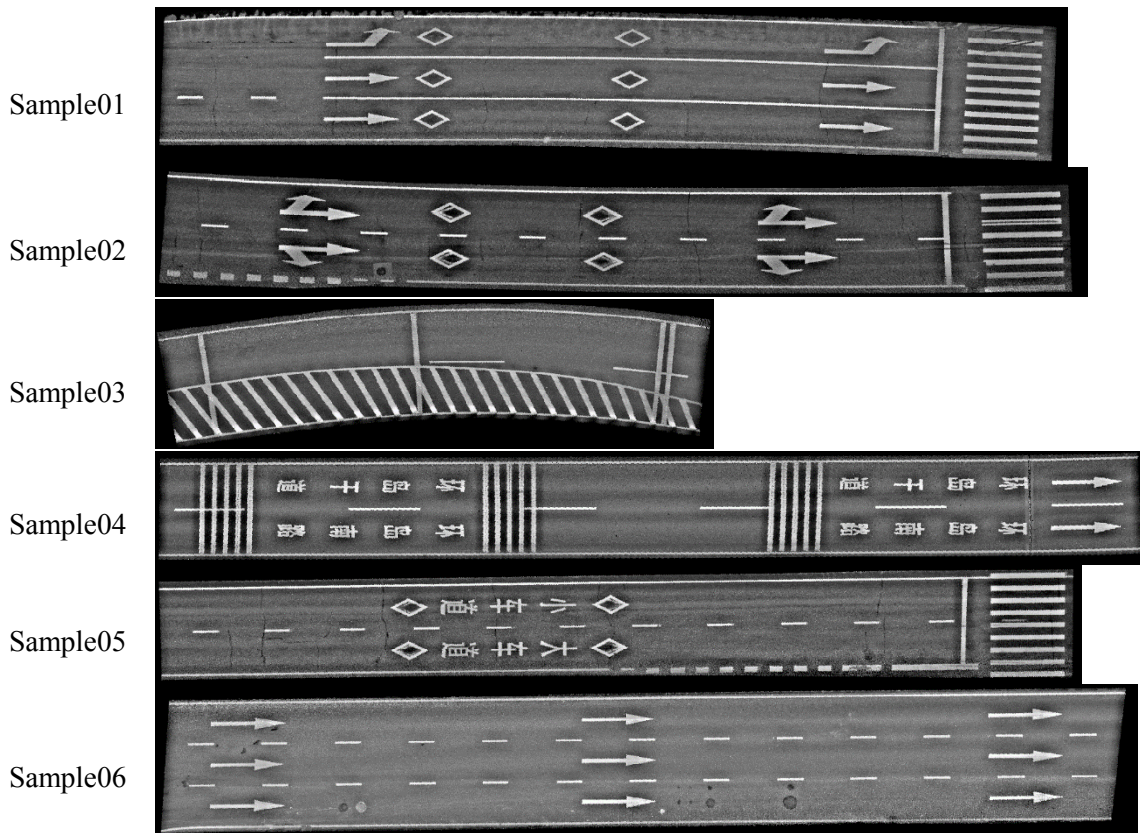


Figure 4.9: High-pass enhanced images with  $31 \times 31$  kernel.

Based on the high-pass enhanced image ( $31 \times 31$  kernel), the Otsu's thresholding results are shown in Figure 4.10. It is identified that majority of the road markings were extracted but with five errors.

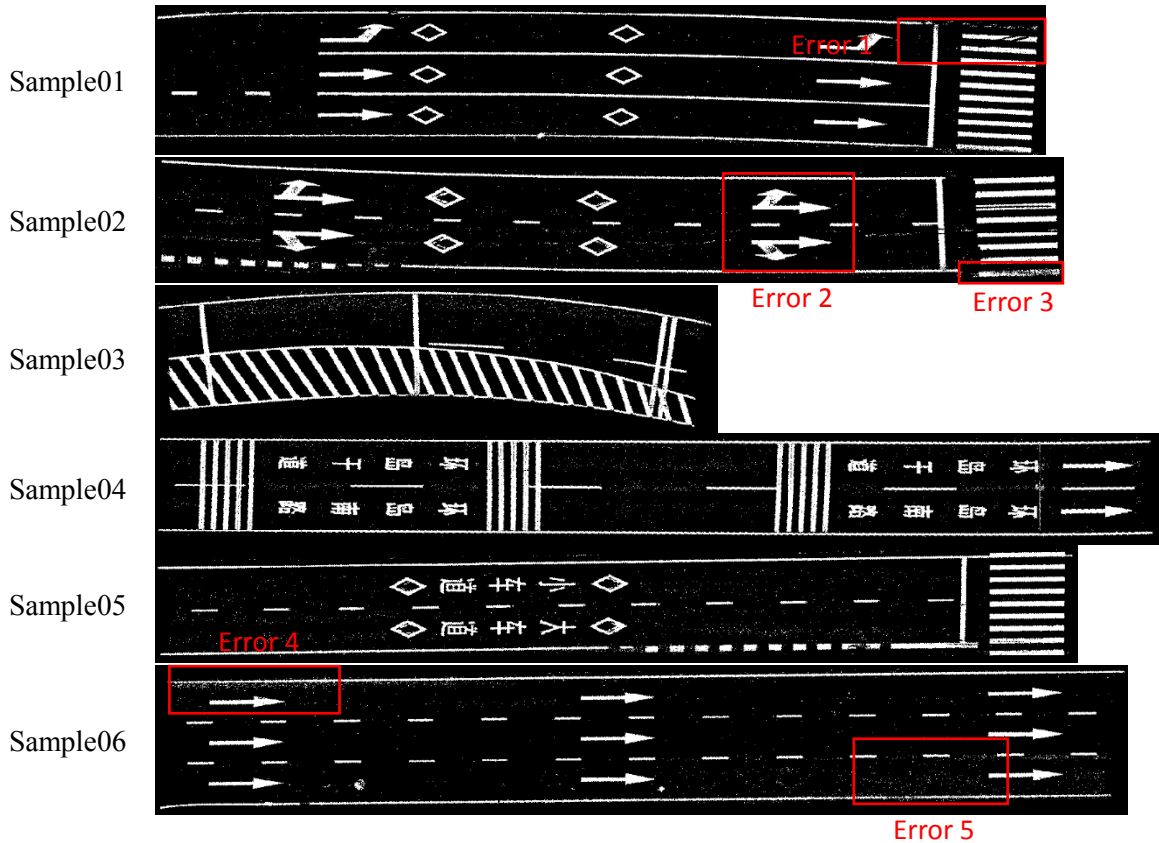


Figure 4.10: Otsu's thresholding results based on high-pass enhanced images from sample01 to Sample06.

As shown in Figure 4.11, error 1 is a typical misclassification of road marking caused by replacing no-data with a constant value. The road marking pixels with a lower value than the constant value are misclassified as pavements. This problem can be solved by setting the no-data area with a dynamic value. Error 2 is the false negative located in the inner of the road arrows. Applying a larger window size increase the amount of detected pixels inside the road markings. Error 3 is caused by lacking of sufficient laser points. The increase of the gaps between the laser points results in a low value that was interpolated into the intensity image. It is noted that the gaps can be eliminated using IDW interpolation with a larger pixel size. However, this method may lead to the loss of details in return. The noises in Error 4 and Error 5 are resulted from the roughness of the road. With the assistance of the intensity enhancement, the high intensity pixels of the

pavement were suppressed and identified as noise. In addition, the noise can be further eliminated using the region growing segmentation.

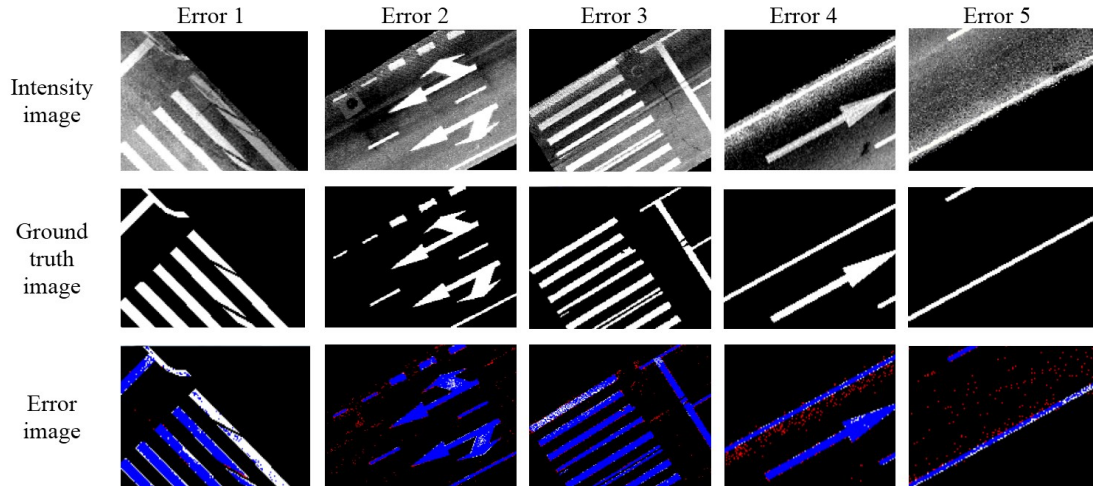


Figure 4.11: Intensity image, ground truth image (white: road marking pixels, black: pavement pixels), error image (white: False Negative, red: False Positives, blue: True Positives).

The no-data values were assigned dynamically, and defined as the three-time value of the average of its neighbours'. The road in Sample 06 is wider than the one in Sample02, therefore, the intensity variance is larger in Sample 06 is larger than Sample02's. Thus, the Sample06 is the supplement of Sample02 to reveal the decrease of F-Score with an increased high-pass filter size.

Figure 4.12 shows the F-Score of the test based on Sample06. The F-Score increased sharply with the size of the filter from  $3 \times 3$  to  $19 \times 19$ . From  $19 \times 19$  to  $29 \times 29$ , the F-Score increased smoothly, and it reached the peak (93.66%) at  $29 \times 29$ . After  $29 \times 29$ , the F-Score of extraction decreased with the increase of the filter size. This phenomenon was caused by the growth of the filters size when the spatial variance increased, high-pass process is influenced by the uneven intensity distribution. For example, if the small size kernel

processing the road boundary line that is far from the laser scanner, it actually compares the boundary line with the neighbouring pavement. If the kernel size is overlarge, the kernel will cover some brighter road markings pixels which are close to the vehicle's trajectory. In that case, the high-pass value of the boundary line will be restrained by the influence of brighter road markings. Therefore, the boundary line will be misclassified as a pavement and the accuracy of the extraction will decrease. The beginning of the trend in Figure 4.12 is similar to the case in Sample02 and then F-Score started to decrease after the kernel size reached  $29 \times 29$ . The Sample02 represents the case of extracting the largest road markings while Sample06 represents the case with significant spatial variance. To strike a balance between the capability of detecting large road markings and the immunity to spatial variance, the high-pass filter size should be set to  $31 \times 31$ . It can make the largest road markings detectable and avoid the generation of increased intensity variance in each window. Thus, the size of  $31 \times 31$  was identified to be the optimal size of the high-pass filter to improve the performance of the road marking extraction in Xiamen datasets.

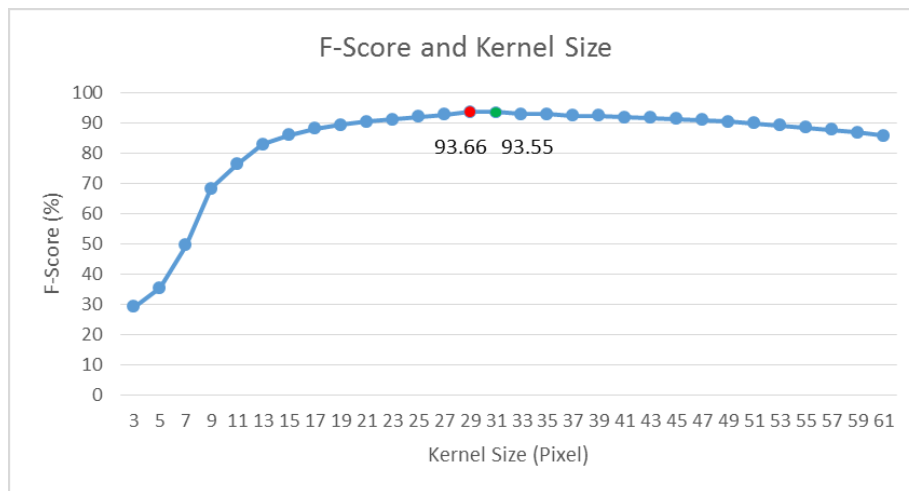


Figure 4.12: Performance of different high-pass filter with Sample06.



#### 4.2.2 Accuracy Assessment of Road Marking Extraction and Comparative Study

The final extraction result of road markings is shown in Figure 4.13.

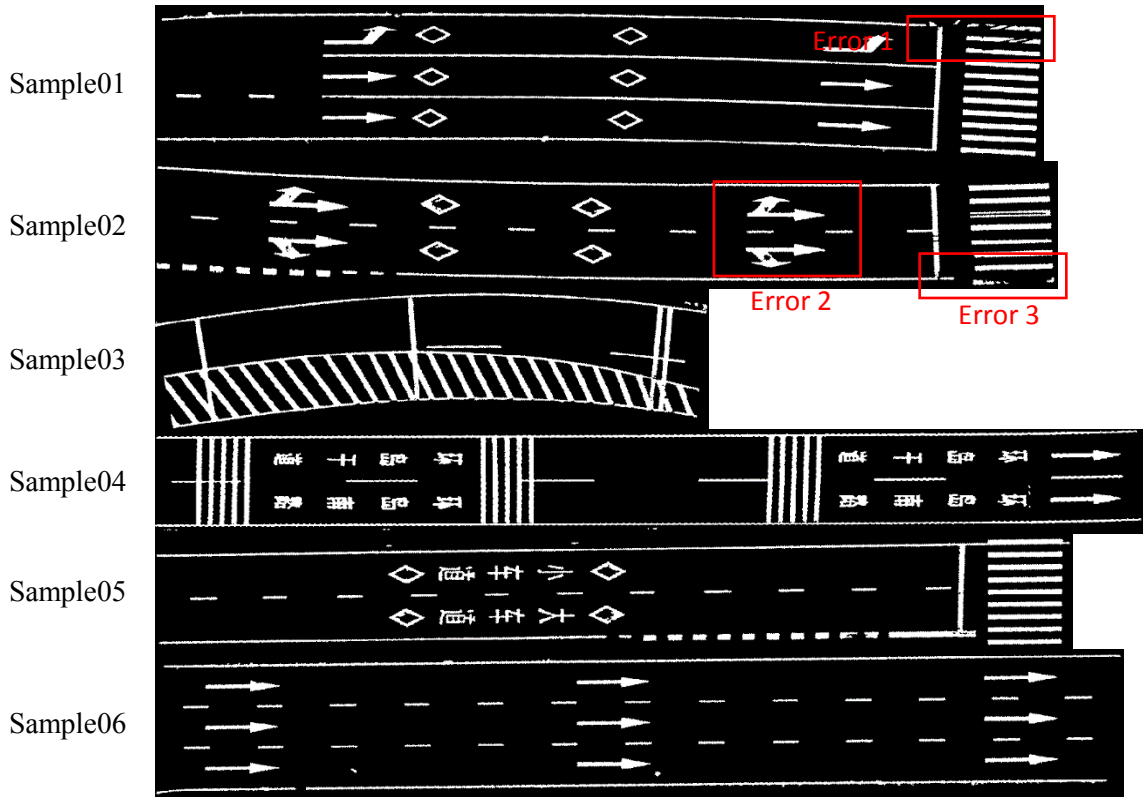


Figure 4.13: Results of road marking extraction.

After the preprocessing step, majority of the road markings are extracted from the image but three incomplete markings. The errors are caused by the road marking decay, the window size of the high-pass filter or the lack of sufficient laser points.

Table 4.2: Quantitative assessment using completeness, correctness and F-Score.

Performance (%)	Sample01	Sample02	Sample03	Sample04	Sample05	Sample06
Completeness	89.42	93.36	94.19	93.88	90.80	92.03
Correctness	96.02	93.55	96.06	95.60	97.50	95.12
F-Score	92.61	93.45	95.11	94.73	94.03	93.55

After the intensity correction and high-pass enhancement (31×31), the global Otsu's thresholding was implemented on the samples. The noises were removed from the

extraction results using  $3 \times 3$  median filtering and region growing method. As shown in the quantitative assessment (see Table 4.2), the proposed road marking extraction is capable to achieve 93% completeness, 95% correctness and 93% F-Score. The rate of completeness is smaller than the correctness's in each sample, indicating that some marking pixels were misclassified into the pavements. Due to the decay of the road markings, the sizes of manually labelled references are bigger than the damaged road markings'. Therefore, the performance of proposed method was underestimated in the result.

### **4.2.3 Comparative Study**

The following section will undertake a comparison between the results from the proposed method and other studies i.e. Chen's (Chen et al., 2009), Guan's (Guan et al., 2014) and Yu's methods (Yu et al., 2015). 2D intensity image generated from points clouds were used in Guan's and the proposed method for the extraction of road markings; while 3D point clouds were directly applied in the extraction practices in Chen's and Yu's studies. The evaluation results of these three methods are adapted from Yu's study as shown in Figure 4.14 and Figure 4.15. One of the limitations in Chen's method is that the extraction only focuses on the lane markings along the traffic direction Guan's, Yu's and the proposed method have extended the extraction boundary to any types of road markings.

Compared with Guan's approach, increased number of markings can be extracted using the proposed method, as shown in Figure 4.14(e) and 4.15(e). Based on the distribution of point density, Guan's method is capable to partition the road. However, Guan's method still suffered from the inconstant intensity, so that the road markings

could not be distinguished from the rough pavement near the road boundary (see Figure 4.14(c) and 4.15(c)). It is also noted that Yu's method is point-based while Guan's and proposed method are pixel-based. Therefore, Yu's method would not be affected by blurring data and achieves higher completeness than Guan's and proposed methods.

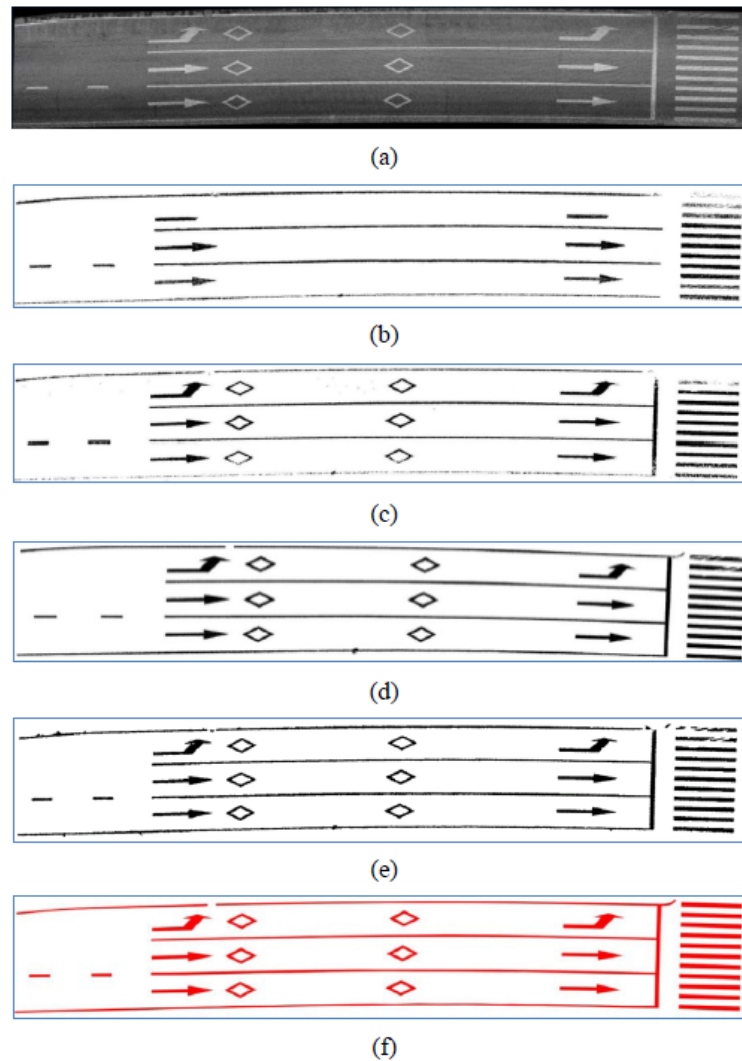


Figure 4.14: Extracted road markings from Sample 01 dataset: (a) road surface points, (b) Chen's method result, (c) Guan's method result, (d) Yu's method result, (e) proposed method result, and manually labeled reference data (Adapted from: Yu, 2015).

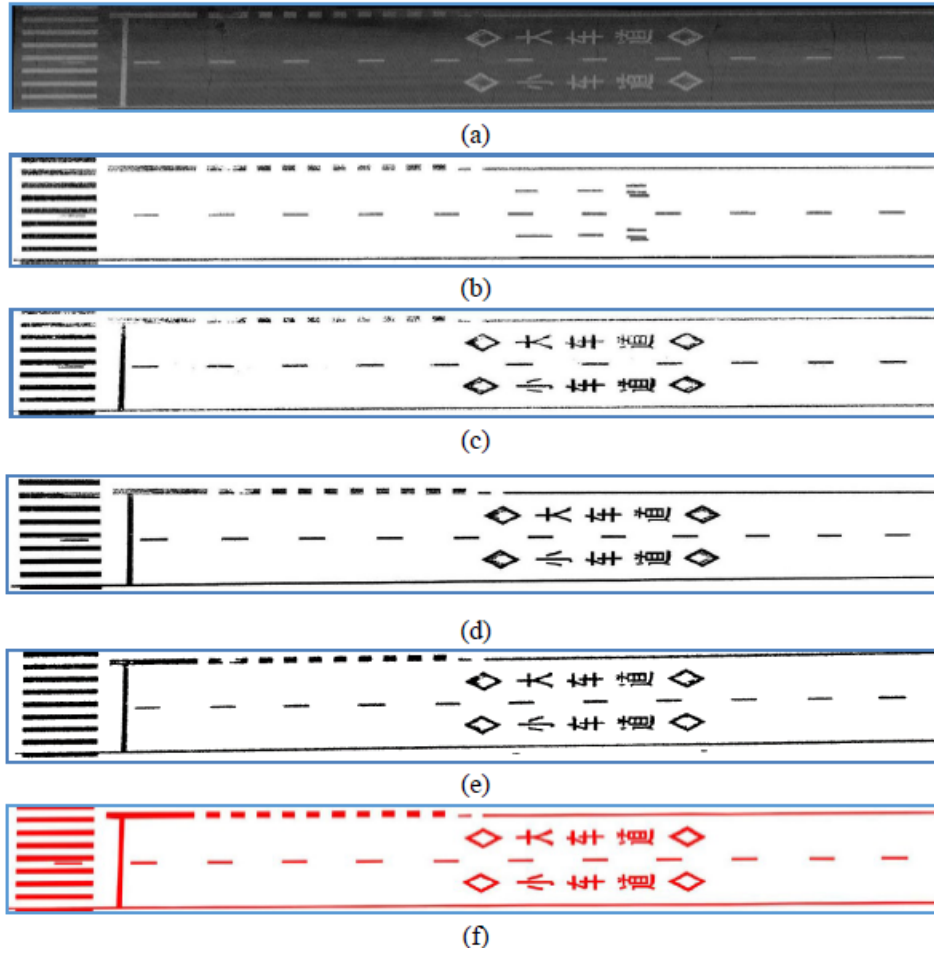


Figure 4.15: Extracted road markings from Sample 05 dataset: (a) road surface points, (b) Chen's method result, (c) Guan's method result, (d) Yu's method result, (e) proposed method result, and manually labeled reference data (Adapted from: Yu, 2015).

The performance of these four methods is evaluated in a quantitative way, using three variables, i.e. completeness, correctness and F-score (see Table 4.3). It is identified that the proposed method outmatches Chen's and Guan's methods while it is inferior to Yu's method in terms of the completeness.

Table 4.3: Quantitative evaluation results of different road marking extraction methods.

Sample	Sample 01				Sample 05			
	Chen	Guan	Yu	Proposed	Chen	Guan	Yu	Proposed
Completeness (%)	75	86	93	89	71	89	93	91
Correctness (%)	91	90	92	96	92	91	91	98
F-Score (%)	82	88	93	92	80	90	92	94

### 4.3 Road Marking Segmentation

Before the classification process, a road marking was segmented into the clusters by 4-neighbours region growing segmentation. The segmentation results from road marking extraction are presented in Figure 4.16. Based on the neighbour counting filtering, the large regions of the road markings were segmented successfully except in Sample03. The reserve area that was segmented into pieces cannot be interpreted correctly in Sample03.

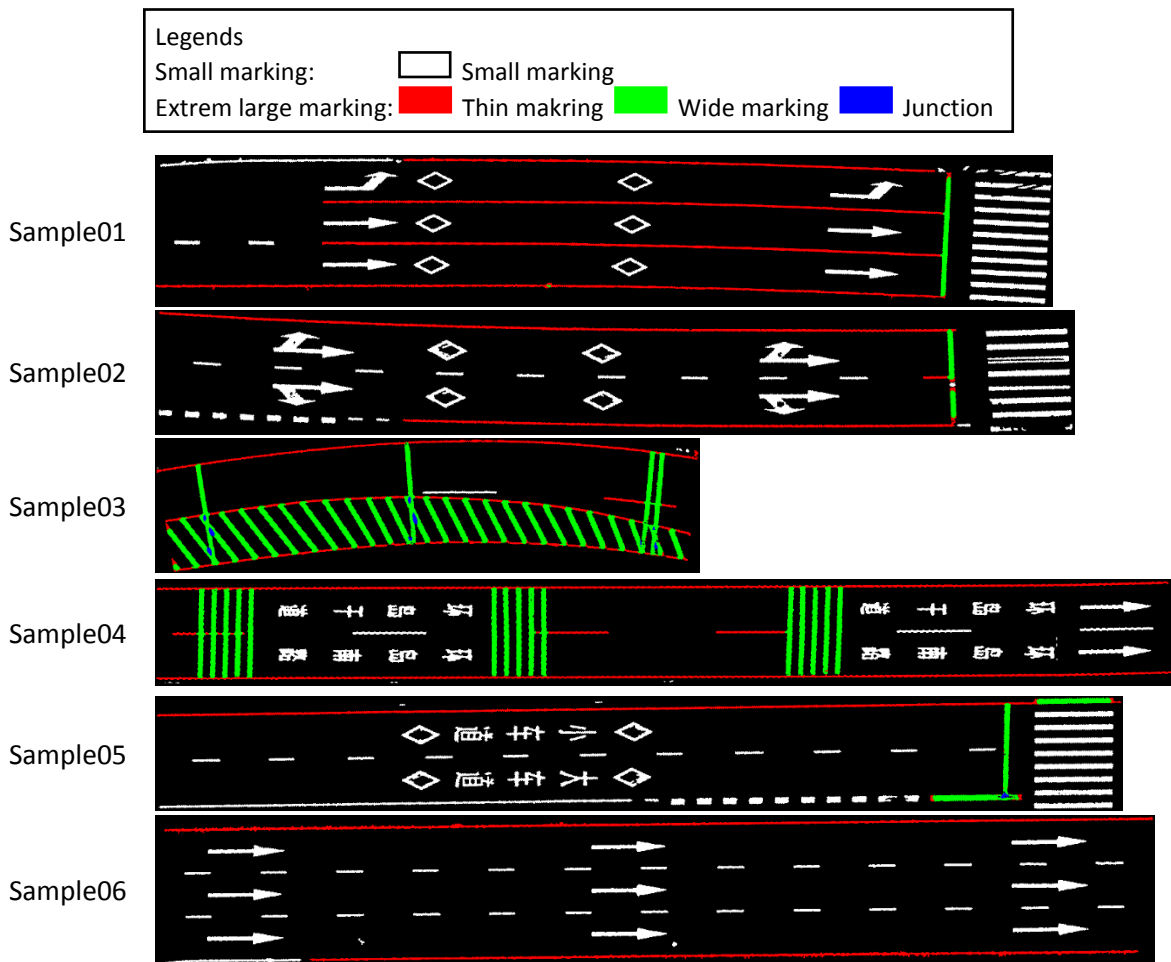


Figure 4.16: Results of road marking clustering and segmentation.

#### 4.4 Road Marking Classification

The marking segments were classified into categories based on the decision tree. All kinds of the road markings in the samples are illustrated in Figure 4.17. It is identified that majority of the segments were classified into correct categories. Nevertheless, three problems arose in the classification.

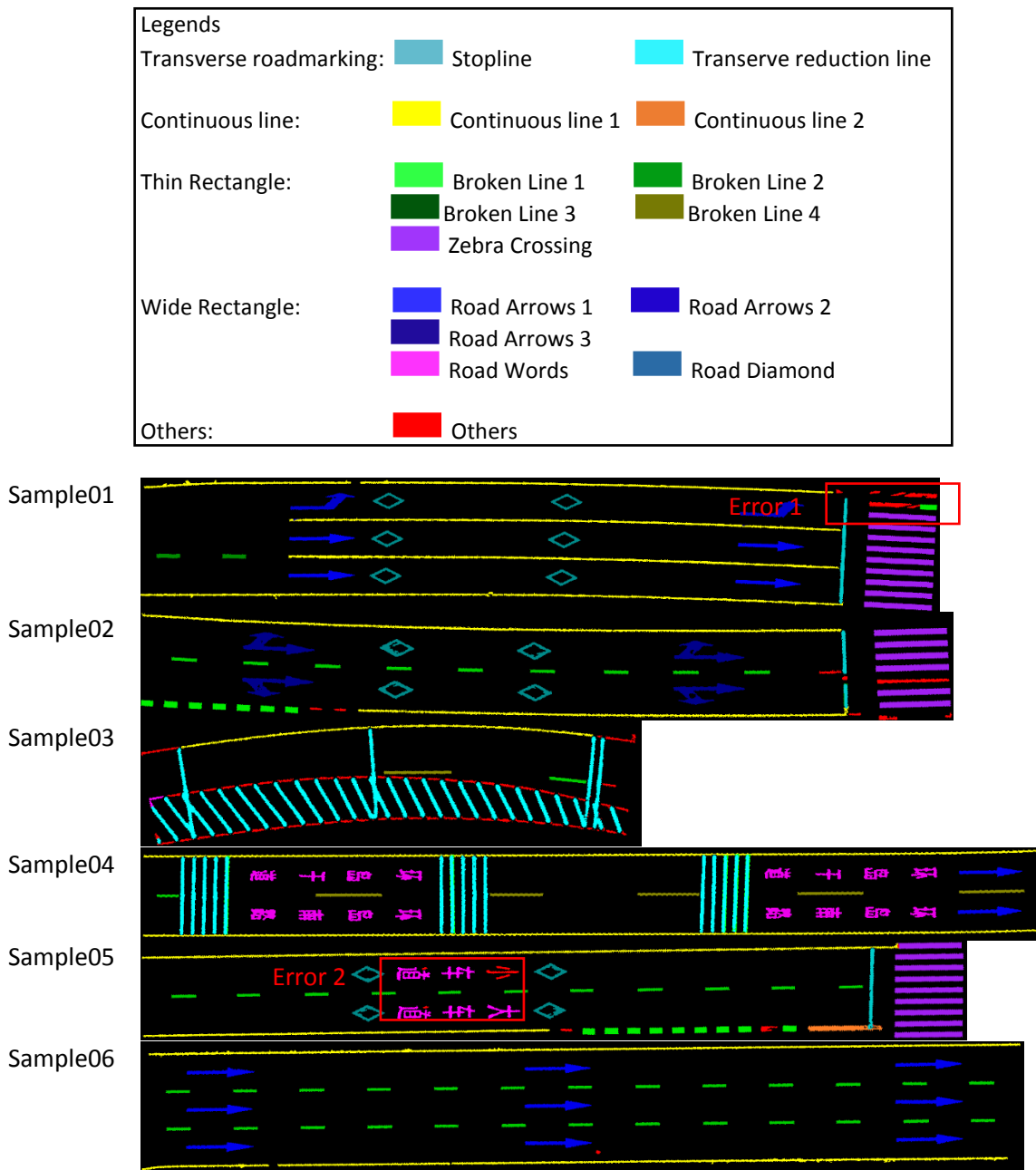


Figure 4.17: Results of road marking classification.

Resulting from these three problems, there were number of unclassified road marking segments within the images. In order to solve the issue caused by the marking decay, a rectification method was employed to group the unclassified segment to its nearest road marking. The principle behinds this method is that the damaged road marking still inherit the major features with its congeneric markings.

In order to overcome the difficulty in the identification of the Chinese characters, it was proposed to expand the segments of the strokes. Thus, the strokes would be easier to be grouped as a unit. The dilation, as one of the basic operators in the area of mathematical morphology, was used to unite the strokes. The use of the dilation and its recognition result are presented in Figure 4.19.



Figure 4.18: Errors of road marking classification.

Aiming at these unclassifiable segments, causing by marking decay, a rectification method can correct these misclassifications. The basic idea is that these unclassified segments should be reclassified according to the confessedly recognized road marking segments. Based on these correctly classified road-marking segments, the near unclassified segment can be set into the closest road marking. Although the damaged road marking cannot be classified correctly by its geometric features, it still has a strong spatial relationship with its congeneric markings.

In order to identify Chinese characters, successfully separating the strokes becomes

the crucial point. One solution is to expand the segments of strokes to generate them to become one connected region, and then detected as one character correctly. The dilation, as one of the basic operators in the area of mathematical morphology, was tested to connect separate strokes. Figure 4.19 shows the dilation of Chinese characters and the recognition result. After region expanding, the strokes in one connect area can be classified as one character.

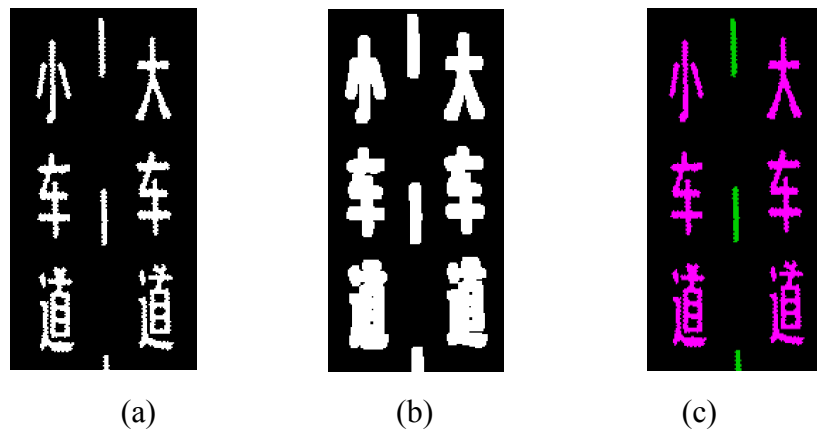
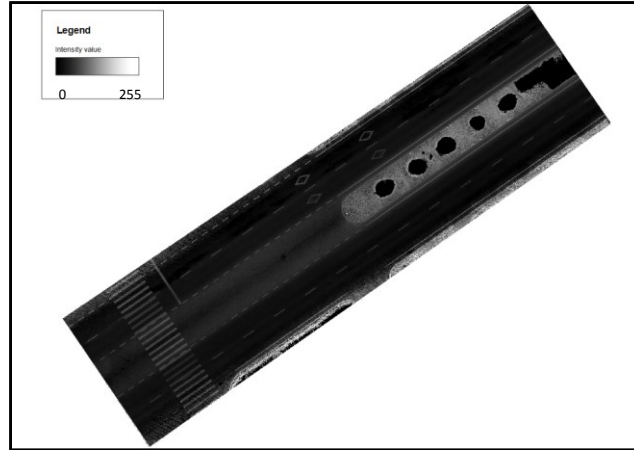


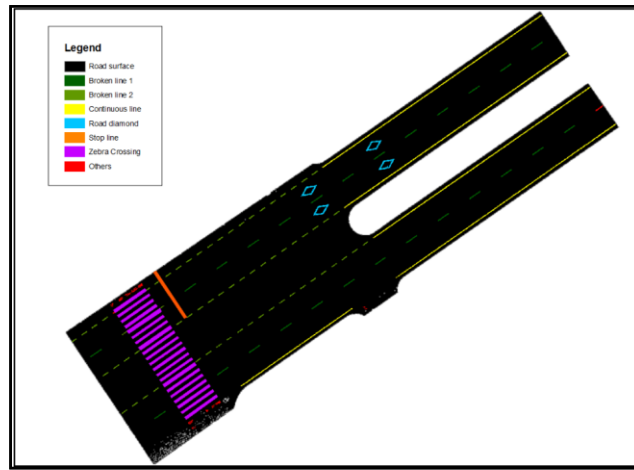
Figure 4.19: Detection of Chinese characters: (a) road marking region, (b) dilated road marking region, (c) Chinese characters classified in dilated region.

Since the proposed method is based on the global threshold strategy, it can process the multi-path MLS data. Since the MLS dataset in Xiamen was retrieved from a round-trip survey, it consists of both back and forth point cloud data. Compared to the distance-dependent road marking detection, the proposed method can process the entire dataset at one time without the trajectory data. The intensity image of the road surface and extraction results of Sample07 is shown in Figure 4.20.





(a)



(b)

Figure 4.20: Road marking extraction of sample07 in Xiamen (a) road surface intensity image, (b) road marking extraction result.

#### 4.5 A Case Study on Road Marking Classification in Kingston

The proposed method was initially implemented with MLS data acquired in Xiamen. In order to test the feasibility of the proposed method in Canada's road network, a case study was carried out in the City of Kingston. It should be noted that the MLS data acquired in Kingston is more challenging due to the impacts from climate condition difference, topographic variability, and the resultant pavement aging. The pavement cracking, rutting, potholes and aged asphalt pavement surface would be the sources that generate noises in Kingston's MLS data. The noises would have effect on the application

of the Otsu's thresholding in extracting road marking successfully. Hence, the threshold in the road-marking extraction was set to be lower than the Otsu's method's. However, this set-up may lead to the generation of a number of false positive pixels included in the road marking. The source of these false positive pixels will be discussed in Section 4.5.1. Additionally, the denoising methods are applied to remove these false positive pixels.

The following section consists of three parts. First, the challenges and countermeasures for the Kingston's study were discussed. The second section aims to validate the efficiency of using maximum intensity in the corrected image for road marking extraction in which different methods for rasterizations of point clouds were employed and compared. In the third section, based on the corrected image data in the Kingston's study, maximum and mean intensities were utilised in an overlapping analysis to monitor the decay of the road markings.

#### **4.5.1 Challenges and Adjustments**

There are four major challenges on processing the Kingston dataset using the method proposed within this research.

The first challenge is the flexibility of adapting this method in different pavement marking guides. In general, the road markings are similar in the worldwide but with differences e.g. between major and local roads. It is noted that the sampled roads in Xiamen are major roads that are more complicated than the local roads in Kingston. Thus, the decision tree needs to be adjusted based on the Ontario Traffic Manual (2000).

The second challenge is the ability to accurately extract the pure road surface in different circumstance. Different from the main roads in Xiamen with a continuous

connectivity, the sample from Kingston is a local street where the sidewalks connect to the drive road at the crossroad and many cracks occur on the roads. The differences would impact the performance of the extraction so that the threshold was modified to separate the road surface from the sidewalks (see Figure 4.21(b)). In addition, the fractures of the road marking would be obtained from the extraction of the incomplete pavement surface, which makes the road marking recognition very difficult. Thus, it is proposed that the candidate markings were first filtered with an overlapping area of the road surface. As shown in Figure 4.21 (b), occupying 40% of the road surface, the road markings are identified and labelled successfully.

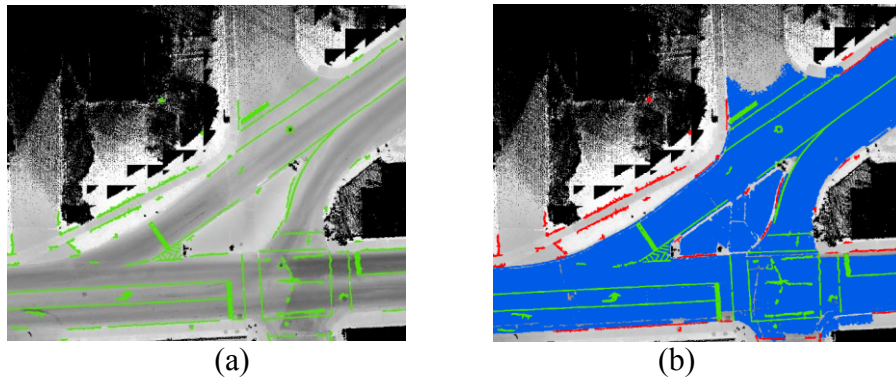


Figure 4.21: Road surface detection in Kingston's sample: (a) candidate road markings (green) (b) road surface coverage thresholding result, including road surface (blue), road markings (green), and non-marking segments (red).

The third challenge is how to overcome the effect of the pavement distortion on the intensity correction. One of the assumptions in the proposed intensity correction method is that the road surface would be flat. However, the intensity variance caused by the grooves on the road cannot be mitigated using the proposed correction method but leads to the generation of some noises.

Within this study, individual noises can be eliminated using region growing

segmentation, and the noise clusters can be detected in the period of road marking classification with a specific geometric parameter (i.e. rectangularity). Rectangularity is the ratio of the object area to the minimal bounding box area, used to distinguish the noise clusters from the road markings. Furthermore, the neighbour-counting filtering can also be applied to eliminate the noises. The neighbours' number of the road marking pixels are counted within a window size of  $15 \times 15$ . For example, the pixels in the centre of the noise clusters have a large number of neighbours. Thus, the density filtering was employed to remove the center pixels of the noise cluster and make the road marking lines distinguishable from the background. The line road markings before and after the density filtering are shown in Figure 4.21(a) and Figure 4.21(b), respectively.

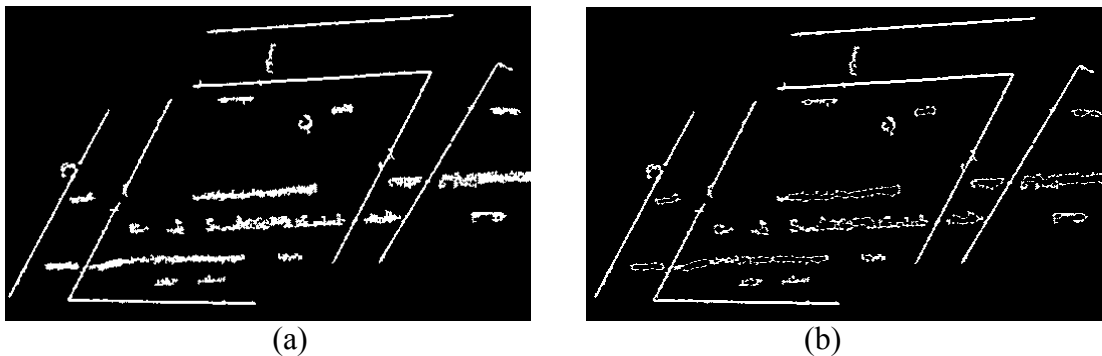


Figure 4.22: Density filtering of road marking: (a) road marking with noise, and (b) density filtering result of (a).

The fourth challenge is the identification of the damaged road markings. As discussed in section 4.4, the proposed decision tree is very sensitive to the decay of the road markings. Due to the cold winter condition and excessive loading, the occurrence of cracking and road marking decay is inevitable. Cracks in the road surfaces arising from both the Canada's climatic conditions and excessive traffic loading, makes the decay of the road markings almost inevitable.

It is identified that the broken road marking segments can be extracted and classified by reclassification strategy. For example, the unclassified road markings highlighted in red in Figure 4.23(a) cannot be recognized using the decision tree. Based on the reclassification criteria, they were grouped into the nearest road markings (see Figure 4.23(b)).

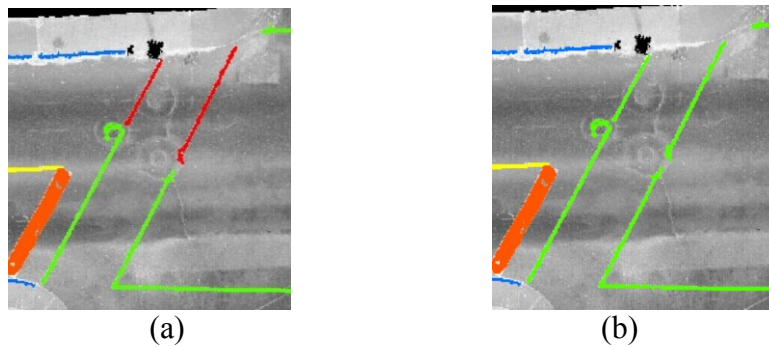


Figure 4.23: A remedial measure of road marking: (a) the unclassified marking segments, and (b) result of the rectification method.

#### 4.5.2 Results and Discussion

To overcome the challenges discussed in the previous section, a series of approaches were applied.

Both the IDW interpolation and maximum value enhancement were utilised to generate intensity images for road marking extraction. The IDW mean corrected intensity image and maximum intensity corrected image are presented in Figure 4.24 (a) and (b). It is noted that the road arrow was brighter and more complete in the Figure 4.24(b), compared to the one in Figure 4.24(a). Figures 4.24(c) and (d) show the results of road marking extraction from the IDW mean intensity corrected image and the maximum intensity corrected image respectively. As shown in Figure 4.24(c) and Figure 4.24(d), the extraction result from maximum intensity corrected images was more nearly complete

and clear.

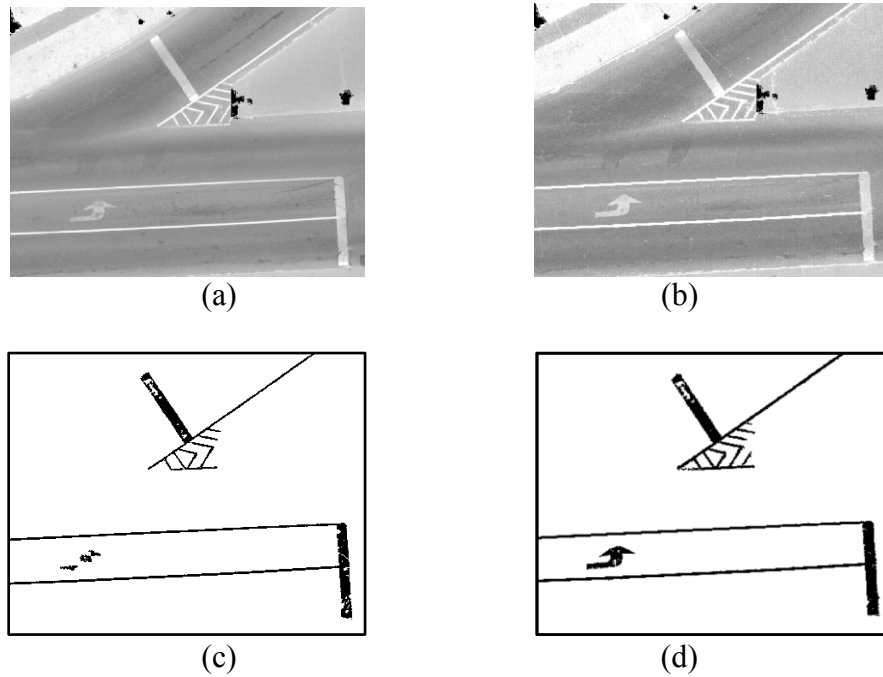


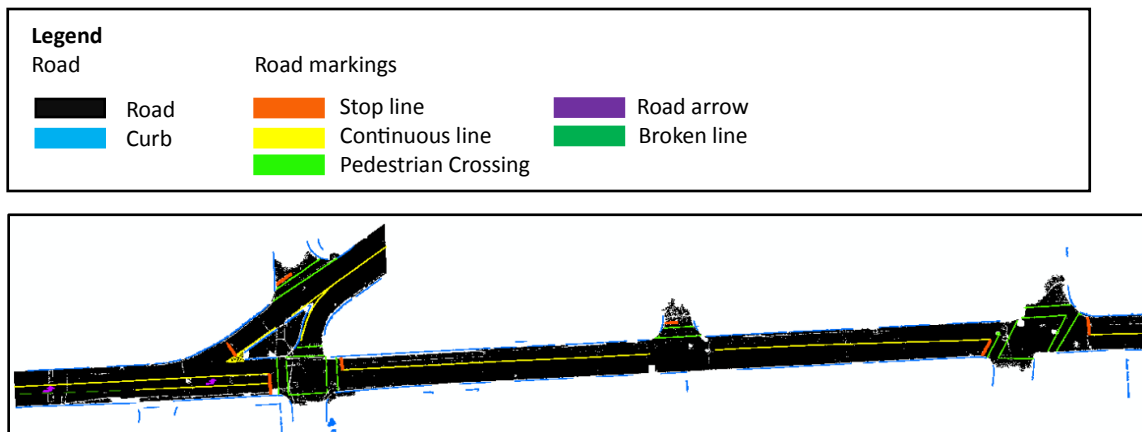
Figure 4.24: IDW interpolation vs Maximum value enhancement: (a) IDW mean intensity image, (b) the maximum corrected-intensity image, (c) road marking extraction result from IDW mean corrected-intensity image, and (d) road marking extraction result from maximum corrected-intensity image.

In addition, compared to IDW interpolation, the maximum value enhancement can be used to improve the road marking extraction performance. Based on the assessment of three variables (correctness, completeness and F-score), the comparison results is illustrated in Table 4.4. It is clear that the maximum intensity contributes to the enhancement of the fade marking and improves the performance of the extraction significantly.

Table 4.4: Comparison of the road marking results from different rasterization methods.

Rasterization method	IDW interpolation	Maximum value enhancement
Correctness (%)	82.95	93.47
Completeness (%)	76.79	84.16
F-Score (%)	79.75	88.57

Based on the Kingston dataset, the final classification result of the road markings is shown in Figure 4.25. Based on a  $3 \times 3$  high-pass filtering result of DTM, the road surface and curbs were detected and shown in black and blue (see Figure 4.25(a)). However, the corrected and enhanced intensity image was not qualified to be masked before the road marking extraction. Therefore, high-pass enhancement and filtering were employed in the maximum intensity corrected image for all road marking candidates. The road markings whose majority of it located on the road surface were labelled as road marking, and the others were classified as non-markings and removed. It should be noted that a modified decision tree and a reclassification strategy were utilised to classify the road markings. A number of criteria were developed for the classification of both detected and undetected segments. For example, the broken pedestrian crossing lines caused by the road marking decays were reclassified successfully as shown in Figure 4.25(b) and Figure 4.25(c).



(a)

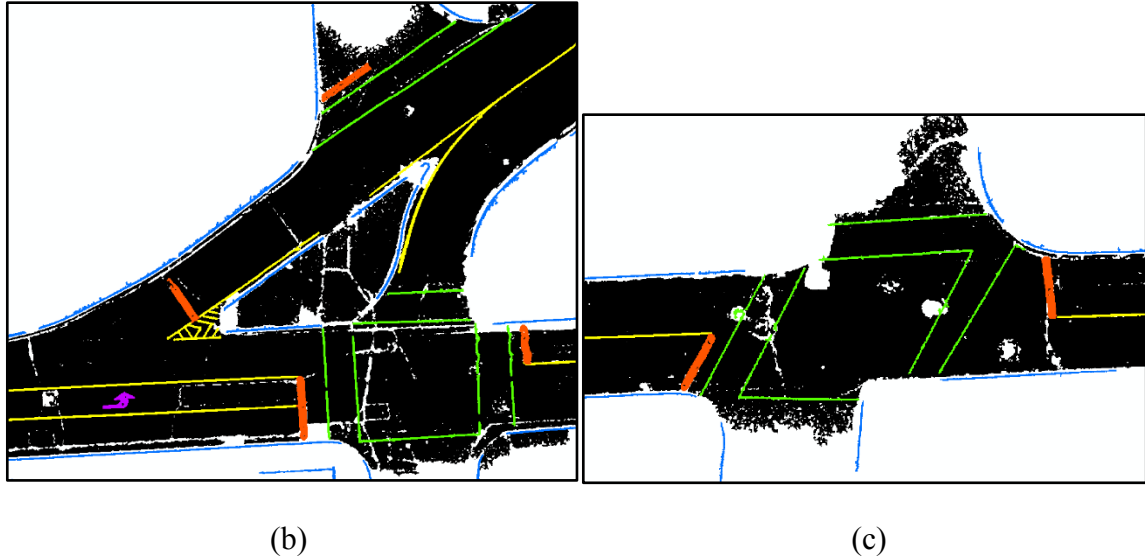


Figure 4.25: Road marking classification in Kingston: (a) overview of road marking classes, black area represent detected road surface, blue lines represent curbs, (b) road intersection 1, (c) road intersection 2.

Based on the quantitative assessment results, it is identified that the extraction performance using the Kingston dataset was not as good as the Xiamen's. The values of three parameters (correctness, completeness and F-score) achieved from the Kingston's case were lower than the ones obtained from the Xiamen's case (see Table 4.5). The reason behinds this result is that the road marking detection is significantly affected by the road marking decay and digital erosion. On one hand, the road markings in King Street (Kingston) are in disrepair. Due to the winter maintenance and traffic, the road markings have heavy reflectance losses and cannot be extracted correctly. For example, the completeness of the road arrows and the pedestrian crossing lines are 81% and 82%, respectively. On the other hand, the region growing method was used to remove the noises and group the road marking pixels. It is identified that, it removes the small fragments of damaged road markings inevitably. As a result, without shape features, these damaged road markings cannot be recognised by the decision tree as standard road markings. Therefore, both the decay and the digital erosion result in the relatively low



completeness in the Kingston’s case within this research.

Table 4.5: Quantitative assessment results using the Kingston dataset

Performance(%)	Correctness	Completeness	F-Score
Road markings			
Continuous line	93.26	85.86	89.41
Stop line	98.24	83.03	89.99
Road Arrow	99.82	80.96	89.41
Broken line	90.97	86.95	89.91
Pedestrian crossing	90.34	81.79	85.85
Overall (Kingston)	93.47	84.16	88.57
Overall (Xiamen)	95	93	94

#### 4.6 Chapter Summary

This chapter analyzed the performance of the application of the proposed method in Xiamen and Kingston. The main discussion and analysis were based on the performances of the preprocessing, extraction and classification in Xiamen dataset. The case study in Kingston was discussed and analyzed as the complementary case for the proposed method. The Xiamen dataset was mainly used to demonstrate the performance of the processes, including the preprocessing, extraction and classification. The Kingston dataset was employed as a complementary case for the application of the proposed method.

With the IDW interpolation with the grid size of 5 cm, large amounts of 3D point clouds were transferred to 2D images, thus the computation efficiency was significantly improved. In addition, two methods (i.e. scan-angle-rank-based intensity correction and large-size-high-pass enhancement) were used to solve the effect caused by the uneven distribution of the MLS interpolated intensity data. The function of cosine was used to correct the intensity data and achieve a normal distribution of the histogram of the road

marking pixels. Therefore, the contrast between the road markings and the pavements was enhanced. Furthermore, in order to eliminate the spatial variance of the road marking in the road boundary, a large size high-pass enhancement was employed with 30 different window sizes. The Otsu's method was then applied to segment the images, whose performance was tested based on the evaluation of three parameters, i.e. completeness, correctness and F-score. It is identified that the optimal size of the large window for high-pass enhancement is  $31 \times 31$ .

Compared with the others three recently published MLS data based road marking detection methods, the proposed method has its advantages. First, the proposed method employed the function, i.e. cosine of scanning angle to correct the intensity value. Second, a large size high-pass filter was utilized to overcome the uneven intensity issue. As a result of these two steps, the road markings became more detectable from the pavements. Thus, the global Otsu's thresholding can be implemented successfully to extract the road markings. It is noted that "true" image can be produced using IDW interpolation, but replacing the IDW interpolation value with a maximum corrected intensity generates increased numbers of road marking pixels for further extraction and classification.

After the extraction, road markings were segmented by 4-neighbour-region growing segmentation process. The extreme large road markings were divided into transverse markings, wide longitudinal markings and thin longitudinal markings. Based on the geometric features, these road marking segments were classified into corresponding categories. The main problems of the proposed method lie on the classification of the damaged road markings and the isolated strokes of Chinese characters. With the expansion of the dilation kernel, Chinese characters can be grouped and recognized as

one marking. A reclassification strategy was also developed and implemented for the unclassified broken road markings in the case studies. It is noted that the decision tree would need adjustment due to the difference of climate condition and topography, and the pavement ageing effect. In addition, the noises generated in Kingston's case were successfully eliminated using the density filtering approach.

A number of features were used in the road marking classification process, including its connectivity, area, width, bounding box, rectangularity and spatial relationship. In the Kingston's case study, both the maximum and mean intensity corrected images were generated associated with two results. It is identified that the maximum value enhancement of intensity helps scale up the road markings' spectral characteristic with increased numbers of marking-alike pixels. Therefore, the utilization of the maximum intensity interpolation in the road marking extraction results in higher completeness, correctness and F-Score than the extraction result using IDW interpolation approach.

## Chapter 5 Conclusions and Recommendations

### 5.1 Conclusions

The main conclusions of this study can be summarized as follows:

The driverless car, as one of the most viable forms of ITS, has been developed by many automotive and other companies, and fully-autonomous vehicles are predicted to be launched in the next 5 years. It is noted that the sensors and a prior 3D map are the key elements of the driverless cars. In addition, one of the biggest challenges to develop the prior 3D maps lies in the generation of the lane model with the precise lane geometry and rich attributions. The Mobile Laser Scanning (MLS) technology is also essential for capturing the point clouds that are used to detect the road markings.

Majority of the existing MLS point clouds-based road marking extraction methods are based on the application of global intensity filtering and multi-thresholding segmentation. However, these methods could be greatly influenced by the unevenly distributed intensity. This highlights the need for well-developed preprocessing before the road marking extraction. The preprocessing aims at eliminating the in-class variance of road markings and thus improving the marking detection. Additionally, the machine learning algorithms are normally utilized in road marking classification and its application requires extensive training effort. Hence, this study has proposed a decision tree that is able to classify the road markings in a detailed and efficient way.

This study has highlighted that the application of the scan-angle-rank-based intensity correction and the large-size high-pass filtering have the potential to significantly reduce the in-class variance of road markings and pavements. In addition, based on the

comprehensive prior knowledge, a shape-based hierarchical tree developed in this study is capable to undertake the classification in an efficient and systematic manner. It should be noted that the efficiency of the intensity correction method greatly depends on the flatness of the road surface (e.g. cracking, rutting). Furthermore, the proposed workflow may not be able to achieve the ideal performance on poor road conditions due to the road marking decay. Therefore, the neighbors-based filtering and region growing algorithm have been applied in maximum intensity images to eliminate the noise caused by cracking and rutting.

Two case studies have been undertaken to demonstrate the applicability of the proposed workflow. They also aimed at evaluating the performance of the developed methodology using different MLS datasets acquired from various roadway environments. The comprehensive prior knowledge was applied to assess the accuracy of the road marking classification. Based on the case study results, the preprocessing has attenuated the intensity variance of road makings and improved the extraction performance. It has also been highlighted that the road conditions (i.e., flatness of the road surface, completeness of the road markings) have a great impact on the accuracy of extraction and sequent classification.

The thesis has concluded that the developed workflow is capable of rapid extraction and classification of the road markings in the MLS point clouds.

## **5.2 Contributions**

This section presents four principal research contributions to the study of road marking extraction and classification.

This section summarizes the main contributions of this thesis.

(1) **The hybrid road-surface extraction** method for road surface detection has been developed. Based on the ground points generated by the voxel-based upward growing algorithm, the  $3 \times 3$  high-pass kernel was applied to generate the DTM. Then the road surface was extracted based on the smoothness and connectivity of the road. Different from the surface growing approach (Vosselman et al., 2004), the hybrid method involved the removal of the non-ground points and the integration of the point cloud into DTM. It aims at reducing the data volume prior to the extraction step. At the same time, the hybrid method inherited the advantage of the pixel-based region growing algorithm to take the smoothness and connectivity into consideration in 2D images. Thus, the hybrid method can be used to extract the road surface rapidly.

(2) **The scan-angle-rank-based intensity correction** has been undertaken to attenuate the intensity variance caused by varying incidence angles. The in-class variance of the road markings has dropped significantly after the intensity correction. In addition, the improved efficiency of the intensity correction has demonstrated that radiometric calibration was critical for the road marking extraction.

(3) **The large-size high-pass filter** has been utilised to attenuate the intensity variance caused by different surface roughness to ensure the realization of the global thresholding. The selection of an optimal size of high-pass filter can enhance the road markings from pavements and reduce the spatial variance in the kernel. Compared with the application of multi-thresholding segmentation in others' studies, the large-size high-pass filter used in this research resulted in less spatial variance, and a better road marking extraction performance. The improved filter efficiency demonstrates the applicability of

the window-based extraction approach.

(4) **The shape-based hierarchical tree** for road markings classification has been developed based on the comprehensive prior knowledge of the road-marking shapes. On the basis of the hierarchical tree, a decision-tree for classification can be manually developed and classify the road markings into detailed categories. It is noted that the hierarchical tree has the flexibility to meet different requirements, either for a rough or detailed classification. In general, the diarchy tree is able to classify the road markings into detailed categories including the information of precise lane geometry and rich attributions. The hierarchical tree is superior to other machine learning classifiers because it does not need any training process. The prior knowledge of the traffic markings were coded into the trees manually. Moreover, the development of the hierarchical tree requires less computation than the use of template matching algorithm.

In conclusion, the manually developed hierarchical tree can be easily integrated with human prior knowledge and used to classify the road markings. In addition, the detailed classification result, as an indispensable data source, was used for developing the prior 3D map to support the operation of driverless cars.

### **5.3 Recommendations for Future Studies**

This section presents the limitations of the proposed method and discusses the future work.

#### **5.3.1 Point Cloud Intensity Correction**

The scan-angle-rank-based correction of intensity has enhanced the contrast between pavements and markings significantly. However, the efficiency of the method depends on

the flatness of the road surface. The cracking, rutting and potholes, which are not in compliance with the plane model, can hardly be corrected by the proposed method. In the future, advanced radiometric calibration of MLS data should be developed and applied prior to the road marking extraction.

### **5.3.2 Large-size High-pass Enhancement**

This thesis introduces a large-size high-pass filtering method to reduce the in-class variance and highlight the road markings from pavements successfully. However, this image-based filter cannot be implemented on the 3D point cloud directly. Due to the conceptual similarity between the pixel and the voxel, lots of sophisticated pixel-based algorithms can be applied in voxel-based point cloud processing. In the future, the large-size high-pass enhancement of markings could be realized by a suitable voxel-based algorithm.



## References

- Adams, R. and Bischof, L. (1994). Seeded region growing. *IEEE Transactions Pattern Analysis and Machine Intelligence*, vol. 16, pp.641–647.
- ASPRS Standards Committee. (2011). *ASPRS LIDAR Data Exchange Format Standard, Version 1.4*. Retrieved from [http://www.asprs.org/a/society/committees/standards/LAS\\_1\\_4\\_r13.pdf](http://www.asprs.org/a/society/committees/standards/LAS_1_4_r13.pdf)
- Barber, D., Mills, J., and Smith-Voysey, S. (2008). Geometric validation of a ground-based mobile laser scanning system. *ISPRS Journal of Photogrammetry and Remote Sensing*, vol. 63, pp.128-141.
- Borgefors, G. (1986). Distance transformations in digital images. *Computer Vision, Graphics, and Image Processing*, pp.344-371.
- Cabo, C., Ordoñez, C., García-Cortés, S. and Martínez, J. (2014). An algorithm for automatic detection of pole-like street furniture objects from Mobile Laser Scanner point clouds. *ISPRS Journal of Photogrammetry and Remote Sensing*, vol. 87, pp.47-56.
- Chen, X., Stroila, M. and Wang, R. (2009). Next generation map marking: geo-referenced ground-level LiDAR point clouds for automatic retro-reflective road feature extraction. *17th ACM SIGSPATIAL International Conference on Advances in Geographic Information System*, Seattle, WA, USA, 04-06 November , pp.4-6.
- Clode, S., Rottensteiner, F., Kootsookos, P. and Zelniker, E. (2007). Detection and vectorization of roads from LiDAR data. *Photogrammetric Engineering & Remote Sensing*, vol. 73, no. 5, pp.517-535.
- Dalal, N. and Triggs, B. (2005). Histograms of Oriented Gradients for Human Detection. In *IEEE Conference Computer Vision and Pattern Recognition*, Sean Diego, CA, USA, 20-25 June, vol. 1, pp.886–893.
- Danescu, R. and Nedeveschi, S. (2010). Detection and classification of painted road objects for intersection assistance applications. In *IEEE Conference on Intelligent Transportation System*, Funchal, Portugal, 19-22 September, pp.433-438.
- Florida Department of Transportation. (2008). *Terrestrial mobile LiDAR surveying & mapping guidelines*. Retrieved from Florida Department of Transportation website: [http://www.dot.state.fl.us/surveyingandmapping/documentsandpubs/20131007\\_tml\\_guidelines.pdf](http://www.dot.state.fl.us/surveyingandmapping/documentsandpubs/20131007_tml_guidelines.pdf)

- Foucher, P., Sebsadji, Y., Tarel, J., Charbonnier, P. and Nicolle, P. (2011). Detection and recognition of urban road markings using images. In *14th International IEEE Conference on Intelligent Transportation Systems (ITSC)*, Washington, DC, USA, 05-07 October, pp.1747-1752.
- Franke, U., Gavrilu, D., Gorzig, S., Lindner, F., Paetzold, F. and Wohler, C. (1998). Autonomous driving goes downtown. *IEEE Intelligent Systems and their Applications*, vol. 6, pp.40-48.
- Freeman, W.T. and Adelson, E.H. (1991). The design and use of steerable filters. *IEEE Transactions on Pattern Analysis and Machine Intelligence*, vol. 13, no. 9, pp.891 -906.
- Guan, H., Li, J., Yu, Y., Wang, C., Chapman, M. and Yang, B. (2014). Using mobile laser scanning data for automated extraction of road markings. *ISPRS Journal of Photogrammetry and Remote Sensing*, vol. 87, pp.93–107
- Guan, H., Li, J., Yu, Y., Ji, Z. and Wang, C. (2015). Using mobile LiDAR data for rapidly updating road markings. *IEEE Transactions Intelligent Transportation Systems*, vol. 16, no. 5, pp.2457-2466.
- Guizzo, E. (2011). How google's self-driving car works. Retrieved from IEEE Spectrum Online website: <http://www.123seminarsonly.com/Seminar-Reports/2015-03/190666282-Google-Car.docx>
- Hervieu, A. and Soheilian, B. (2013). Semi-automatic road/pavement modeling using mobile laser scanning. *ISPRS Annals*, vol. II-3/W3, pp.31-36
- Hervieu, A., Soheilian, B. and Brédif, M. (2015). Road marking extraction using a model&data-driven RJ-MCMC. *ISPRS Annals*, vol. 2, no. 3, pp.47.
- Innovative Software Engineering. (2015). *Google driverless car report*. Retrieved from <http://www.slideshare.net/ammudaddala15/googles-driverless-car-report>
- Jaakkola, A., Hyypää, J., Hyypää, H. and Kukko, A. (2008). Retrieval algorithms for road surface modelling using laser-based mobile mapping. *Sensors*, vol. 8, pp.5238-5249.
- Kaasalainen, S., Vain, A., Krooks, A. and Kukko, A. (2009). Topographic and Distance Effects in Laser Scanner Intensity Correction. In *ISPRS Laserscanning*, Paris, France, vol. 38, pp.219-223.
- Kaasalainen, S., Jaakkola, A., Kaasalainen, M., Krooks, A. and Kukko, A. (2011). Analysis of incidence angle and distance effects on terrestrial laser scanner intensity: search for correction methods. *Remote Sensing*, vol. 3, no. 10, pp.2207–2221.

- Kent, L. (2015). *Autonomous cars can only understand the real world through a map*. Retrieved from the official Here blog: <http://360.here.com/2015/04/16/autonomous-cars-can-understand-real-world-map/>
- Kheyrollahi, A. and Breckon, T. P. (2010). Automatic real-time road marking recognition using a feature approach. *Machine Vision and Applications*, vol. 23, no. 1, pp.123-133.
- Kukko, A., Karritine, H., Hyypä, J. and Chen, Y.(2012). Multiplatform mobile laser scanning: usability and performance. *Sensors*, vol. 12, pp.11712-11733.
- Kumar, P., McElhinney, C. P., Lewis, P. and McCarthy, T. (2014). Automated road markings extraction from mobile laser scanning data. *International Journal of Applied Earth Observation and Geoinformation*, vol. 32, pp.125-137.
- Li, W., Lu, G. and Wang, Y. (1997). Recognizing white line markings for vision-guided vehicle navigation by fuzzy reasoning. *Pattern Recognition Letters*, vol. 18, pp.771-780.
- Li, B., Li, Q., Shi, W. and Wu, F. (2004a). Feature extraction and modeling of urban building from vehicle-borne laser scanning data. In *ISPRS Archives*, Istanbul, Turkey, 12–23 July, pp.934-940.
- Li, Q., Zheng, N. and Cheng, H. (2004b). Springrobot: A prototype autonomous vehicle and its algorithms for lane detection. *IEEE Transactions Intelligent Transportation Systems*, vol. 5, no. 4, pp.300–308.
- Li, Y., He, K. and Jia, P. (2007). Road markers recognition based on shape information. *IEEE International Symposium on Intelligent Vehicles*, Istanbul, Turkey, 13-15 June 2007, pp.117-122.
- Litman, T. (2014). Autonomous Vehicle Implementation Predictions. *Victoria Transport Policy Institute*, 28
- Liu Z., Wang, J. and Liu, D. (2013). A new curb detection method for unmanned ground vehicles using 2d sequential laser data. *Sensors*, vol. 13, pp.1102-1120.
- Liu, Y., Wei, W., Wang, P. and Zalik, B. (2007). Compressed vertex chain codes. *Pattern Recognition*, vol. 40, no. 11, pp.2908-2913.
- Lemmens, M. (2011). Geo-information: Technology, Applications and the Environment. *Geotechnologies and the Environment Series*, Springer, vol. 5, pp.101-121.

- Manandhar, D. and Shibasaki, R. (2002). Auto-extraction of urban features from vehicle-borne laser data. *International Archives of Photogrammetry Remote Sensing and Spatial Information Sciences*, vol. 34, no. 4, pp.650-655.
- Mathibela, B., Newman, P. and Posner, I. (2015). Reading the Road: Road Marking Classification and Interpretation. *IEEE Transactions on Intelligent Transportation Systems*, vol. 16,no.4, pp. 2072-2081.
- McCall, J. C. and Trivedi, M. M. (2006). Video based lane estimation and tracking for driver assistance: Survey, system, and evaluation. *IEEE Transactions on Intelligent Transportation Systems*, vol. 7, no. 1, pp.20–37.
- McElhinney, C., Kumar, P., Cahalane, C. and McCarthy, T. (2010). Initial results from European road safety inspection (EuRSI) mobile mapping project. *International Archives of Photogrammetry, Remote Sensing and Spatial Information Sciences* vol. 38, part 5, pp.440-445.
- Ogund, J. O. (2015). *Precision Surveying: The Principles and Geomatics Practice*. John Wiley & Sons, pp.648.
- Olsen, M. J. (2013). *Guidelines for the Use of Mobile LiDAR in Transportation Applications*. Transportation Research Board.
- Otsu, N. (1979). A threshold selection method from gray-level histogram. *IEEE Transactions on Systems, Man, and Cybernetics*, vol. 9, no. 1, pp.62-66.
- People's Republic of China National Standards (2009). *Road traffic signs and markings part 3: road traffic markings*. Retrieved from <http://www.cdzj.gov.cn/images/dfbz/GFGGBZ05.pdf>
- Pu, S., Rutzinger, M., Vosselman, G. and Elberink, S. O. (2011). Recognizing basic structure from mobile laser scanning data for road inventory studies. *ISPRS Journal of Photogrammetry and Remote Sensing*, vol. 66, pp.s28-s39.
- Puente, I., González-Jorge, H., Martínez-Sánchez, J. and Arias, P (2013). Review of mobile mapping and surveying technologies. *Measurement*, vol. 47, pp.2127-2145.
- Rebut, J., Benschair, A. and Toulminet, G. (2004). Image segmentation and pattern recognition for road marking analysis. *IEEE International Symposium Industrial Electronics*, vol. 1, no. 4-7, pp.727-732.
- RIEGL. (2015). Compact Mobile Laser Scanning System, RIEGL VMX-450. Retrieved from: [http://www.riegl.com/uploads/tx\\_pxpriegl/downloads/DataSheet\\_VMX-450\\_2015-03-19.pdf](http://www.riegl.com/uploads/tx_pxpriegl/downloads/DataSheet_VMX-450_2015-03-19.pdf)

- Salakhutdinov, R. and Hinton, G. E. (2009). Deep Boltzmann machines. In *the 12th International Conference on Artificial Intelligence and Statistics (AISTATS'09)*, Clearwater Beach, Florida USA, 16-18 April, vol. 5, pp.448-455.
- Schwarz, K.P. and El-Sheimy, N. (2007). Digital mobile mapping systems - state-of-the-art and future trends. In: V. Tao and J. Li (eds.). *Advances in Mobile Mapping Technology*, Taylor & Francis, pp.3-18.
- Smadja, L., Ninot, J. and Gavrilovic, T. (2010). Road extraction and environment interpretation from LiDAR sensors. *ISPRS Archives*, vol. 38, pp.281-286.
- Sebsadji, Y., Tarel, J.P., Foucher, P. and Charbonnier, P. (2010). Robust road marking extraction in urban environments using stereo images. In *IEEE Intelligent Vehicle Symposium*, San Diego, USA, 21-24 June, pp.394-400.
- Sokolova, M., Japkowicz, N. and Szpakowicz, S. (2006). Beyond accuracy, F-score and ROC: a family of discriminant measures for performance evaluation. In *Advances in Artificial Intelligence*, Hobart, Australia, 04-08 December, vol. 4304, pp.1015-1021
- Talaya, J., Bosch, E., Alamús, R., Serra, A. and Baron, A. (2004). GEOVAN: The Mobile Mapping System from the ICC. In: V. Tao and J. Li (eds.). *Advances in Mobile Mapping Technology*, Taylor & Francis.
- Toth, C., Paska, E. and Brzezinska, D. (2008). Using road pavement markings as good control for LiDAR data. *ISPRS Archives*, vol. 37 (B1), pp.189-196.
- Tournaire, O., Pappadimitis, N. and Lafarge, F. (2007). Rectangular Road Marking Detection with Marked Point Processes. In *Photogrammetric Image Analysis Conference*, Munich, Germany, vol. 36, no. 3/W49A, pp.149-154.
- Vosselman, G. and Maas, H.-G. (2010). *Airborne and Terrestrial Laser Scanning*, Whittles Publishing: Caithness, UK.
- Vosselman, G. (2009). Advanced point cloud processing, *Photogrammetric Week'09*, Heidelberg, Germany, 7-11 September, pp.137-146.
- Vosselman, G., Gorte, B., Sithole, G. and Rabbani, T. (2004). Recognizing structure in laser scanner point clouds. *International Archives of Photogrammetry, Remote Sensing and Spatial Information Sciences*, vol. 36 (Part 8/W2), pp.33-38.
- Wang, N., Liu, W., Zhang, C., Yuan, H. and Liu, J. (2009). The detection and recognition of arrow markings recognition based on monocular vision, *Chinese Control and Decision Conference*, Guilin, China, 17-19 June, pp.4380-4386.

- Wagner, W., Ullrich, A., Ducic, V., Melzer, T. and Studnicka, N. (2006). Gaussian decomposition and calibration of a novel small-footprint full-waveform digitising airborne laser scanner. *ISPRS Journal of Photogrammetry and Remote Sensing*, vol. 60, pp.100-112.
- Whitwam, R. (2014). How Google's self-driving cars detect and avoid obstacles. Retrieved from <http://www.extremetech.com/extreme/189486-how-googles-self-driving-cars-detect-and-avoid-obstacles>
- Williams, K., Olsen, M. J., Roe, G. V. and Glennie, C. (2013). Synthesis of transportation applications of mobile LiDAR. *Remote Sensing*, vol. 5, no. 9, pp.4652-4692.
- Wu, S.T. and Márques, M.R.G. (2003). A non-self-intersection DouglasPeucker algorithm. In *XVI Brazilian Symposium on Computer Graphics and Image Processing*, Sao Carlos, Brazil, 12-15 October, pp.60-66
- Wu, T. and Ranganathan, A. (2012) A practical system for road marking detection and recognition. In *IEEE Intelligent Vehicles Symposium*, pp.25-30.
- Yang, B., Fang, L., Li, Q. and Li, J. (2012). Automated extraction of road markings from mobile LiDAR point clouds, *Photogrammetric Engineering & Remote Sensing*, vol. 78, no. 4, pp.331-338.
- Yang, B., Fang, L. and Li, J. (2013). Semi-automated extraction and delineation of 3D roads of street scene from mobile laser scanning point clouds. *ISPRS Journal of Photogrammetry and Remote Sensing*, vol. 79, pp.80-93.
- Yang, M., Kpalma, K. and Ronsin, J. (2008). A survey of shape feature extraction techniques. In: *Yin, P.Y. (ed.) Pattern Recognition*, IN-TECH, pp.43-90.
- Yu, Y., Li, J., Guan, H., Jia, F. and Wang, C. (2015). Learning hierarchical features for automated extraction of road markings from 3-D mobile LiDAR point clouds. *IEEE Journal Selected Topics in Applied Earth Observations and Remote Sensing*, vol. 8, no. 2, pp.709-726.
- Zhao, H. and Shibasaki, R. (2002). Surface modelling of urban 3D objects from vehicle-borne laser range data. *ISPRS Archives*, vol. 34 (Part 3/WG III/7).
- Zhang, D. and Lu, G. (2004). Review of shape representation and description techniques. *Pattern Recognition*, vol. 37, pp.1-19.
- Zhou, Y., Yu, Y., Lu, G. and Du, S. (2012). Super-segments based classification of 3-D urban street scenes. *International Journal of Advanced Robotic Systems*, vol. 9, no. 248, pp. 1-8.